Quality Assessment of VTEC Products Derived from Observations with the Next-Generation VLBI System

Master Thesis

Author(s):
Awadaljeed, Mudathir

Publication date:
2021-07-12

Permanent link:
https://doi.org/10.3929/ethz-b-000573149

ETH zürich

IGP
Institut für Geodäsie und Photogrammetrie

Master's Thesis

Quality Assessment of VTEC Products Derived from Observations with the Next-Generation VLBI System

Mudathir Awadaljeed

July 12, 2021

Institute of Geodesy and Photogrammetry
Space Geodesy
ETH Zurich

Supervisors

Prof. Dr. Benedikt Soja
Dr. Grzegorz Kłopotek

Acknowledgment

While writing this master's thesis, I have received a great deal of support and assistance. I would like to thank Prof. Benedikt Soja for offering me the opportunity to work on the topic forming the basis of this master's thesis. I found his guidance and feedback helpful. I would like also to thank Dr. Grzegorz Kłopotek for supervising this master's thesis and making his expertise available to me. His insightful feedback helped me to sharpen my problem-solving skills and bring my thesis to a higher level. Furthermore, I am grateful to Prof. Andreas Wieser for contributing to my ETH Zurich Master Scholarship Award (MSP) during my first semesters and supporting me with guidance and valuable input in the past. In addition, it is a pleasure to thank Prof. Sarah Springman and Dr. Barbara E. Hellermann for further supporting me with a scholarship from Winiker-Foundation during this master's thesis.

I would like to thank the people and organizations behind the International VLBI Service for Geodesy and Astronomy (IVS) and International GNSS service (IGS) for making the geodetic datasets and products publicly available as well as scientists and organizations contributing to the establishment and maintenance of the Madrigal dataset.

Abstract

The ionosphere hosts all charged particles in the Earth's atmosphere. It is a dispersive medium for radio signals allowing to investigate the variability and changes of this medium with the use of ground-based geodetic instruments operating in the microwave regime. One of the parameters of interest in connection to ionosphere is the vertical total electron content (VTEC) that can be derived from multi-frequency measurements carried out with space-geodetic techniques such as global satellite navigation system (GNSS) and geodetic very long baseline interferometry (VLBI). The latter technique relies on measurements of the time difference in the arrival of microwave signals from natural and very distant radio sources (quasars) at two or more radio telescopes located on the Earth surface. The focus of this thesis are the VTEC products derived from the next-generation VLBI system, known as the VLBI global observing system (VGOS). The latter has already reached an operationally stable international network. However, VGOS continuously evolves into a truly global infrastructure. Since late 2017, VGOS observations, organized as 24-hour sessions, were already carried out. Currently, there are over forty sessions that are available. In this master's thesis, a Python code was developed to process these sessions and derive VTEC time series above VGOS stations. In modelling the ionosphere with VGOS, piece-wise linear (PWL) function with a temporal resolution of one hour is used to consider the time variability of the ionosphere above VGOS sites. The modified dip (modip) latitude is used to consider the influence of the Earth's magnetic field on the ionosphere, and Sun-fixed coordinate system is used to account for the strong correlation between the ionosphere and the position of the Sun. In addition, latitudinal ionospheric gradients and VGOS instrumental offsets are considered in the adjustment process and assumed to remain constant during the 24-hour session.

The results show that VTEC time series from VGOS observations show similar temporal behavior of ionosphere when compared with VTEC time series from global ionosphere maps (GIMs) and Madrigal total electron content maps (MTMs). This is also the case when VTEC time series from VGOS observations are compared with VTEC time series from observations carried out with both geodetic VLBI and GNSS stations that are co-located with VGOS telescopes. Furthermore, a bias between VGOS-derived VTEC time series and the remaining VTEC time series from GIMs, MTMs and GNSS observations was identified. This bias, which often has a positive sign, varies in size across the investigated sessions, reaching few TEC unit (TECU). The smallest and largest RMS differences w.r.t. GIMs-based VTEC time series occur at Onsala Space Observatory (ONSA13NE and ONSA13SW) and at Kokee Park Geophysical Observatory (KOKEE12M), reaching 2.6 ± 0.5 and 5.4 ± 1.1 TECU, respectively. The smallest and largest RMS differences w.r.t. MTMs-based VTEC time series are noticed for ISHIOKA and GGAO12M, reaching 1.6 ± 0.2 and 3.3 ± 1.0 TECU, respectively. Based on the investi-

gated VGOS sessions, the uncertainty of VGOS-derived VTEC time series is on the order of 0.12 ± 0.03 TECU for all VGOS station except KOKEE12M, where the uncertainty is on the order of 0.22 ± 0.05. In addition, the results indicate that the uncertainty of the north ionospheric gradient is often better resolved than the uncertainty of the south gradient due to the current geometric configuration of the operational VGOS network. In general, VGOS-derived VTEC has the potential to complement local and global ionospheric maps in the vicinity of VGOS stations.

Contents

List of Abbreviations

- CDDIS Crustal Dynamics Data Information System
- DCBs Differential Code Biases
- dTEC differential TEC
- EDW Elevation Dependent Weighting
- EFRF Earth-FixedReference Frame
- EPBs Equatorial Plasma Bubbles
- EOP Earth Orientation Parameters
- GIMs Global Ionosphere Maps
- GNSS Global Navigation Satellite System
- GGOS Global Geodetic Observing System
- IPP Ionospheric Pierce Point
- IGRF International Geomagnetic Reference Field
- ITRF International Terrestrial Reference Frame
- ICRF International Celestial Reference Frame
- IGS International GNSS Service
- IVS International VLBI Service for Geodesy & Astronomy
- IAACs IGS Ionosphere Associate Analysis Centres
- LSQ Least SQuares
- Modip Modified dip
- MTMs Madrigal TEC Maps
- PWL Piece Wise Linear
- RFI Radio Frequency Interference
- SMTMs Smoothed Madrigal TEC Maps

- STEC Slant Total Electron Content
- TEC Total Electron Content
- TECU Total Electron Content Unit
- VLBI Very Long Baseline interferometry
- VGOS VLBI Global Observing System
- VCE Variance Component Estimation
- VTEC Vertical Total Electron Content
- WGS84 World Geodetic System 1984

1 Introduction

Space geodesy is a scientific discipline providing key geophysical measurements of Earth's layers and atmosphere (Abdalati et al., 2018; Davis et al., 2016; Mathews et al., 2002). It utilizes observation techniques such as the global navigation satellite system (GNSS), Doppler orbitography and radio-positioning integrated by satellite (DORIS), satellite laser ranging (SLR), and geodetic very long baseline interferometry (VLBI) (Niell et al., 2018). The latter technique measures the difference in the arrival times of a radio signal emitted from a radio source, so-called quasar, at two antennas fixed to the Earth surface, see Fig. 1.1. The next generation of of the VLBI system, known as the VLBI global observing system (VGOS), currently at the initial phase, has been designed in order to meet ambitious goals of the Global Geodetic Observing System (Plag and Pearlman, 2009), aiming toward an accuracy of 1 mm in station position and 0.1 mm/year in station velocity on a global scale (Niell et al., 2006; Petrachenko et al., 2009). The current delay uncertainty of the new VLBI system, i.e., 8 *ps*, is approximately 75% better than that for the legacy VBLI system, i.e., 31 *ps* (Niell et al., 2018)

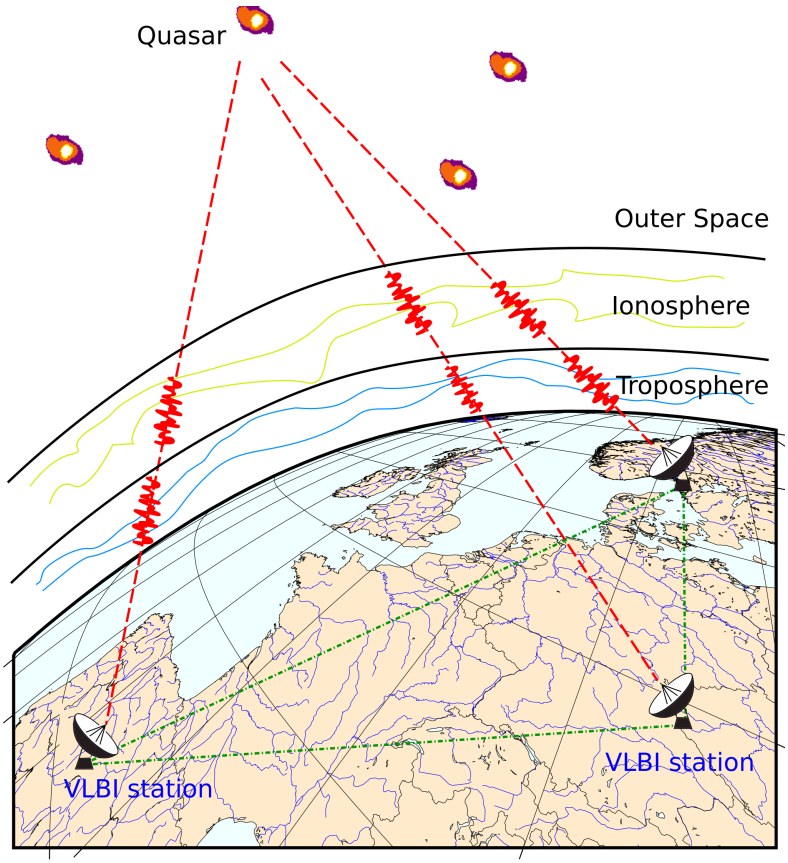

Figure 1.1: The concept of geodetic VLBI

As the electromagnetic signal propagates through the Earth's ionosphere, which is a dispersive medium, it is subjected to advances and delays that are proportional to its frequency and the slant total electron content (STEC) along its path. STEC can be projected into the vertical direction to obtain the vertical total electron content (VTEC) above the geodetic stations (Schaer et al., 1998). Since VGOS stations are equipped with the broadband signal chain system, the broadband delay can be obtained, and the VTEC parameters can also be derived (Niell et al., 2018). The parameters relating to TEC are of importance in various fields such as space weather and climate analysis (Jin et al., 2017).

The ionospheric delays in single-frequency GNSS observations could cause a ranging error of up to (300 ns) 100 m (Johnston et al., 2017). Therefore, in the case of single-frequency GNSS observations, it is important for correcting these delays using regional or global ionospheric models such as global ionospheric maps (Cai et al., 2017). In general, multi-frequency space-geodetic techniques, such as GNSS and VLBI, offer the possibility of deriving ionospheric parameters based on the performed observations, but with varying spatio-temporal resolution and latency. These ionospheric parameters help us also to learn more about the dynamics of the ionospheric processes, for instance, the origin and propagation of ionospheric storms (Johnston et al., 2017).

Similar to the geodetic VLBI, hereafter referred to as the legacy VLBI system, VGOS has the potential to contribute to the knowledge on the ionosphere state in the vicinity of VGOS stations. This new system has already carried out many observations, organized as 24-hour sessions, forty four of which have been made publicly available until present, (Noll, 2010). This allows to utilize the available VGOS sessions to assess the quality of the ionospheric products, such as VTECs, derived from observations made with this new system. The VGOS network is is still expanding. Currently, it has nine operational stations, and, by the end of this decade, the number of stations coming into service is expected to grow significantly (Abdalati et al., 2018). VGOS system is designed to operate continuously, implying collection of huge amounts of data. This might raise also a need for automating its data processing and analysis in order to generate ionospheric products within 24 hour after data acquisition.

Based on the aforementioned needs, the main goals of this master's thesis are threefold. The first goal is to derive VTEC time series at VGOS sites based on all available 24-hour VGOS sessions. The second goal is to perform a comprehensive quality analysis of these estimates in relation to internal and external ionospheric products, such as global ionosphere maps and GNSS-derived VTEC time series at co-location sites with VGOS antennae, respectively. The third goal is to develop an automatic processing pipeline for obtaining and deriving VTEC time series from VGOS observations.

1.1 Thesis Structure

The structure of this thesis is organized as follows. First, background information about the ionosphere, VLBI and VGOS are introduced in Chapter 2. Second, the data and the pre-processing stages are described in Chapter 3. Third, the methodology followed in this research is outlined in Chapter 4. Fourth, the results are presented in Chapter 5, and they are discussed and analysed in Chapter 6. Finally, the main findings of this master's thesis are summarized as well as key insights and possible avenues for future research related to the topic investigated in this thesis are highlighted in Chapter 7.

2 Theoretical Foundations

2.1 Ionosphere

Ionosphere is an upper layer hosting charged particles and covering areas from approximately 50 to 1000 km above the mean sea level. This however varies and depends primarily on the solar radiation. When the day comes, the Sun heats the particles up. They get excited and release electrons, making them ionized. When the night falls, they relax and combine with the ions to form neutral particles. Other solar phenomena, for example, flares, solar wind, and geomagnetic storms also affect the ionosphere. Furthermore, extreme weather events on Earth, such as hurricanes, create pressure waves, which also disturb the ionosphere. The ionosphere also depends on the Earth's magnetic field, and this is evident at low latitudes in the form of the so-called equatorial plasma bubbles (EPBs), which have very low electron density during the night. Thus, changes in the magnetic field caused by, for example, solar winds can disturb the ionosphere state (Johnston et al., 2017; Schaer, 1999).

The ionosphere is an important factor in satellite communication and navigation. Since ionospheric disturbances affect such domains, there is a pressing need for reliable ionospheric products to correct for ionospheric delays in single-frequency GNSS observations, which can introduce a ranging error of up to 100 m (300 ns), and also to learn more about the dynamics of the ionospheric processes such as the origin and propagation of ionospheric storms (Johnston et al., 2017).

Ionosphere is a dispersive medium for radio waves, where its refractive index is primarily a function of its electron density and the signal frequency f (Sekido et al., 2003). Thus, the radio signals used in space-geodesy techniques, such as geodetic VLBI, VGOS, and GNSS, experience ionospheric delays that vary in magnitude. The ionosphere delay (τ_{ion}) expressed in meters can be approximated to a first order by

$$\tau_{\mathbf{ion}} = \pm \frac{40.3}{f^2} TEC, \tag{2.1}$$

where TEC stands for total electron content, i.e., the total number of electrons in a columnar cylinder of square meter along the signal path, and it is expressed in TECU, i.e. 10^{16} $electrons/m^2$. The frequency is given in Hz.

For single-frequency observations, such as those collected by single-frequency GNSS receivers, correction of ionospheric effects should be applied using an ionospheric model such as Klobuchar (Klobuchar, 1987) or NeQuick (Di Giovanni and Radicella, 1990). For multi-frequency observations, these effects can be reduced to a large extent by using ionospheric-free linear combination

of simultaneous measurements made at different frequency bands. In general, space-geodesy techniques with multi-frequency measurements can provide us with not only corrections for the ionosphere effects but also valuable information about the ionosphere and its behaviour (Johnston et al., 2017).

2.2 Geodetic Very Long Baseline Interferometry

Geodetic very long baseline interferometry (VLBI) is an important space-geodetic technique (Bachmann et al., 2016; Nothnagel et al., 2017), contributing to the establishment of the international terrestrial reference frame (ITRF) (Altamimi et al., 2016), and the international celestial reference frame (ICRF) (Charlot et al., 2020), since 1970s. In addition, geodetic VLBI uniquely provides Earth orientation parameters (EOP), which link ITRF and ICRF (Niell et al., 2018). While ICRF finds applications, for instance, in spacecraft navigation (quasar-spacecraft differential VLBI), EOP are also necessary for accurate satellite orbit determination (Niell et al., 2006), and help in understanding the properties of the Earth's mantle and core (Mathews et al., 2002).

Geodetic VLBI measures the time difference between the arrivals of microwave signals from extragalactic radio sources at two or more antennae, which are tied to the Earth's surface. These radio sources, commonly referred to as quasars, are billions of light years away, and they form the aforementioned ICRF, with the latest release known as ICRF3 (Charlot et al., 2020). In the legacy system, the measurements are carried out in the S/X bands at approx. 2 and 8 GHz, respectively (Sekido et al., 2003). A baseline consists of a pair of telescopes simultaneously observing the same radio source while a network is formed by all the participating stations in the session. A source scan consists of simultaneous observations made by a group of telescopes to the same radio source, see Fig. 1.1.

Although geodetic VLBI has contributed significantly to geodesy over decades and the precision of measurements it provides has improved significantly, its network already reached its performance limits (Niell et al., 2006). First, the telescopes are aging, costly to maintain and slow to move, making it difficult to meet today's geodetic requirements for high accuracy, for example, see Fig. 2.1. Secondly, there is a dramatic increase in the radio interference, particularly in the S-band, reducing the sensitivity of the system and making it prone to more errors. Thirdly, for some stations, the data are still recorded on disks and physically shipped to the correlators, resulting in delays for final products. Finally, the distribution of the telescopes world-wide is not ideal, limiting the sensitivity of the system to EOP. These problems and the need for a significant leap in the performance of geodetic VLBI motivated the International VLBI Service for geodesy and astronomy (IVS) to review its geodetic VLBI system from antenna structure, through correlation, to analysis approaches and developed the next-generation VLBI system

(Niell et al., 2006).

Figure 2.1: The 26-m radio telescope located at Hartebeesthoek Radio Astronomy Observatory (HartRAO), South Africa

2.3 VLBI Global Observing System

The decision upon the geodetic VLBI system resulted in the design of the broadband equipment forming the basis of the next-generation VLBI system, hereafter referred to as VLBI Global Observing System (VGOS). With the dawn of the new system, one tries to meet two main goals. The first goal is related to performance, i.e. an accuracy of 1 mm in position and 0.1 mm/s in station velocity per year on a global scale. The second goal is operational, i.e. continuously providing station positions and EOP while making the products available within 24 hour after data collection (Niell et al., 2006). Unlike the legacy VLBI system, this system is based on a broadband technology, which use four carefully-chosen frequency bands between approx. 2GHz and 14GHz to increase its sensitivity and the precision of its derived group delays, and to reduce radio frequency interference (RFI). Compared to S/X, broadband observations allow to increase precision of group delays hereafter referred to as broadband delays. Further, VGOS makes use of small, fast-slewing antennas, i.e. approx. 13 m in diameter and at least

360° per minute in terms of slew speed. An example of the VGOS-compliant telescope is shown in Fig. 2.2. This is to allow for short source-switching intervals and to provide more angularly well-distributed observations, i.e. an observation every 30 seconds or less, by decreasing the source scans to 30 seconds or less. This produces high temporal and spatial resolutions, and eventually significantly decreases the effect of the troposphere delay, which is one of the largest source of random errors in VGOS observations besides the radio source structure effects. Furthermore, this next-generation VLBI system uses high recording bandwidths, i.e. at least 8 Gps, and digital signal processing to increase VGOS observation sensitivity and to have more stable instrumentation. In addition, the VGOS concept is also driven by the idea of operating continuously and autonomously. As the VGOS network is rapidly growing, it shall gradually replace the legacy VLBI system (Niell et al., 2018). The distribution of VGOS stations that are currently operational and considered in this thesis is shown on Fig. 2.3.

Figure 2.2: WETTZ13S VGOS Antenna in Germany

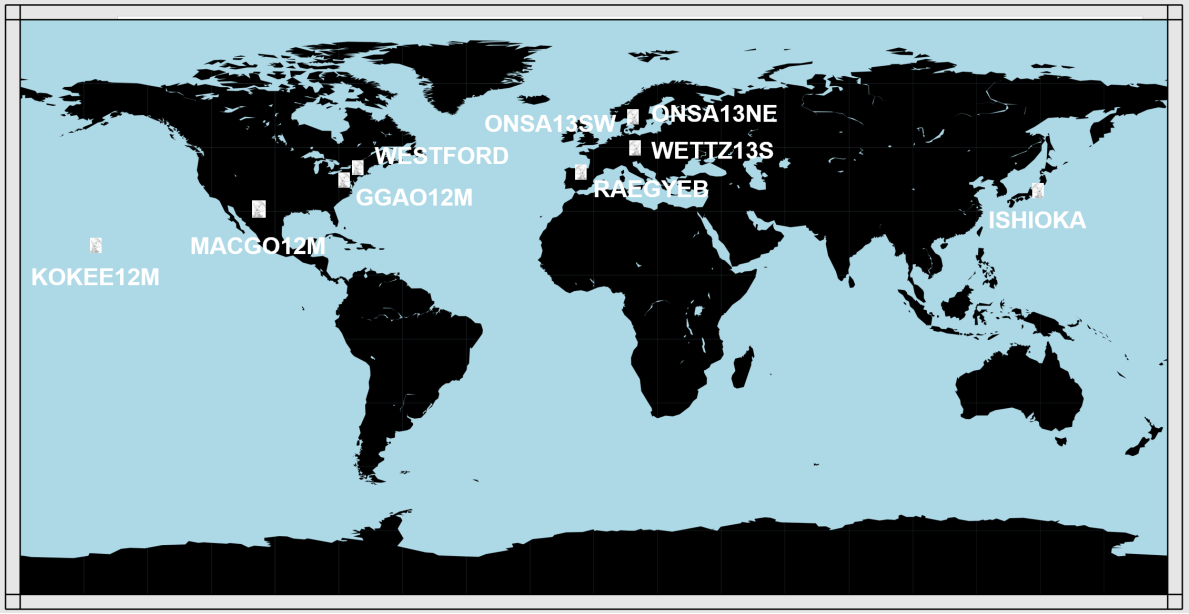

Figure 2.3: Current Operational VGOS Stations

2.4 Ionospheric Delays from Geodetic VLBI and VGOS

The processing pipeline for obtaining ionospheric delays from the observations of the legacy VLBI system differs in many aspects from that for VGOS. One of main reason for this difference is that VGOS uses a four-band, dual-linear-polarization signal chain instead of S/X bands as in the case of the legacy system (Barrett et al., 2019). For VLBI, the processing pipeline consists of three main stages. The first stage is the correlation, in which the recorded station-based signals of each baseline are correlated to average out the receiver noise and find the coherence signal of the radio sourc. The second stage is the post-correlation analysis stage, also known as the fringe-fitting stage, in which the group delays for the S/X bands are obtained separately. The third stage is the analysis, in which parameters such as coordinates of VLBI telescopes, EOP and radio source positions are estimated. The group delays in this case are reduced by the ionospheric contribution deduced from the combination of X-band and S-band delays (Niell et al., 2018).

For VGOS, the processing pipeline consists also of three main stages, i.e., correlation, post-correlation analysis, and data analysis. In the second stage, broadband delays and ionospheric delays, the latter is hereafter referred to as dTEC, are estimated simultaneously. The uncertainty of undispersed broadband group delays from VGOS obervations is approximately 50 times smaller than the uncertainty of the S-band group delays from the observations of the legacy VLBI system, thanks to the broadband signal chain, which improves the delay precision and sensitivity significantly (Niell et al., 2018).

3 Input Data and Processing Steps

The input data utilized for the purposes of this thesis can be divided into three groups. The first group consists of VGOS observations present in VGOS databases, from which VTEC time series at VGOS stations are derived. These VTEC time series are the main subject of this master's thesis. The second group consists of VLBI and GNSS observations made with the legacy VLBI system and GNSS receivers, respectively. From this group, VTEC time series are also derived to serve as an internal reference in relation to the VGOS-derived VTEC time series. The third group is composed of global ionosphere maps (GIMs) and Madrigal TEC maps (MTMs). From these maps, VTEC time series are extracted to serve as an external reference concerning the VGOS-derived VTEC time series.

For the purpose of this thesis, the Python code has been developed allowing to automatically obtain, process, and analyse the input data, see Appendix A. The code will be made available as an open-source python library to be further extended for other space geodetic techniques. The resulting processing pipeline is introduced in more detail in Sec. 4.2.

This chapter is organized as follows. First, VLBI and VGOS databases as well as the necessary processing steps to acquire the VTEC time series are presented in Sec. 3.1. Then, GNSS observations from GNSS stations that are co-located with VGOS antennas are introduced in Sec. 3.2. Next, GIMs and MTMs as well as the necessary steps to extract the VTEC time series from both of these products are described in Sec. 3.3 and Sec. 3.4.

3.1 Geodetic VLBI and VGOS

Both VLBI and VGOS stations participate in 1-hour intensive sessions and 24-hour sessions. The recorded, station-based raw data are then electronically transferred or physically shipped to the correlators in order to correlate these observations and create geodetic databases containing group delays and auxiliary information related to the correlation stage. Next, the created databases are analysed by the analysis centres. The further-processed databases and the generated products such as EOP and station positions are then stored in IVS repositories and made available to the users by the data centres (Nothnagel et al., 2017).

IVS consists of three primary data centres, i.e., CDDIS (USA), BKG (Germany), and OPAR (France), archiving and disseminating its data and products. CDDIS uses an HTTP server while BKG and OPAR make use of an FTP server. There are two categories of data. The first is the primary data such as databases and NGS card files, while the second is the auxiliary data such as schedule and log files. The databases are of importance to us, and those used for this thesis are stored in the vgosDB format, which has netCDF binary files and ASCII files (Gipson, 2014). The VGOS sessions are organized by year and then by session. Each vgosDB

contains sub-directories for station/scan-dependent, scan-dependent, session-dependent, and observation-dependent data. The different data files are pointed out to in the wrapper, which is a simple, human-readable ASCII file present in the session directory.

3.1.1 VGOS Observations and Pre-processing Steps

One can download 24-hour VGOS sessions, whose files end with VG.tgz, from CDDIS's server using the module described in section 4.2.3. Then, one can extract the different types of data such as the coordinates of VGOS stations, the azimuth and elevation angles, and the ionospheric delays. Next, one can filter out the data, and this stage consists of many steps, which are described in the subsequent paragraphs.

First, one excludes all observations with formal errors equal to zero due to their unrealistic uncertainty. For the legacy VLBI system, some observations have zero frequencies in the S/X bands, and these observations are to be excluded as well. Second, one removes all observations with an elevation angle below a predefined cut off angle because it is difficult to model the ionospheric effects at low elevation angle. In general, no observations are made to radio sources below 5°. Third, one eliminates all observations with a signal-to-noise ratio below 15 since the corresponding group delay are considered as non-detections or of poor quality. This threshold was actually set in the scheduling stage for the session, but there are observations with a signal-to-noise ratio below this threshold due to the lack of perfect knowledge about the received signal strength (on the VGOS bands) of radio sources during the scheduling stage. Fourth, one leaves out all observation groups corresponding to radio sources that were observed less than five times since the variance components of these groups fluctuate largely when refining the stochastic model of the observations with variance component estimation (VCE), see section 4.1.1. Fifth, one can exclude all observations related to stations that experienced technical problems during the data acquisition. In this case, one needs however to consult the history files of the session and input the names of these stations before running the processing pipeline, see section 4.2.2.

Once the data is properly screened, one can proceed with the pre-processing stage, which consists of four main steps. The first step is converting the coordinates of VGOS stations from Cartesian coordinates to geographic coordinates, i.e., longitude, latitude, and altitude. This can be done using a suitable Python library such as pyproj (Whitaker, 2021). The second step concerns calculating the geographic latitude and longitude of the ionospheric pierce point (IPP), which is the intersection between the thin shell approximation of the ionosphere and the signal path from the radio source to the VGOS antenna, (Schaer et al., 1998; Hobiger et al., 2006; Dettmering et al., 2011b). For each VLBI/VGOS observation, this can be done using the following equations, which are provided by Klobuchar (1987):

$$\psi = \frac{\pi}{2} - \varepsilon - \sin^{-1}\left(\frac{R}{R+h}\cos\varepsilon\right), \tag{3.1}$$

$$\phi^{'} = \sin^{-1}\left(\sin\phi\cos\psi + \cos\phi\sin\psi\cos Az\right), \tag{3.2}$$

$$\lambda^{'} = \lambda + \frac{\psi \sin Az}{\cos\phi^{'}}, \tag{3.3}$$

where Az is the azimuth of the radio source in radian, and ε is the elevation angle in radian. The parameters described as ϕ and λ are the geographic latitude and longitude of VGOS station in radian while the parameters described as $\phi^{'}$ and $\lambda^{'}$ are the geographic latitude and longitude of IPP in radian. R and h are the mean radius of the Earth and the height of the ionospheric thin shell.

The third steps is to convert the latitudes of IPP and VGOS sites from geographic to either geomagnetic or modified dip latitudes in order to account for the dependency of the ionosphere on the Earth's magnetic field (Azpilicueta et al., 2006; Hobiger, 2006; Fu et al., 2021; Johnston et al., 2017). The geomagnetic reference system is defined as follows: its z-axis is parallel to the magnetic dipole, its y-axis is perpendicular both the Earth's rotation axis and the geomagnetic dipole, and its x-axis completes a right-handed system. The conversion to geomagnetic latitude can be performed using the following equation (Hobiger, 2006)

$$\sin\phi_m = \left(\sin\phi\sin\phi_0 + \cos\phi\cos\phi_0\cos\left(\lambda - \lambda_0\right)\right) \tag{3.4}$$

where ϕ_0 and λ_0 are the geographic latitude and longitude of the geomagnetic north pole. The pole is slowly changing its position due to the change in the geomagnetic field, i.e., the so-called geomagnetic secular variation. The coordinates of the pole can be acquired from the latest release of the international geomagnetic reference field (IGRF) 13^{th} generation (Alken et al., 2021).

At the magnetic equator, which is commonly referred to as the modip equator, the magnetic inclination or dip, which is the angle between the horizontal plane and the lines of the magnetic field, is zero. The location of the magnetic equator is slowly changing. The modified dip (modip) latitude μ can be calculated using

$$\tan(\mu) = \frac{I}{\sqrt{\cos\phi}}, \tag{3.5}$$

where I is the true magnetic inclination, which can be obtained using a Python library such as magnetic-field-calculator (Filip, 2021).
Since in VGOS the post-corellation analysis stage results in dTEC values expressed in TECU, the fourth step applies only to the legacy VLBI system, and it is related to the conversion of the VLBI ionospheric delays and their formal errors from seconds to TECU using the following equation (Sekido et al., 2003).

$$\tau_{\mathbf{ion}} = 40.3\frac{f_x^2 - f_s^2}{c f_x^2 f_s^2}\tau, \tag{3.6}$$

where τ is the VLBI ionospheric delays in seconds, c is the speed of light in m/s, and $f_{s/x}$ is the reference frequencies of the S/X bands as present in the EffFreq_bX.nc file of the vgosDb.

3.2 GNSS Observations

The International GNSS Services (IGS) makes available GNSS observations from a global network of ground tracking stations on a daily-basis. These observations are sampled every 30 sec and present in the RINEX format (Noll, 2010). IGS also provides the differential code biases (DCBs) for all active GNSS satellites and IGS receivers. The DCBs, which are provided along with GIMs, are used to correct the GNSS code observations and to generate the ionospheric dispersive delay, i.e., the so-called slant total electron content (STEC) (Schaer et al., 1998). One can derive VTCEs from GNSS observations collected by IGS receivers at sites co-located with VLBI/VGOS stations. The implemented module for deriving the VTECs from these GNSS observations is described in 4.2.7 and visualised in 4.7.

3.3 Global Ionosphere Maps

The IGS ionosphere associate analysis centres (IAACs), such as CODE in Switzerland, JPL in U.S.A, and CAS in China, derives independently global ionosphere maps (GIMs) from the IGS network data using different methods, such as tomographic methods with splines and spherical harmonics plus generalized trigonometric series (Hernández-Pajares et al., 2009; Wielgosz et al., 2021). Some centres provide rapid and final maps that are available in less than 24 hours and approximately 11 days later, respectively. These centers also generate predictions that cover the upcoming 1 - 2 days. The IGS later combines their solutions and provides predicted, rapid,

and final GIMs on a regular basis [1].
GIMs are organized by year and then by day of year. These products are provided in the IONEX format, and they are expressed on a 2.5°-by-5° grid in latitude and longitude in an Earth-Fixed Reference Frame (EFRF). These maps can be considered as snapshots of ionosphere at certain epochs expressed in UTC (Schaer et al., 1998). The maps from the different centres have a temporal resolution between 15 and 120 minutes. The final combined IGS GIMs have however a temporal resolution of 2 hours. The accuracy of the final map is within 3 TECU, depending on the solar activity (Wielgosz et al., 2021). For further information, see Rovira-Garcia et al. (2016, 2020); Chen et al. (2020).

3.3.1 Extracting VTECs from GIMs

In order to extract VTECs from GIMs at VLBI/VGOS sites, one needs to interpolate between those maps as a function of geographic location and time (Schaer et al., 1998). The first step is to locate the four grid points surrounding the VLBI/VGOS site. The second step is to calculate the weight for each grid point as a unitary distance from VLBI/VGOS site in East-West direction and North-South direction. The third step is to find the two consecutive maps before and after the epoch of the VLBI/VGOS observation. The fourth step is to compute VTEC at the VLBI/VGOS site as a weighted average of VTECs of those points from each map. The fifth step is to linearly interpolate VTECs at VLBI/VGOS site as a function of time. This procedure is summarized in the equations below

$$\begin{aligned} W_{ll} &= (1-p)(1-q), \\ W_{ul} &= (1-p)q, \\ W_{ur} &= pq, \\ W_{lr} &= p(1-q), \end{aligned} \tag{3.7}$$

with

$$\begin{aligned} p &= (\lambda - \lambda_l)/5, \\ q &= (\phi - \phi_l)/2.5, \end{aligned} \tag{3.8}$$

$$E_i(\phi, \lambda) = W_{ll}E_i(\phi_l, \lambda_l) + W_{ul}E_i(\phi_u, \lambda_l) + W_{ur}E_i(\phi_u, \lambda_r) + W_{lr}E_i(\phi_l, \lambda_r), \tag{3.9}$$

[1] IGS (2021) Ionosphere working group. https://www.igs.org/wg/ionosphere/

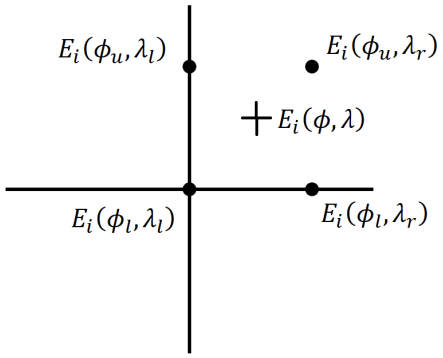

Figure 3.1: The four grid points surrounding the VLBI/VGOS site of interest

$$E(\phi, \lambda, t) = \frac{t_{i+1} - t}{t_{i+1} - t_i} E_i(\phi, \lambda) + \frac{t - t_i}{t_{i+1} - t_i} E_{i+1}(\phi, \lambda), \tag{3.10}$$

where λ and ϕ represents to the longitude and latitude of the VLBI/VGOS site of interest, respectively. The parameters described as λ_l and ϕ_l are the longitude and latitude of the lower-left grid point, respectively. W_{ul} and W_{lr} are the unity weight of the upper-left and lower-right grid points, respectively. E_i and E_{i+1} are GIMs-based VTECs at VLBI/VGOS site from the first and second consecutive maps, respectively. The parameters described as t_i and t_{i+1} are the epochs of the two consecutive maps, and t is the epoch of the VLBI or VGOS observation.

3.4 Madrigal TEC Maps

MIT Haystack Observatory developed an open source, web-based, distributed database system, which is known as Madrigal (Coster A, MIT/Haystack Observatory, 2021). Madrigal contains a wide variety of data, models, and products, such as incoherent scatter radar data and madrigal TEC maps (MTMs). The latter is of importance in the context of this thesis since it is strictly data-driven (Rideout and Coster, 2006), and can serve as a proper reference concerning VGOS-derived VTECs, see Sec. 5. The data is collected using a few thousands of globally distributed dual-frequency (L1/L2) GNSS receivers, many of which are not considered in the IGS network. Therefore, there is a need for estimating DCBs for the stations outside the IGS network, and this is performed in accordance to the dedicated method presented in Vierinen et al. (2016) and implemented in the MIT Automated Processing of GPS (MAPGPS) software suite, see Rideout and Coster (2006). As for the satellite biases, they use NASA Jet Propulsion Laboratory (JPL) estimates, which are available through CDDIS (Noll, 2010). The single TEC map is expressed on a 1°-by-1° grid in latitude and longitude with 5 min temporal resolution and only in the

vicinity of the receivers utilized to produce MTMs. When generating MTMs, the height of the ionospheric thin layer was set to 350 km. The uncertainties of the receiver biases and MTMs are not yet publically available (Rideout and Coster, 2006). For comparison with VLBI/VGOS-derived VTECs, one can simply take the nearest TEC bin to the VLBI/VGOS site of interest. Since the VTEC estimates, as present in MTMs, are often noisy, they can be smoothed using, for example, the Savitzky–Golay filter.

4 Methodology

4.1 Least Squares Adjustment

The method of least squares (LSQ) is widely used to estimate the most probable values of the unknowns from a group of observations, detect outliers in the observations and provides indicators of precision and accuracy for the observations and the adjusted parameters. In LSQ, one minimizes the weighted sum of squared residuals based on the assumptions made concerning two parts, i.e., the functional model and stochastic model. The former defines the mathematical relationship between the observations, hereafter referred to as n, and the unknowns, hereafter referred to as m, using a set of equations. The latter introduces the probabilistic behavior of the observations as weights into the adjustment. In this thesis, Gauss-Markov model, i.e., parametric model, is used, where individual observations are a function of the parameters (Teke et al., 2009; Guillaume, 2017; Ghilani, 2017). The mathematical model can be written in a general matrix form as follows

$$l + \hat{v} = A \cdot \hat{x} \tag{4.1}$$

where $\hat{v} \sim N(0, \sigma^2 W^{-1})$ is the vector of observation residuals (n $\times$ 1), W is the weight matrix (n $\times$ n) of the observations, A is the design matrix (n $\times$ m) containing the coefficients of the parameters, $\hat{x}$ is the vector of parameters (m $\times$ 1), and l is the vector of observations (n $\times$ 1). Assuming that the system is over-determined, i.e., the number of observations is higher than the number of unknowns and the functional model is linear, the maximum likelihood solution $\hat{x}$ for the unknowns can be found by minimizing the sum of squared residuals

$$\hat{v}^T \cdot W \cdot \hat{v} \rightarrow min. \tag{4.2}$$

In a closed form, it can be written as follows

$$\hat{x} = (A^T \cdot W \cdot A)^{-1} \cdot (A^T \cdot W \cdot l), \tag{4.3}$$

If the functional model $f(x)$ is non-linear, it can be linearised using a first-order Taylor series approximation at a vicinity point x_0, i.e., the initial value, as follows

$$f(x) = f(x_0) + \frac{\partial f}{\partial x} \cdot \delta x, \tag{4.4}$$

$$\hat{v} = A \cdot \delta\hat{x} - \delta l, \tag{4.5}$$

with

$$\delta l = l - f(x_0), \tag{4.6}$$

where A contains the partial derivatives of the functional model w.r.t the parameters at x_0, and δl is the vector of reduced observations, i.e. the observations minus the solution of $f(x)$ evaluated at x_0.
Eq 4.5 is a good approximation of eq 4.1, and the LSQ solution yields corrections $\delta\hat{x}$ to the initial values x_0. In order to obtain accurate estimates, one needs to iteratively calculate and apply corrections $\delta\hat{x}$ to the initial values x_0 until a pre-defined convergence threshold is met. One can, for example, stop the iteration when the change in the reference variance $\hat{\sigma}_0^2$ is below a threshold, e.g. 1%, since LSQ converges quadratically. The $\delta\hat{x}$ can be calculated using

$$\delta\hat{x} = (A^T \cdot W \cdot A)^{-1} \cdot (A^T \cdot W \cdot \delta l), \tag{4.7}$$

$$\hat{x} = x_0 + \delta\hat{x}, \tag{4.8}$$

$$\hat{\sigma}_0^2 = \frac{\hat{v}^T \cdot W \cdot \hat{v}}{dof}, \tag{4.9}$$

with

$$dof = n - m, \tag{4.10}$$

where dof is the degree-of-freedom for the adjustment, i.e., the number of observations n minus

the number of unknowns m.
The uncertainty of the estimate $\hat{\sigma}_{ii}$ can be calculated using

$$\hat{\sigma}_{ii} = \hat{\sigma}_0 \sqrt{Q_{ii}}, \tag{4.11}$$

with

$$Q_{xx} = (A^T \cdot W \cdot A)^{-1}, \tag{4.12}$$

Where Q_{xx} is the variance co-variance matrix of the estimates, Q_{ii} is the i^{th} diagonal element in Q_{xx} corresponding to x_i.
In the case of introducing relative constraints between the parameters as pseudo-observations, e.g. see Sec. 4.1.1, one can obtain the corrections $\delta\hat{x}$ from LSQ, and the aposteriori variance $\hat{\sigma}_0^2$ using

$$\delta\hat{x} = (A^T \cdot W \cdot A + H^T \cdot W_c \cdot H)^{-1} \cdot (A^T \cdot W \cdot \delta l + H^T \cdot W_c \cdot h), \tag{4.13}$$

$$\hat{\sigma}_0^2 = \frac{\hat{v}^T \cdot W \cdot \hat{v} + \hat{v_c}^T \cdot W_c \cdot \hat{v_c}}{dof}, \tag{4.14}$$

with

$$\hat{v_c} = H \cdot \delta\hat{x} - h, \tag{4.15}$$

$$dof = n - m + u, \tag{4.16}$$

where H is the design matrix of the constraint equations, W_c is the weight matrix of the pseudo-observations, h is the vector of the pseudo-observations, and u is the number of relative constraints.
The uncertainty of the estimate $\hat{\sigma}_{ii}$ can be calculated using

$$\hat{\sigma}_{ii} = \hat{\sigma}_0 \sqrt{Q_{ii}}, \tag{4.17}$$

with

$$Q_{xx} = (A^T \cdot W \cdot A + H^T \cdot W_c \cdot H)^{-1}, \tag{4.18}$$

where Q_{xx} is the variance co-variance matrix of the estimates, Q_{ii} is the i^{th} diagonal element in Q_{xx} corresponding to x_i.
In some cases, for example, see VGOS instrumental offset in Sec. 4.1.1, one needs to solve Eq. 4.1 under a condition. This can be performed, for example, using Helmert's method (Ghilani, 2017). In general, the conditions between the parameters can be expressed as

$$c(\hat{x}) = 0 \tag{4.19}$$

This condition equation can be linearised using Taylor series approximation at a vicinity point x_0 as follows

$$C \cdot \delta\hat{x} = b_c \tag{4.20}$$

with

$$b_c = -c(x_0) \tag{4.21}$$

where C is the design matrix of the condition equations, and b_c is the reduced vector of the condition equations.
The LSQ solution can be obtain using

$$\begin{bmatrix} \delta\hat{x} \\ p \end{bmatrix} = \begin{bmatrix} A^T \cdot W \cdot A + H^T \cdot W_c \cdot H & C^T \\ C & 0 \end{bmatrix}^{-1} \cdot \begin{bmatrix} A^T \cdot W \cdot \delta l + H^T \cdot W_c \cdot h \\ b_c \end{bmatrix}, \tag{4.22}$$

where $\delta\hat{x}$ represents the corrections to the initial values x_0, and p is a place holder corresponding to the condition equations.

The degree of freedom will be reduced by the number of conditions one introduces, and the uncertainty of the estimates can be calculated using eq 4.17.

4.1.1 Functional Model for VLBI/VGOS-derived VTEC

The sum of electrons along the signal path in the ionosphere in the direction from the radio to the antenna is referred to as the slant total electron content $STEC^{'}$. Since geodetic VLBI is a differential technique, the ionospheric delay (τ_{ion}) in each observation is proportional to the difference in $STEC^{'}$ of the two antennas forming a baseline. In order to obtain the so-called vertical total electron content ($VTEC^{'}$), the $STEC^{'}$ can be projected into the vertical direction at the ionospheric pierce point (IPP) using the modified mapping function (mf) and assuming a thin shell approximation of the ionosphere at an altitude of 450 km (Schaer, 1999; Hobiger et al., 2006; Petit and Luzum, 2010; Dettmering et al., 2011b). The mathematical relationship between τ_{ion} and $VTEC^{'}$ for VLBI/VGOS can be expressed as follows

$$\tau_{ion} = \frac{40.3}{f^2}[mf(\varepsilon_j)V_j^{'} - mf(\varepsilon_i)V_i^{'}] + I_j - I_i, \tag{4.23}$$

with

$$mf(\varepsilon_i) = \frac{1}{\sqrt{1 - \left(\frac{Rcos(\varepsilon_i)}{R+h}\right)^2}}, \tag{4.24}$$

where f is the reference frequency for VGOS observation and the effective frequency for VLBI observation. V_i and V_j are VTEC at antenna i and j respectively, and ε is the elevation angle of the radio source at VLBI/VGOS station. I_i and I_j are instrumental offsets of the antennas, and are introduced to absorb all potential errors / delays stemming from the antenna. These offsets are assumed to be constant over the 24-hour session, and are derived in the adjustment process. R is the mean radius of Earth, i.e., 6371 km, h is the height of the ionospheric layer, and α is a modifying factor. For the purpose of this thesis, a value of 506.7 and 0.9782 was used for h and α, respectively (Hugentobler et al., 2002; Dettmering et al., 2011b).
The introduction of instrumental offsets to the LSQ adjustment results in a rank deficiency in the design matrix A. To address this problem, one can choose to apply one of two options which are mathematically equivalent. The first option is to fix the instrumental offset of one antenna in the network and estimate the instrumental offsets of the remaining antennas w.r.t. the specified antenna. This would require removing the corresponding column in the A matrix. The second option is to introduce a condition that the sum of instrumental offsets in the

network is equal to zero (Sekido et al., 2003)

$$\sum_{i=1}^{s} I_i = 0, \tag{4.25}$$

where s represents the number of stations in the network.
$VTEC^{'}$ at IPP can be further expressed as a $VTEC$ above the telescope, considering the spatial difference in latitude and longitude between IPP and the telescopes (Hobiger et al., 2006). The latitudinal difference ($\delta\phi$) is geometrically related to the location of the telescope and is assumed to be constant during the 24-hour session. It can be modelled with two gradients, i.e., G_n in the north direction, and G_s in the south direction. If the latitude of IPP calculated for certain observation is greater than the latitude of the telescope, the corresponding observation contributes to the estimation of G_n. Otherwise, it contributes to the estimation of G_s. The longitudinal difference ($\delta\lambda$) is however temporally related to the location of the telescope. Since the temporal behaviour of the ionosphere is strongly correlated with the position of the Sun, it is assumed that the ionosphere remains constant during the relatively short period of time that Earth takes to rotate by the difference in longitudes. In other words, the epoch of the observation is shifted forward or backward in time until the difference in longitude ($\delta\lambda$) is zero (Hobiger et al., 2006; Dettmering et al., 2011b).
Throughout the course of the session, VLBI/VGOS observations are carried out at different elevation angles allowing therefore to separate parameters of different nature in the adjustment process. For a given observation, the mathematical relation between $VTEC^{'}$ at IPP and $VTEC$ at the VLBI/VGOS telescope can be formulated as:

$$V_i^{'}(t) = \left(1 + (\phi^{'} - \phi) \begin{bmatrix} G_n \\ G_s \end{bmatrix}\right) V_i(t + (\lambda^{'} - \lambda)/15), \tag{4.26}$$

where $\phi^{'}$ and ϕ are the geographic, geomagnetic or modip latitudes of IPP and VLBI/VGOS station, respectively. The parameters $\lambda^{'}$ and λ are the geographic longitudes of IPP and VLBI/VGOS station, respectively, see Sec. 3.1.1. The t represents the VLBI/VGOS observation epoch.
To account for the time-variable behaviour in the ionosphere status at VLBI/VGOS sites, VTECs are further expressed as piece-wise linear (PWL) offsets estimated, for example, every 15, 30 or 60 minutes (Teke et al., 2009; Dettmering et al., 2011a,b). In the implemented algorithm, the default time resolution is 60 minutes, but one can adjust it according to the density of the observations. The PWL offsets can be written as follows:

$$V_i(t) = V_i(t_k) + \frac{t - t_k}{t_{k+1} - t_k} \left(V_i(t_{k+1}) - V_i(t_k)\right), \tag{4.27}$$

The partial derivatives of V_i w.r.t the PWL offsets can be written as follows:

$$\frac{\partial V_i(t)}{\partial V_i(t_k)} = 1 - \frac{t - t_k}{t_{k+1} - t_k}, \tag{4.28}$$

$$\frac{\partial V_i(t)}{\partial V_i(t_{k+1})} = \frac{t - t_k}{t_{k+1} - t_k}, \tag{4.29}$$

where t_k and t_{k+1} are the consecutive epochs at which the PWL offsets are estimated and which bound the epoch of the observation t.
The sub-design matrix A_i of antenna i could be written as follows

$$A_i = \begin{pmatrix} \frac{\partial \tau_{ion}(t)}{\partial V_i(t_1)} & \frac{\partial \tau_{ion}(t)}{\partial V_i(t_2)} & 0 & 0 & \dots & 0 & \frac{\partial \tau_{ion}(t)}{\partial G_n} & \frac{\partial \tau_{ion}(t)}{\partial G_s} & \frac{\partial \tau_{ion}(t)}{\partial I_i} \\ \vdots & \vdots & \vdots & \vdots & & \vdots & \vdots & \vdots & \vdots \\ 0 & \frac{\partial \tau_{ion}(t)}{\partial V_i(t_2)} & \frac{\partial \tau_{ion}(t)}{\partial V_i(t_3)} & 0 & \dots & 0 & \frac{\partial \tau_{ion}(t)}{\partial G_n} & \frac{\partial \tau_{ion}(t)}{\partial G_s} & \frac{\partial \tau_{ion}(t)}{\partial I_i} \\ \vdots & \vdots & \vdots & \vdots & \ddots & \vdots & \vdots & \vdots & \vdots \\ 0 & 0 & 0 & 0 & \dots & \frac{\partial \tau_{ion}(t)}{\partial V_i(t_m)} & \frac{\partial \tau_{ion}(t)}{\partial G_n} & \frac{\partial \tau_{ion}(t)}{\partial G_s} & \frac{\partial \tau_{ion}(t)}{\partial I_i} \end{pmatrix}. \tag{4.30}$$

When the number of observations per time interval is less than the number of parameters to be estimated, the design matrix A will be singular, and no unique solution will be thus available. This usually occurs when the time resolution is higher than the density of the observations. In order to address this problem, relative constraints are introduced between the offsets of each station, and they are applied as pseudo-observations in the adjustment process, see Sec. 4.1 (Teke et al., 2009). One can write the constraint equation as follows

$$\delta V_i(t_{k,k+1}) = V_i(t_{k+1}) - V_i(t_k) = 0. \tag{4.31}$$

One can also write the corresponding sub-constraint matrix H_i, which contains the derivatives of the the constraint equations w.r.t the offsets of each station, and the corresponding vector of reduced pseudo-observation h_i as follows

$$H_i = \begin{pmatrix} -1 & 1 & 0 & 0 & \dots & 0 & 0 \\ 0 & -1 & 1 & 0 & \dots & 0 & 0 \\ 0 & 0 & -1 & 1 & \dots & 0 & 0 \\ \vdots & \vdots & \vdots & \vdots & \ddots & \vdots & \vdots \\ 0 & 0 & 0 & 0 & \dots & -1 & 1 \end{pmatrix}, \tag{4.32}$$

$$h_i = \begin{pmatrix} \delta V_i(t_{1,2}) \\ \delta V_i(t_{2,3}) \\ \vdots \\ \delta V_i(t_{k,k+1}) \end{pmatrix}. \tag{4.33}$$

One can write the full-design matrix H of the constraint equations, and the full vector of the pseudo-observations h as follows

$$H = \begin{pmatrix} H_1 & 0 & 0 & 0 & 0 & \dots & 0 & 0 & 0 & 0 \\ 0 & 0 & 0 & 0 & H_2 & \dots & 0 & 0 & 0 & 0 \\ \vdots & \vdots & \vdots & \vdots & \vdots & \ddots & \vdots & \vdots & \vdots & \vdots \\ 0 & 0 & 0 & 0 & 0 & \dots & H_s & 0 & 0 & 0 \end{pmatrix}, \tag{4.34}$$

$$h = \begin{pmatrix} h_1 \\ h_2 \\ \vdots \\ h_s \end{pmatrix}, \tag{4.35}$$

where the zero columns in H correspond to G_n, G_s, I_i, and I_j. The s parameter represents the number of stations in the network.

4.1.2 Stochastic Model

The stochastic model describes the probabilistic behaviour of the observations, which are a realization of a random process and whose formal errors conform to the normal distribution. This model plays an important role in the adjustment process, where not only it determines how much corrections the different observations receive, but also it governs one's ability to identify and eliminate outliers in the observations. Thus, a careful attention should be paid

when defining the stochastic model. The standard approach is to use the inverse of the co-factor matrix Q_{ll} as the weight matrix W in the adjustment process, see Sec. 4.1. Assuming that there is no correlations between the observations, the co-factor matrix is defined as follows

$$Q_{ll} = \frac{1}{\sigma_0^2}\Sigma_{ll} = \frac{1}{\sigma_0^2}\begin{pmatrix} \sigma_1^2 & 0 & \dots & 0 \\ 0 & \sigma_2^2 & \dots & 0 \\ \vdots & \vdots & \ddots & \vdots \\ 0 & 0 & \dots & \sigma_n^2 \end{pmatrix} \tag{4.36}$$

$$W = {Q_{ll}}^{-1} = \begin{pmatrix} \frac{\sigma_0^2}{\sigma_1^2} & 0 & \dots & 0 \\ 0 & \frac{\sigma_0^2}{\sigma_2^2} & \dots & 0 \\ \vdots & \vdots & \ddots & \vdots \\ 0 & 0 & \dots & \frac{\sigma_0^2}{\sigma_n^2} \end{pmatrix} = \begin{pmatrix} w_{11} & 0 & \dots & 0 \\ 0 & w_{22} & \dots & 0 \\ \vdots & \vdots & \ddots & \vdots \\ 0 & 0 & \dots & w_{nn} \end{pmatrix} \tag{4.37}$$

where Σ_{ll} is the variance co-variance matrix of the observations. The σ_0^2 parameter represents the a-priori standard deviation of the unit weight, which is chosen such that the elements of Q_{ll} is close to 1 so as to stabilize the numerical solution of LSQ.
Observations made at low elevation angles have higher uncertainty than those made at high elevation angles. The formal errors of the ionospheric delays (dTEC), which are obtained at the post-correlation analysis of VGOS measurements, do not reflect this. To account for that, one can consider an elevation-dependent weighting (EDW) using, for instance, a sine function as a scaling factor. This sine function yields a factor of 1 for elevation angle $\epsilon = \pi/2$ and 0 for elevation angle $\epsilon = 0$ with smooth transition in between. For a baseline ij and a radio source k , this function can be written as follows

$$s_{ij}^k = \sin\epsilon_i^k \sin\epsilon_j^k = \cos(\frac{\pi}{2} - \epsilon_i^k)\cos(\frac{\pi}{2} - \epsilon_j^k), \tag{4.38}$$

As the pseudo-observations were introduced as relative constraints between the offsets, one can control how tight those constraints are using the standard deviation σ_c of the pseudo-observations (Teke et al., 2009). The smaller the standard deviation is, the tighter the constraints are. Assuming that there is no correlation between the pseudo-observations, one can write the weight matrix W_c of the pseudo-observations as follows

$$W_c = \begin{pmatrix} \frac{1}{\sigma_c^2} & 0 & \dots & 0 \\ 0 & \frac{1}{\sigma_c^2} & \dots & 0 \\ \vdots & \vdots & \ddots & \vdots \\ 0 & 0 & \dots & \frac{1}{\sigma_c^2} \end{pmatrix} \tag{4.39}$$

However, different group of observations, defined, for example, by radio source and/or baseline, may have different levels of precision. Thus, it is not realistic to estimate only one variance of unit weight σ_0^2 for all observations. In order to refine the stochastic model, variance-component estimation (VCE) is introduced into the stochastic model, where individual variance component for each group of observation is estimated. The different groups are scaled by its corresponding factor, and then a new adjustment is performed. Next, one alternates between refining the stochastic model and performing the adjustment until all variance-components and the subsequent aposteriori unit of weight reach 1. It is noteworthy that VCE is sensitive to the presence of outliers in the data; thus, it should be done on outlier-free data. (Koch and Kusche, 2002; Guillaume, 2017). The new weight matrix W can be written as follows

$$W = \begin{pmatrix} \frac{1}{\sigma_{0_1}^2} W_1 & & & & & \\ & \frac{1}{\sigma_{0_2}^2} W_2 & & & & \\ & & \ddots & & & \\ & & & \frac{1}{\sigma_{0_k}^2} W_k & & \\ & & & & \ddots & \\ & & & & & \frac{1}{\sigma_{0_N}^2} W_N \end{pmatrix}, \tag{4.40}$$

with

$$\sigma_{0_k}^2 = \frac{v_k^T W_k v_k}{Tr(R_k)}, \tag{4.41}$$

$$R_k = Q_{vv_k} \cdot W_k, \tag{4.42}$$

where R_k, Q_{vv_k} and W_k are the redundancy matrix, the variance covariance matrix, and the

weight matrix of the residuals for observation group k, respectively. The parameters $\sigma^2_{0_k}$ and v_k are the variance component and the vector of residuals for group k, respectively. $Tr(R_k)$ is the trace of R_k, and $1/\sigma^2_{0_k}$ is the scale factor for group k.

4.1.3 Data Snooping

Observations with the largest residuals are not necessarily outliers because outliers heavily influence the LSQ solution. Thus, residuals could be misleading when used solely to identify outliers. To address this problem and eliminate all significant outliers, data snooping is introduced into the algorithm. It is based on a statistical hypothesis testing with a rejection criteria of 3.29, corresponding to $\alpha = 0.001$ and $\beta = 0.8$ (Ghilani, 2017). The starting point is a conventional LSQ. Then, one calculates the standardized residual $\hat{v}_i$ from the residual v_i and the variance covariance matrix of the residuals Q_{vv} as follows:

$$Q_{vv} = W^{-1} - A \cdot Q_{xx} \cdot A^T, \tag{4.43}$$

$$\hat{v}_i = \frac{|v_i|}{\sqrt{q_{ii}}}, \tag{4.44}$$

Next, one locates the largest standardized residual and checks whether it is larger than the rejection criteria 3.29 σ_0, where 3.29 corresponds to a 99.9% level of confidence and a significance level of $\alpha = 0.001$.

$$\hat{v}_i > 3.29\sigma_0, \tag{4.45}$$

If it is larger, one then excludes the corresponding observation from the dataset and performs again the adjustment. Finally, one repeats the last three steps until no more possible outliers are detected. The implemented algorithm is shown in Fig. 4.5.

4.1.4 Functional and Stochastic Models for VTEC from GNSS observations

The functional model for GNSS-derived VTECs is slightly different from the functional model for VLBI/VGOS-derived VTECs. First, the temporal behavior of the ionosphere in the East-West direction in this thesis is represented as a gradient instead of shifting the observations forward or backward in time, as in the case of VLBI/VGOS observations. Second, the model is linear, and thus there is no need for iteration in the LSQ adjustment. Third, there is no

need for relative constraints between the PWL offsets of VTECs since GNSS observations are available continuously and usually there are no major data gaps. For GNSS, the $STEC$ along the signal path between the satellite and the receiver can be formulated as:

$$S_i^{'}(t) = mf(\epsilon_i) \left(V_i + (\phi^{'} - \phi) \begin{bmatrix} G_n \\ G_s \end{bmatrix} (\lambda^{'} - \lambda) \begin{bmatrix} G_e \\ G_w \end{bmatrix} \right), \tag{4.46}$$

where $S_i^{'}$ refers to $STEC$ at IPP, $mf(\epsilon_i)$ is the mapping function of $STEC$ to $VTEC$ at IPP, V_i represents $VTEC$ above the receiver, $\phi^{'}$ and $\lambda^{'}$ are the latitude and longitude of IPP in radian, ϕ and λ are the latitude and longitude of the receiver, G_n and G_s are the ionospheric gradients in the North and South directions, and G_e and G_w are the ionospheric gradients in the East and West directions. In this thesis, the gradients are assumed to remain constant over the period of 24 hours (Julien et al., 2012).
Using the PWL function, V_i in relation to GNSS observation can be written as follows

$$V_i(t) = V_i(t_k) + \frac{t - t_k}{t_{k+1} - t_k} (V_i(t_{k+1}) - V_i(t_k)), \tag{4.47}$$

The partial derivatives of $S_i^{'}$ w.r.t to the PWL offsets and the gradients can be expressed as

$$\frac{\partial S_i^{'}(t)}{\partial V_i(t_k)} = 1 - \frac{t - t_k}{t_{k+1} - t_k}, \tag{4.48}$$

$$\frac{\partial S_i^{'}(t)}{\partial V_i(t_{k+1})} = \frac{t - t_k}{t_{k+1} - t_k}, \tag{4.49}$$

$$\frac{\partial S_i^{'}(t)}{\partial G_n} = \frac{\partial S_i^{'}(t)}{\partial G_s} = \phi^{'} - \phi, \tag{4.50}$$

$$\frac{\partial S_i^{'}(t)}{\partial G_e} = \frac{\partial S_i^{'}(t)}{\partial G_w} = \lambda^{'} - \lambda, \tag{4.51}$$

where t_k and t_{k+1} are the consecutive epochs at which the offsets are estimated. The epoch of the observation t lies in between t_k and t_{k+1}.
The sub-design matrix A_i of receiver i could be written as follows

$$A_i = \begin{pmatrix} \frac{\partial S_i'(t)}{\partial V_i(t_1)} & \frac{\partial S_i'(t)}{\partial V_i(t_2)} & 0 & 0 & \dots & 0 & \frac{\partial S_i'(t)}{\partial G_n} & \frac{\partial \S_i'(t)}{\partial G_s} & \frac{\partial \S_i'(t)}{\partial G_e} & \frac{\partial \S_i'(t)}{\partial G_w} \\ \vdots & \vdots & \vdots & \vdots & & \vdots & \vdots & \vdots & \vdots & \vdots \\ 0 & \frac{\partial S_i'(t)}{\partial V_i(t_2)} & \frac{\partial S_i'(t)}{\partial V_i(t_3)} & 0 & \dots & 0 & \frac{\partial S_i'(t)}{\partial G_n} & \frac{\partial S_i'(t)}{\partial G_s} & \frac{\partial \S_i'(t)}{\partial G_e} & \frac{\partial \S_i'(t)}{\partial G_w} \\ \vdots & \vdots & \vdots & \vdots & \ddots & \vdots & \vdots & \vdots & \vdots & \\ 0 & 0 & 0 & 0 & \dots & \frac{\partial S_i'(t)}{\partial V_i(t_m)} & \frac{\partial S_i'(t)}{\partial G_n} & \frac{\partial S_i'(t)}{\partial G_s} & \frac{\partial \S_i'(t)}{\partial G_e} & \frac{\partial \S_i'(t)}{\partial G_w} \end{pmatrix}. \tag{4.52}$$

$$A = \begin{pmatrix} A_1 & 0 & \dots & 0 \\ 0 & A_2 & \dots & 0 \\ \vdots & \vdots & \ddots & \vdots \\ 0 & 0 & \dots & A_n \end{pmatrix}, \tag{4.53}$$

Regarding the stochastic model, one can use unit weighting as a rudimentary assumption in relation to the GNSS observations and VTEC time series.

4.2 Implementation

The code has been developed by the author of the thesis an open-source python library to be further extended for other space-geodetic techniques, such as satellite altimetry and DORIS. The pipeline so far supports 24-hour VGOS sessions, 24-hour geodetic VLBI sessions and GNSS observations (provided as text files with predefined format). The following subsections describe the processing pipeline and its main modules.

4.2.1 Processing Pipeline

The input to the pipeline is the starting and ending dates of the time windows to be searched for VGOS 24-hour sessions. The user can also set some other parameters as discussed in the following sections. The first element in the pipeline is the download module, which accesses the defined target repositories to acquire files such as 24-hour VGOS sessions, GIMs and Madrigal TEC maps. The second element is the pre-processing module, which loads and prepares VGOS data for further analysis. The third element is the data snooping module, which eliminates possible outliers from the data. The fourth element is the refinement module, which estimates the ionospheric parameters using LSQ with relative constraints and VCE. The fifth module is the plotting module, which plots the VGOS-derived VTECs complemented with the GNSS-derived VTECs extracted from GIMs and/or Madrigal TEC maps. The sixth module outputs ionospheric parameters in a text file and save it to a disk. The described procedure is depicted in Fig. 4.1.

4.2.2 Data Preparation and Prepossessing Module

This module is second in the processing pipeline, and the implemented algorithm of this module is depicted in 4.3. The input to the algorithm is the name of the VGOS session to be processed. The algorithm has two stages, i.e., data preparation and preprocessing, both of which has multiple steps. The data preparation starts with loading and extracting the data from the vgosDB database. Then, it filters the data using multiple criteria, such as the minimal cut-off elevation angle, signal-to-noise ratio, the minimum number of observations per radio source, and the problematic stations, as outlined in Sec. 3. The user can modify the parameters of these filters. Once the data preparation is complete, the algorithm proceeds to the data preprocessing, which begins with converting the the cartesian coordinates of VGOS sites to geographic latitudes and longitudes. Then, the module calculates the geographic latitude ϕ and longitude λ of IPP as pointed out in Sec. 3. Next, the algorithm can choose one of four processing options depending on the parameter settings.
The first option is to directly use the geographic latitudes and longitudes of IPP and VLBI/VGOS sites. The second option is to convert the latitudes of IPP and VGOS sites to geomagnetic lat-

itudes. This is straightforward as described in Sec. 3. In this case, the output of the algorithm are the geomagnetic latitudes and the geographic longitudes. The third option is to convert the latitudes to modip latitudes. For this, one needs the magnetic dips at IPP and VGOS sites, which can be obtained using two different methods. The first method spatially interpolates a dip grid of 2.5°-by-5° in latitude and longitude, respectively. This grid is generated from IGRF 13 using magnetic-field-calculator Python library (Filip, 2021). This grid is automatically generated and saved for the year corresponding to the session being processed. Thus, it can be used for other sessions carried out in the same year. The second method calculates the dips at the exact locations of IPP and VLBI/VGOS sites. The first method is faster while the second method is more accurate. The first method is the default one, but the user can choose to use the second method instead. In this case, the output of the algorithm are the modip latitudes and the geographic longitudes.

4.2.3 Download Module

The download algorithm is rather simple, and the high level overview of this part is depicted in Fig. 4.2. All the user needs is a good internet connection and to set a few parameters. The first two parameters are the starting and ending dates of the time window for 24-hour VGOS sessions to be searched. The third and fourth parameters are whether to download GIMs and Madrigal TEC maps corresponding to 24-hour VGOS sessions, respectively. Once these parameters are set, the algorithm accesses the defined target repositories to acquire these files and extracts them to the local disk.
By default, the algorithm downloads the final IGS solution. If this solution is not available, it searches for a final map from the other centers, such as UPC in Spain and, NRCan/Canada. If none of these solutions is available, it looks for a rapid solution from IGS. If this solution is not available, it searches for a rapid map from the different centers. If none of these is available, it looks for a 1-day predicted solution from IGS. If this solution is not available, it searches for a 1-day predicted solution from the other centers. If none of these solutions is available, it looks for a 2-day predicted solution from IGS. If this solution is not available, it searches for a 2-day predicted solution from the other centers.

4.2.4 The Basic LSQ Module

The basic LSQ algorithm is mainly used in the data snooping algorithm, see Sec. 4.2.5. The implemented algorithm is shown in Fig. 4.4. This algorithm starts with obtaining some initial values for the ionospheric parameters, which are chosen randomly. Then, it forms the design matrix A, the vector of reduced observations δl, and the weight matrix W. Next, it preforms an LSQ adjustment and adds the obtained corrections to the initial values. Once the new initial

values are calculated, it repeats the last two steps until the change in the reference variance falls below 1%.

4.2.5 Data Snooping Module

The data snooping algorithm is optional since it is computationally expensive and often unnecessary. In this algorithm, relative constraints are also not applied because the goal is to get rid of the bad data rather than estimating VTECs. The implemented algoritm is depicted in Fig. 4.5. The starting point of the algorithm is a conventional LSQ solution which comes from the basic LSQ algorithm. Then, it calculates the standardized residuals and checks whether the maximum standardized residual is above the rejection criteria, see Sec. 4.1. If this is the case, it excludes the observation corresponding to this residual from the VTEC estimation process, and it then repeats the last steps with the new dataset. Otherwise, the module declares that the data is outlier-free, and it passes this data to the refinement algorithm.

4.2.6 Refinement Module

The full LSQ algorithm lies at the heart of the processing pipeline. The default setting is to run the relative constraints and VCE, unless specified otherwise by the user. The input to the algorithm is basically the pre-processed data. If the user however chooses to run the data snooping algorithm, the input would be the outlier-free data. The implemented algorithm is shown in Fig. 4.6. This algorithm begins by choosing randomly some initial values for the ionospheric parameters. Then, it sets up the weight matrix W. Next, it forms the design matrix A and the vector of reduced observations δl. After this, it applies by the default the relative constraints between the linear offsets of VTECs. Then, it calculates corrections for the initial values and updates these initial values. Next, it repeats the steps starting from forming the design matrix A until the change in reference variance is below 1%. Then, it applies VCE and updates the weight matrix W. After this, it repeats the steps starting from forming the design matrix A until the reference variance is nearly one, i.e., $1 - \sigma_0^2 \geq 0.0001$. Finally, it outputs the estimated parameters along with their uncertainties.

4.2.7 GNSS Module

GNSS module is a rudimentary implementation for deriving VTEC time series from GNSS observations at the location of GNSS antenna with the aim of comparing the derived VGOS-based VTEC with an external source of such information. This module requires that the user downloads RINEX files and prepares the data in a certain format, see B1. The input to the algorithm are the STEC file and the file containing the station coordinates in WGS84. The algorithm has few steps, some of which are similar to the step of processing VGOS observations,

see Sec. 3.1.1 and 4.1. The first step is to extract the different types of data from the input files per station. The second step is to calculate the geographic latitude and longitude of IPP for each observation. The third step, which is optional, is to convert the latitudes of IPP and GNSS station to geomagnetic or modip latitudes. The fourth step is to form the design matrix and obtain the LSQ solution. The fifth step is to plot all VTEC time series per station and write the results into a text file. The implemented algorithm is shown in Fig. 4.7.

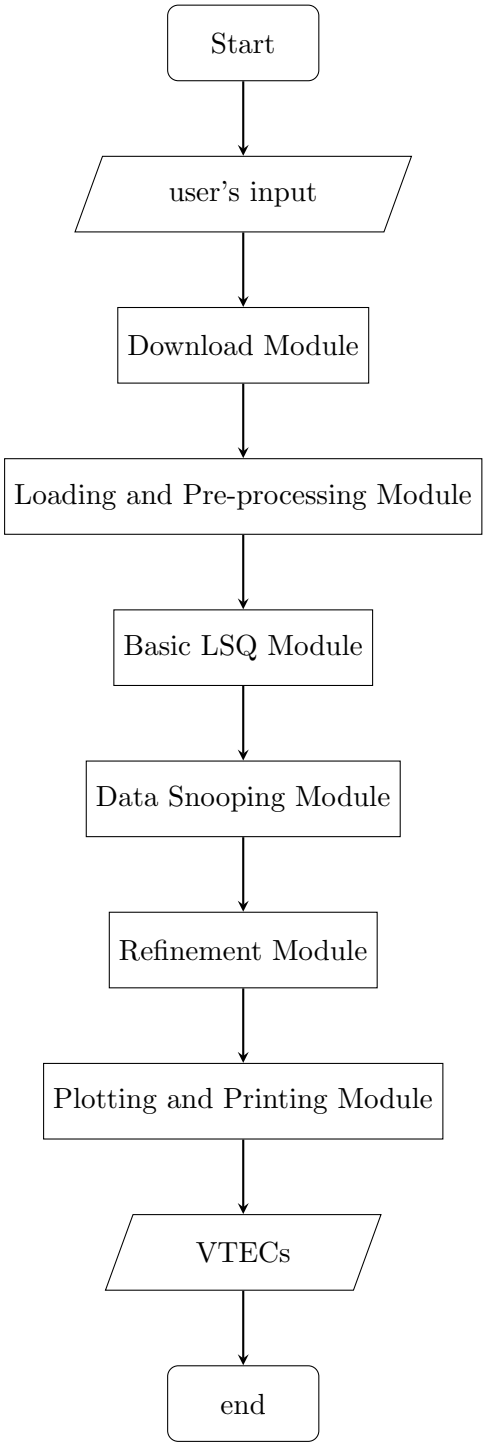

Figure 4.1: The processing pipleline for deriving VTEC time series above VLBI/VGOS stations

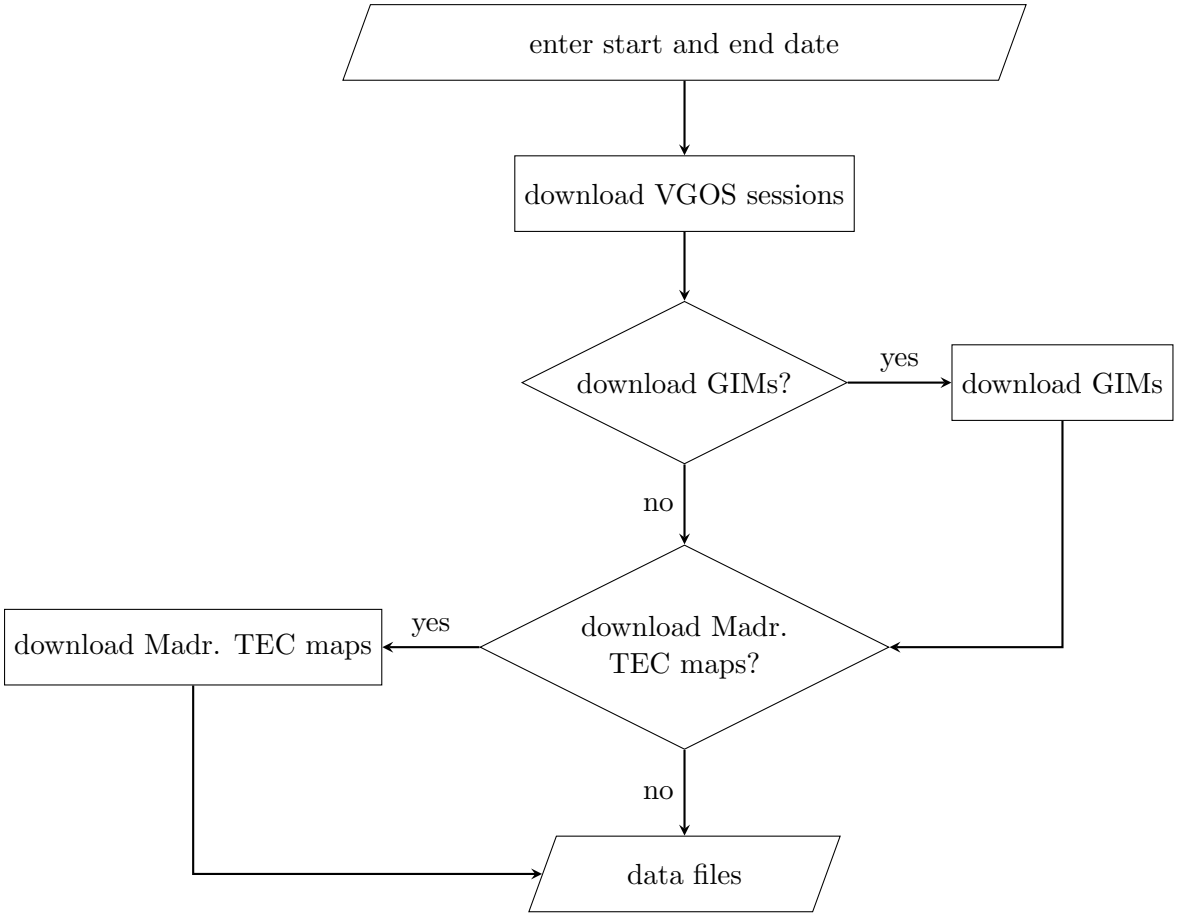

Figure 4.2: The algorithm for downloading 24-hour VGOS sessions and the corresponding GIMs and MTMs

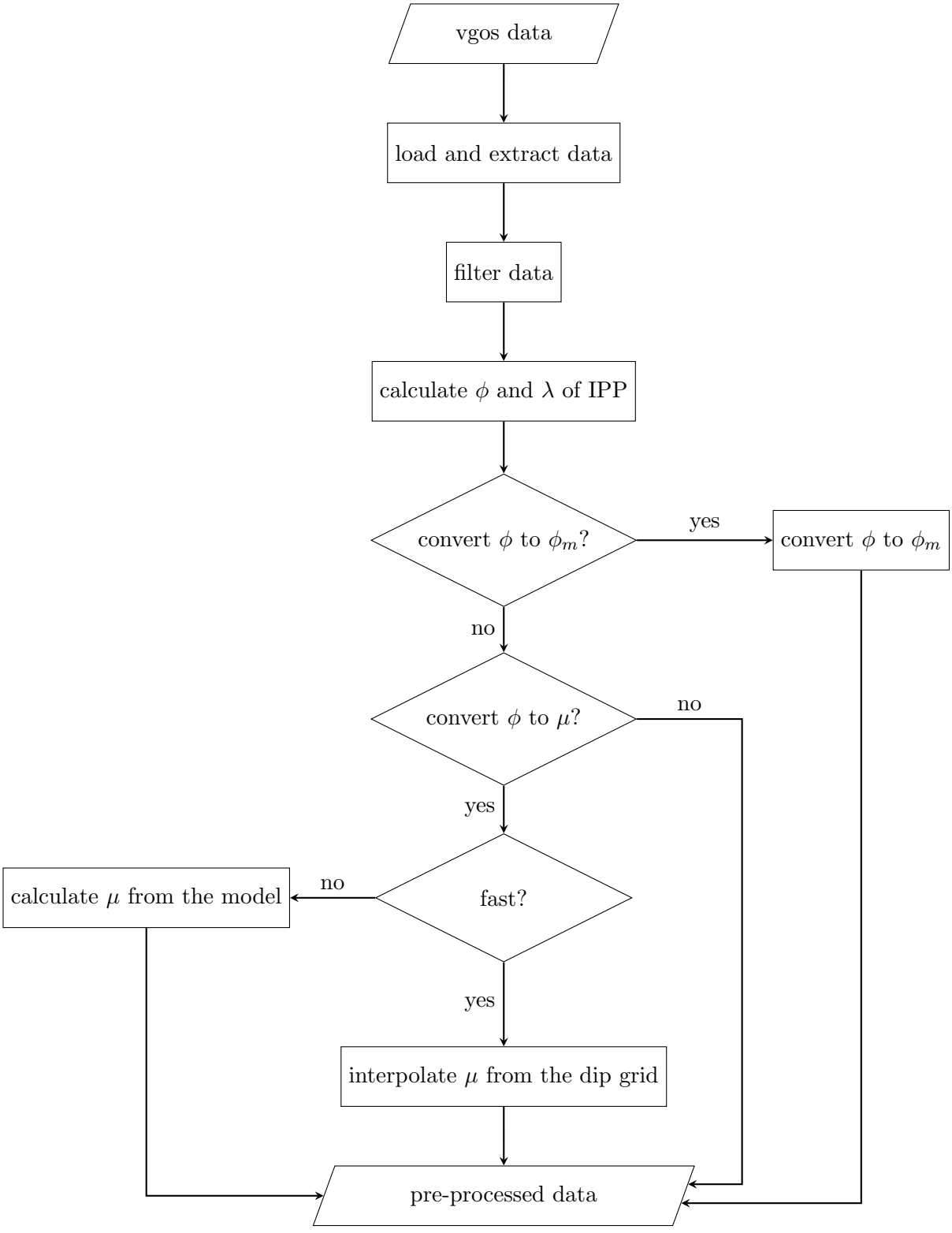

Figure 4.3: The data preparation and preprocessing algorithm for deriving VTECs above VGOS stations from 24-hour VGOS sessions

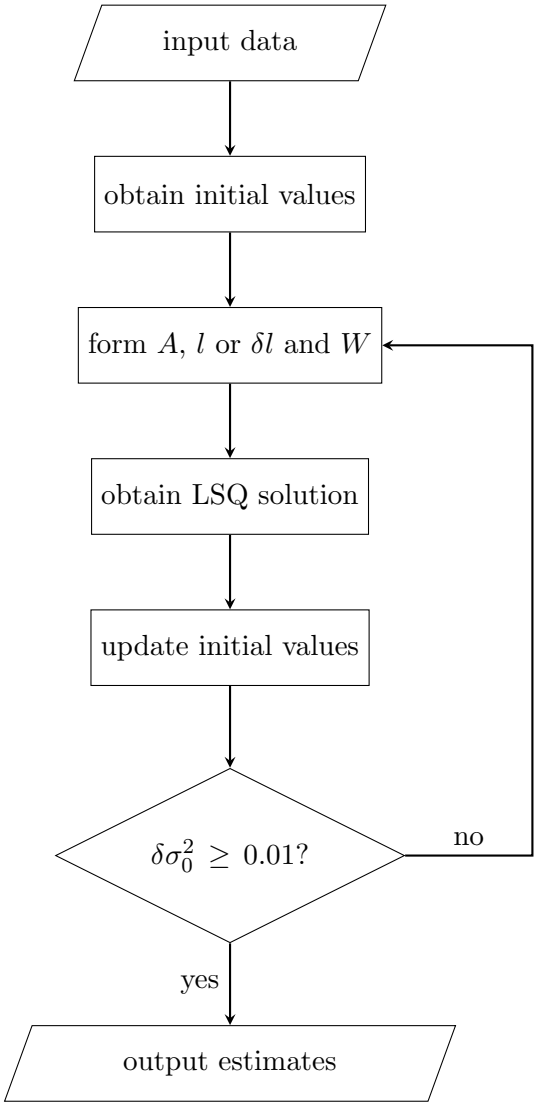

Figure 4.4: The basic LSQ algorithm used inside the data snooping algorithm, as depicted in Fig. 4.5.

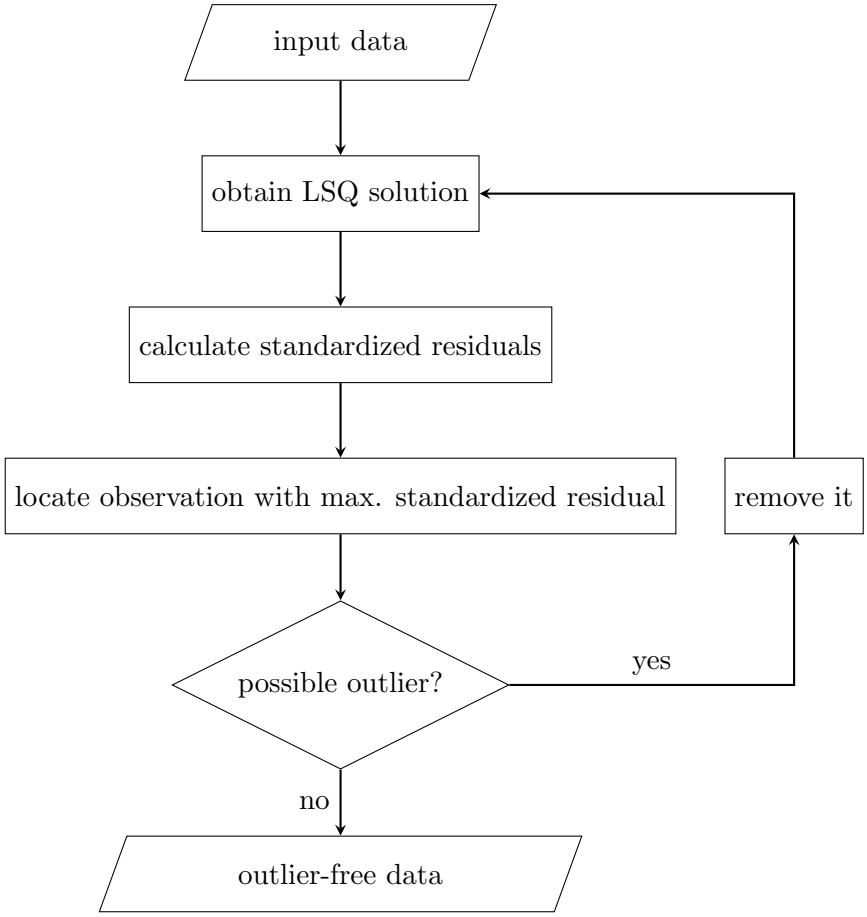

Figure 4.5: The data snooping algorithm for detecting and eliminating significant outliers in the VGOS-type observations

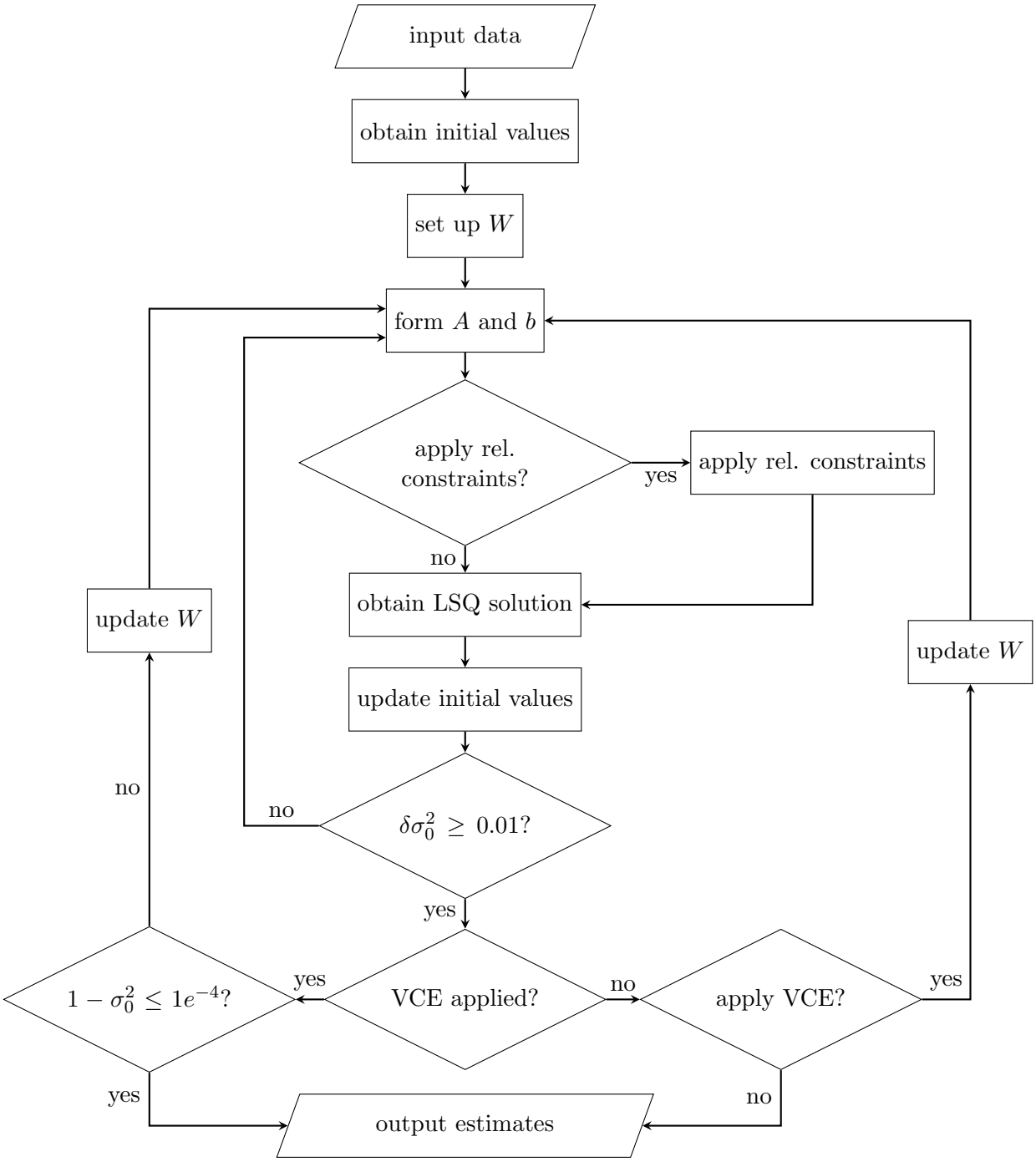

Figure 4.6: The refinement algorithm for estimating VTECs above VLBI/VGOS stations

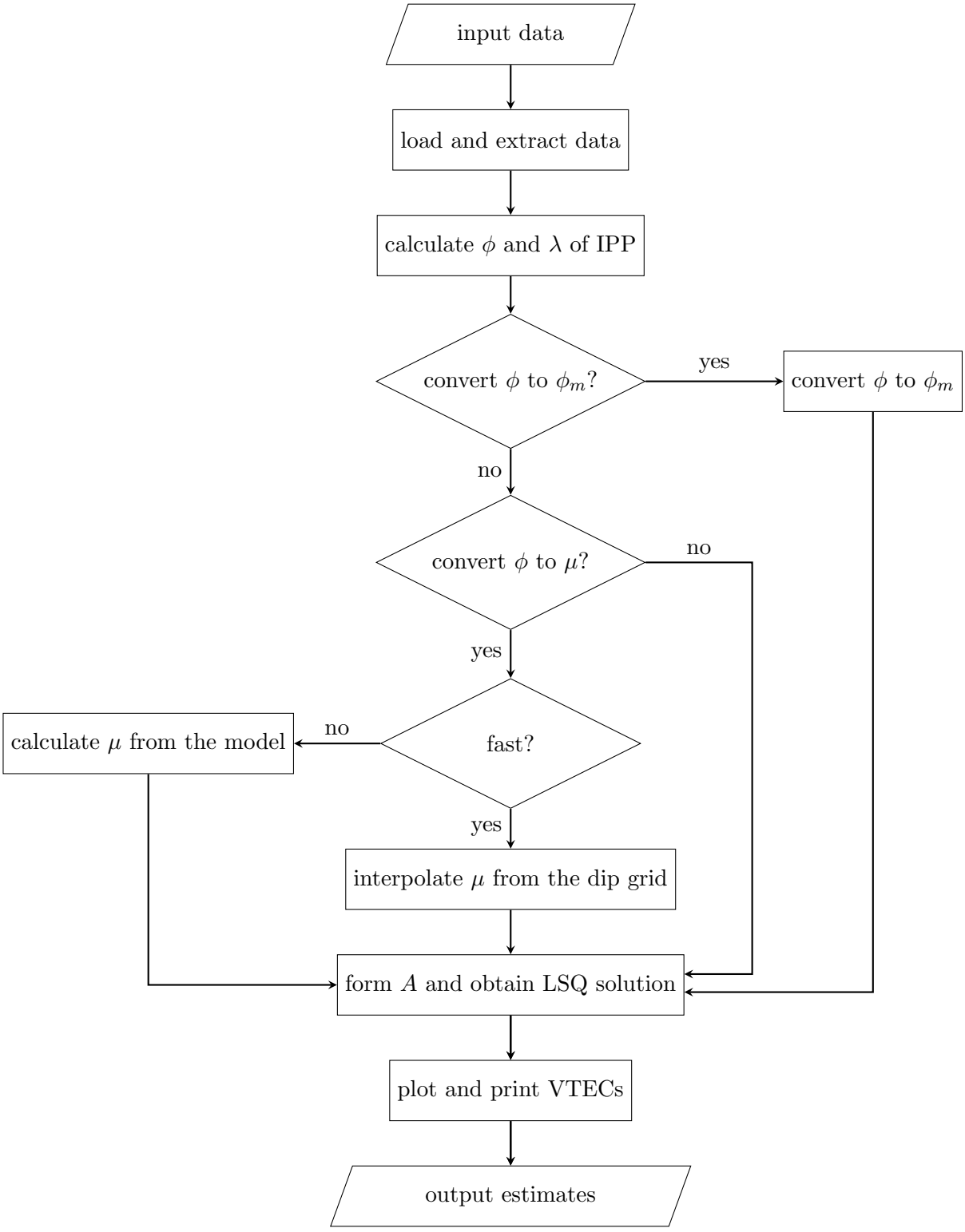

Figure 4.7: GNSS processing algorithm for obtaining VTECs from GNSS observations carried out with ground-based GNSS receivers

5 Results

In this work, VTEC time series were derived from geodetic VLBI and VGOS observations using a PWL function with 1-hour temporal resolution. Relative constraints were introduced between the PWL offsets in order to address data gaps. Further, two gradients, i.e, in north and south directions, were estimated assuming that they remain constant over the 24-hour period. In addition, the epoch of the observations were shifted backward and forward in time to account for the ionosphere dependency on the position of the Sun. Furthermore, modip latitudes for IPP and geodetic VLBI and VGOS sites were used to account for the dependency of the ionosphere on the Earth's magnetic field. In addition, the instrumental offsets were assumed to be constant during the 24-hour session. In the LSQ adjustment, these instrumental offsets were subjected to the condition that their sum equals to zero in the LSQ adjustment, see Sec. 4.1.1. Moreover, no correlation between the observations was assumed for the sake of simplicity. In addition, elevation-dependent weighting (EDW) was applied. Furthermore, variance components per radio source were estimated to account for the different level of accuracy for the observation groups of the different radio sources. Variance components per baseline were also estimated to account for the station dependency, see Sec. 4.1.2.
The parameterisation for deriving VTEC time series from GNSS observations is similar in some aspect to that for geodetic VLBI and VGOS. In this case PWL offsets with an 1-hour resolution were also applied. It is however slightly different in few aspects. First, four gradients instead of two, i.e., in north, south, east, and west directions, were estimated, and they are assumed to be constant for the time window corresponding to geodetic VLBI and VGOS sessions. In addition, no relative constraints between the PWL offsets were introduced since GNSS stations collect GNSS data continuously and no gaps were found in the used data. Finally, a unit weight matrix for all the observations was used, and no variance component per satellite and/or station was estimated for the sake of simplicity, see Sec. 4.1.4.
This chapter is organized as follows. First, VTEC time series derived from VGOS, VLBI, GNSS antennas at co-located sites as well as VTEC time series extracted from global ionosphere maps (GIMs) and Madrigal TEC maps (MTMs) are introduced in Sec. 5.1. Then, VTEC time series per station for three selected sessions are presented in Sec. 5.2. Next, the biases between VTEC time series derived from VGOS observations and extracted from GIMs and MTMs for all the 24-hour VGOS sessions are summarised in Sec. 5.3. Then, the instrumental offsets for all the sessions are presented in Sec. 5.5. Finally, the uncertainties of VTECs derived from VGOS observations for all the sessions are summarized in Sec. 5.6.

5.1 VGOS-derived VTEC Time Series I

In order to validate VGOS-derived VTECs, this subsection presents the comparison between the VTEC time series derived from VGOS observations, VTEC time series derived from geodetic VLBI and GNSS observations at co-located sites for the time window of session 19APR29XA, 19APR29XB, and 19APR29VG. It also presents the corresponding VTEC time series extracted from GIMS and MTMs.

Fig. 5.1 shows the VTEC time series of VGOS station KOKEE12M, VLBI station KOKEE, and GNSS station KOKV in green, red and black, respectively. In a similar fashion, Fig. 5.2 shows the VTEC time series of VGOS stations WETTZ13S, VLBI station WETTZ13N and WETTZELL, and GNSS station WTZZ. These two figures also show the VTEC time series from GIMs and MTMs in blue and grey, respectively. Since VTEC time series from MTMs are noisy, they were smoothed with the Savitzky–Golay filter. The smoothed MTMs (SMTMs) are then displayed in yellow. The x-axis shows the time in UTC hour while the y-axis shows the VTEC in TECU. In addition, the small bars on the time series of VGOS and VLBI stations represent the uncertainty of the corresponding VTECs. For each VGOS station, the RMS of the VTECs w.r.t. to the VTECs from the VLBI and GNSS stations as well as from GIMs and SMTMs are given on the right side of the corresponding figure.

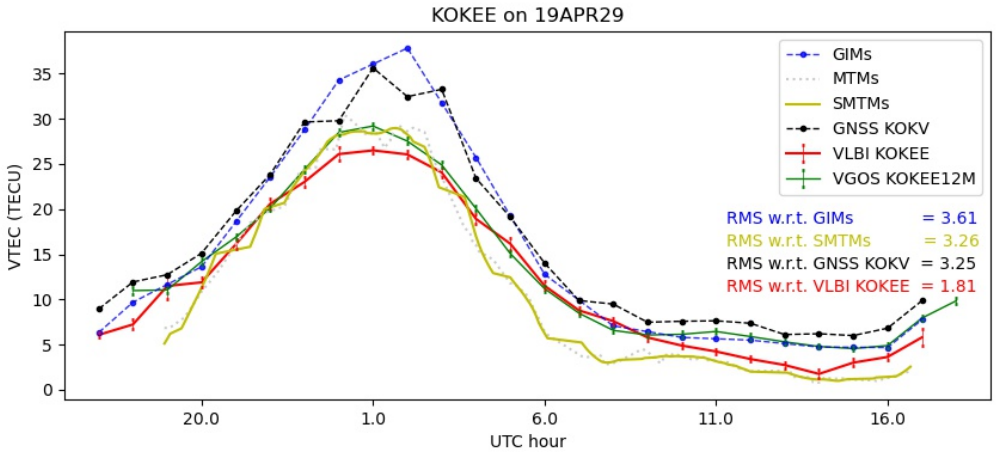

Figure 5.1: VTEC time series derived from VGOS, VLBI, and GNSS observations, and VTEC time series extracted from GIMs and MTMs at Kokee Park Geophysical Observatory between 17:00 UTC on 29/04/2019 and 18:00 UTC 30/04/2019

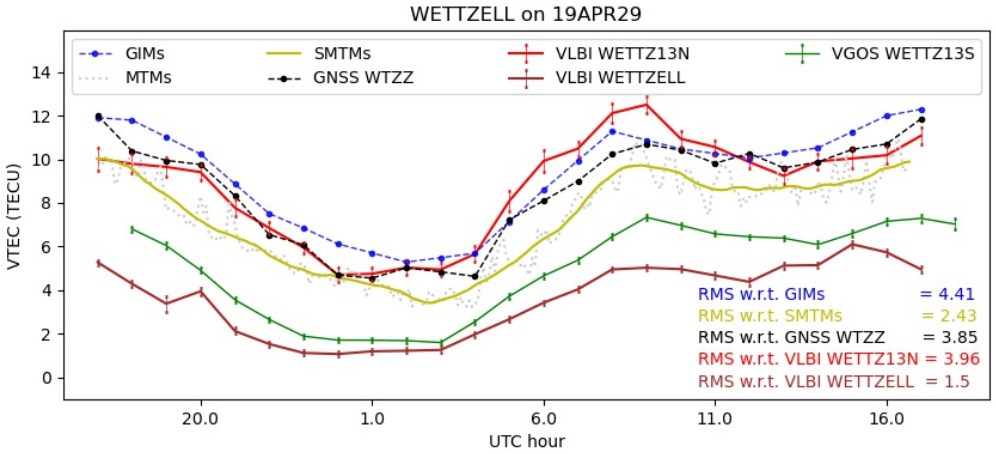

Figure 5.2: VTEC time series derived from VGOS, VLBI, and GNSS observations, and VTEC time series extracted from GIMs and MTMs at Geodetic Observatory Wettzell between 17:00 on 2019/04/29 and 18:00 2019/04/30

5.2 VGOS-derived VTEC Time Series II

In order to demonstrate the performance of VGOS stations and show the session-to-session variation concerning ionosphere above the considered VGOS stations, this section presents the VTEC time series of nine VGOS stations for three selected sessions.

In each sub-figure, the title consists of the station name and the session name, i.e., Year-Month-Day. In each plot, the x-axis shows the UTC time while the y-axis shows the VTEC in TECU. The VTEC time series derived from VGOS observations is displayed in green while the VTEC time series extracted from GIMs and MTMs is depicted in blue and grey, respectively. In addition, the smoothed MTMs (SMTMs) is visualised in yellow. In addition, the RMS differences of VTEC w.r.t. to GIMs and SMTMs is written in blue and yellow on each figure.

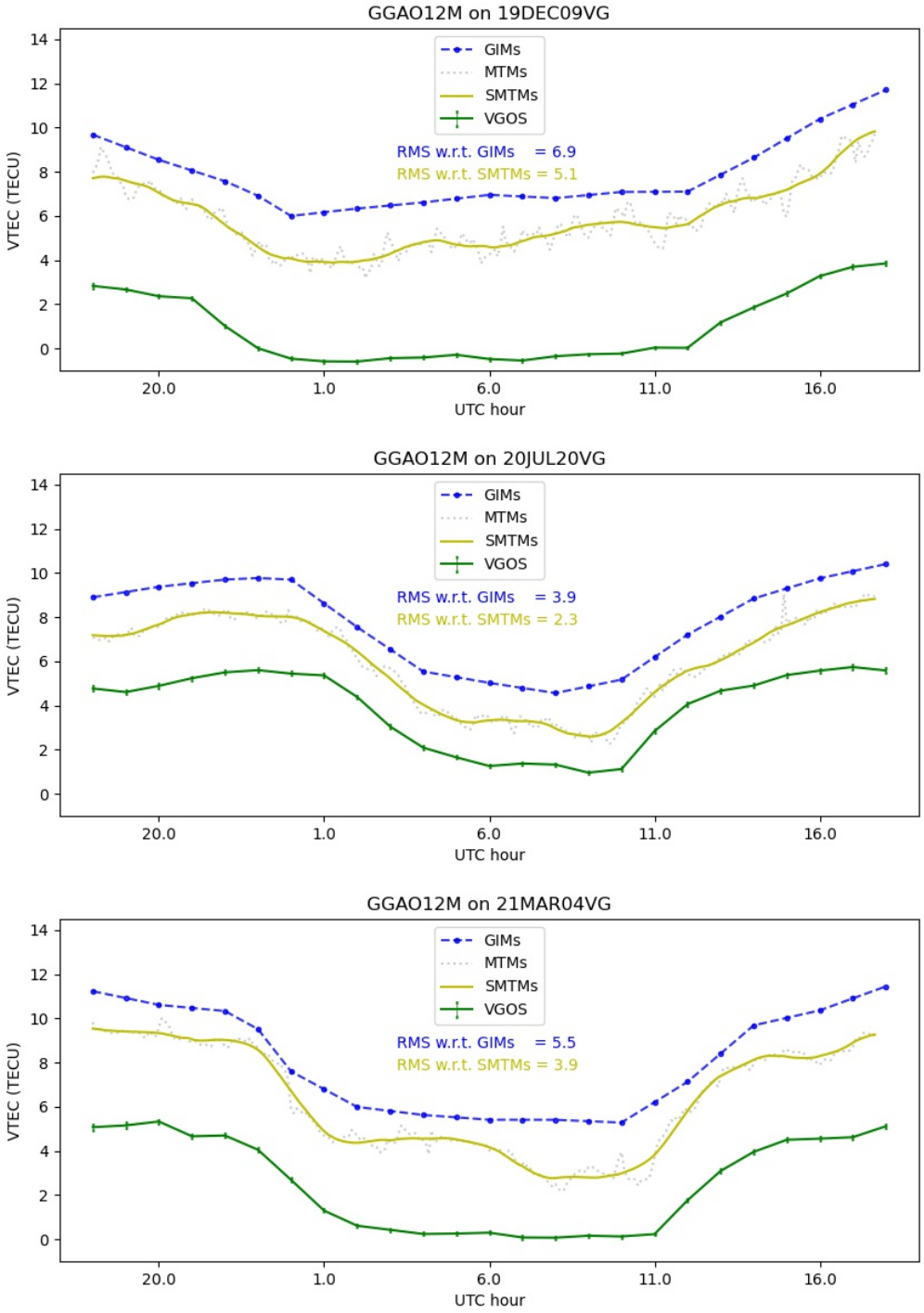

Figure 5.3: VTEC time series of GGAO12M from session 19DEC09VG (top), 20JUL20VG (middle), and 21MAR04VG (bottom)

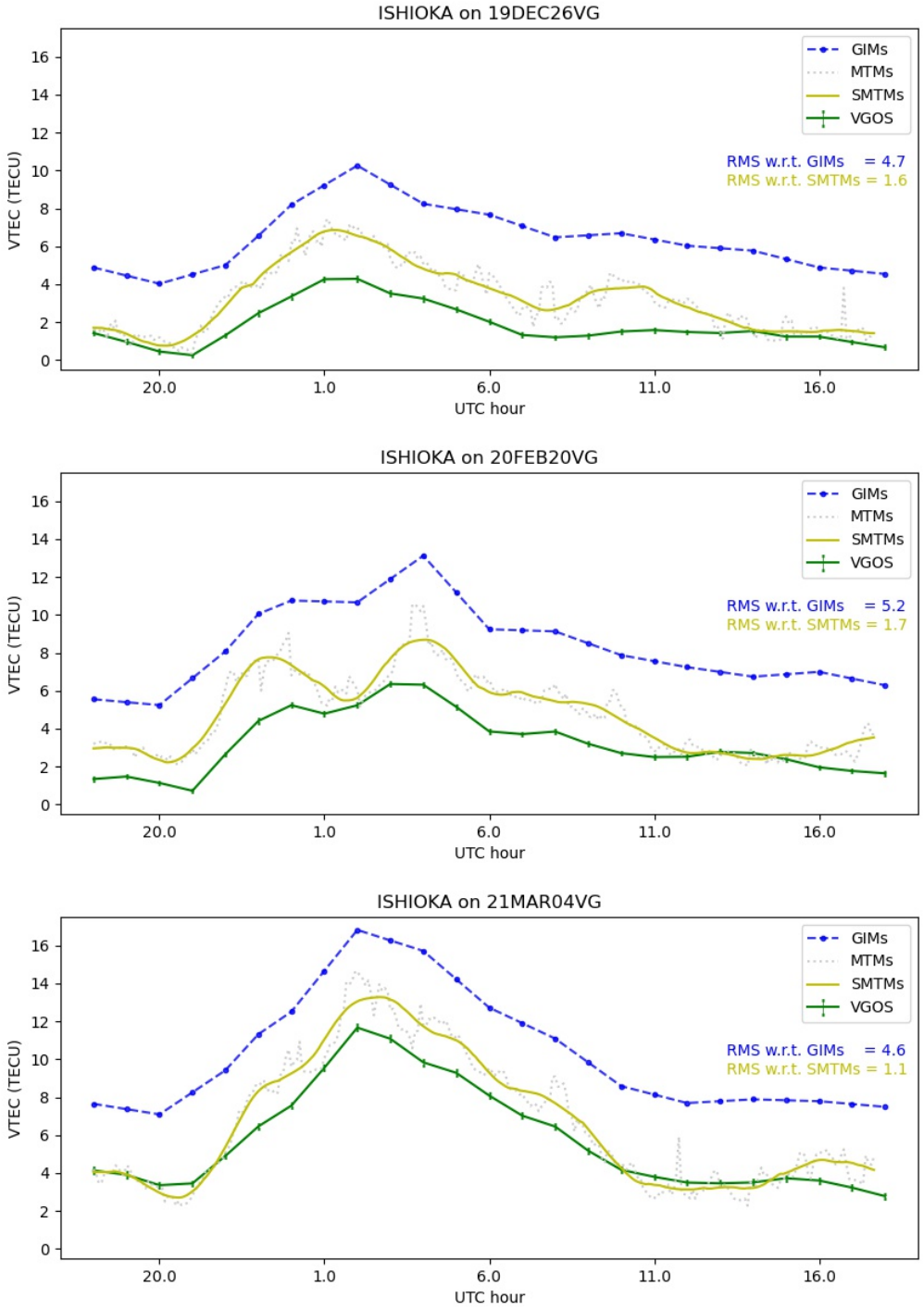

Figure 5.4: VTEC time series of ISHIOKA from session 19DEC26VG (top), 20FEB20VG (middle), and 21MAR04VG (bottom)

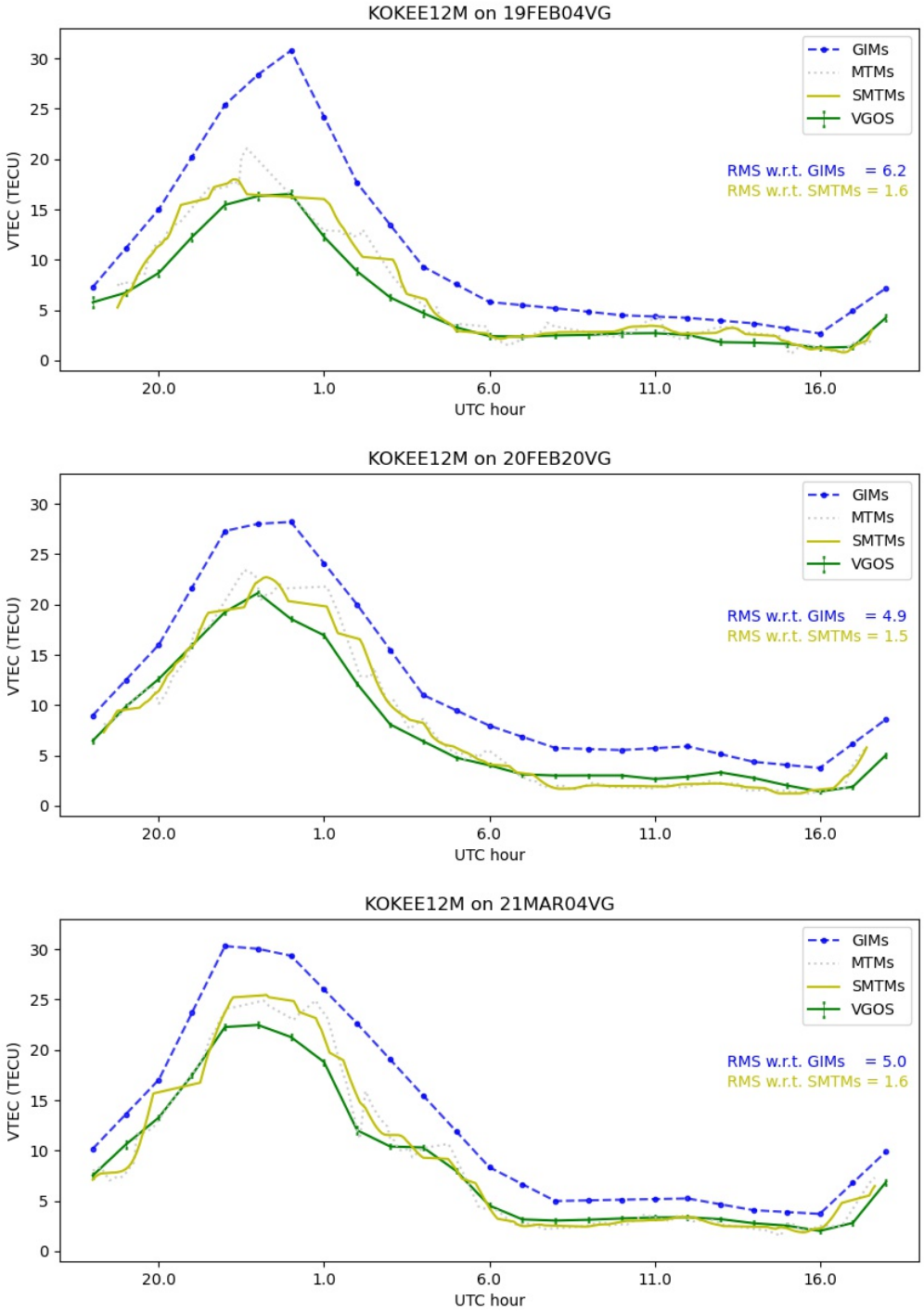

Figure 5.5: VTEC time series of KOKEE12M from session 19FEB04VG (top), 20FEB20VG (middle), and 21MAR04VG (bottom)

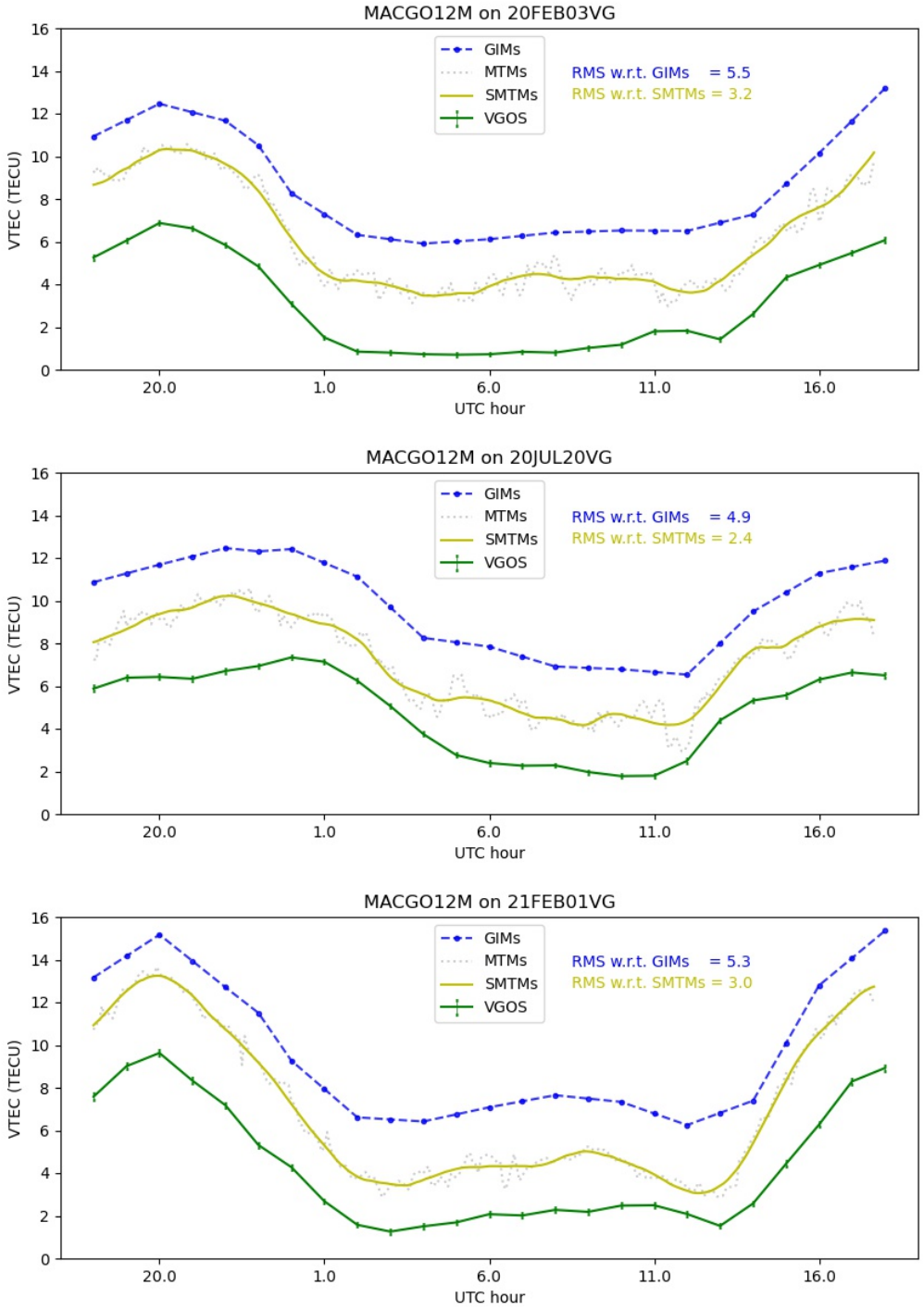

Figure 5.6: VTEC time series of MACGO12M from session 20FEB03VG (top), 20JUL20VG (middle), and 21FEB01VG (bottom)

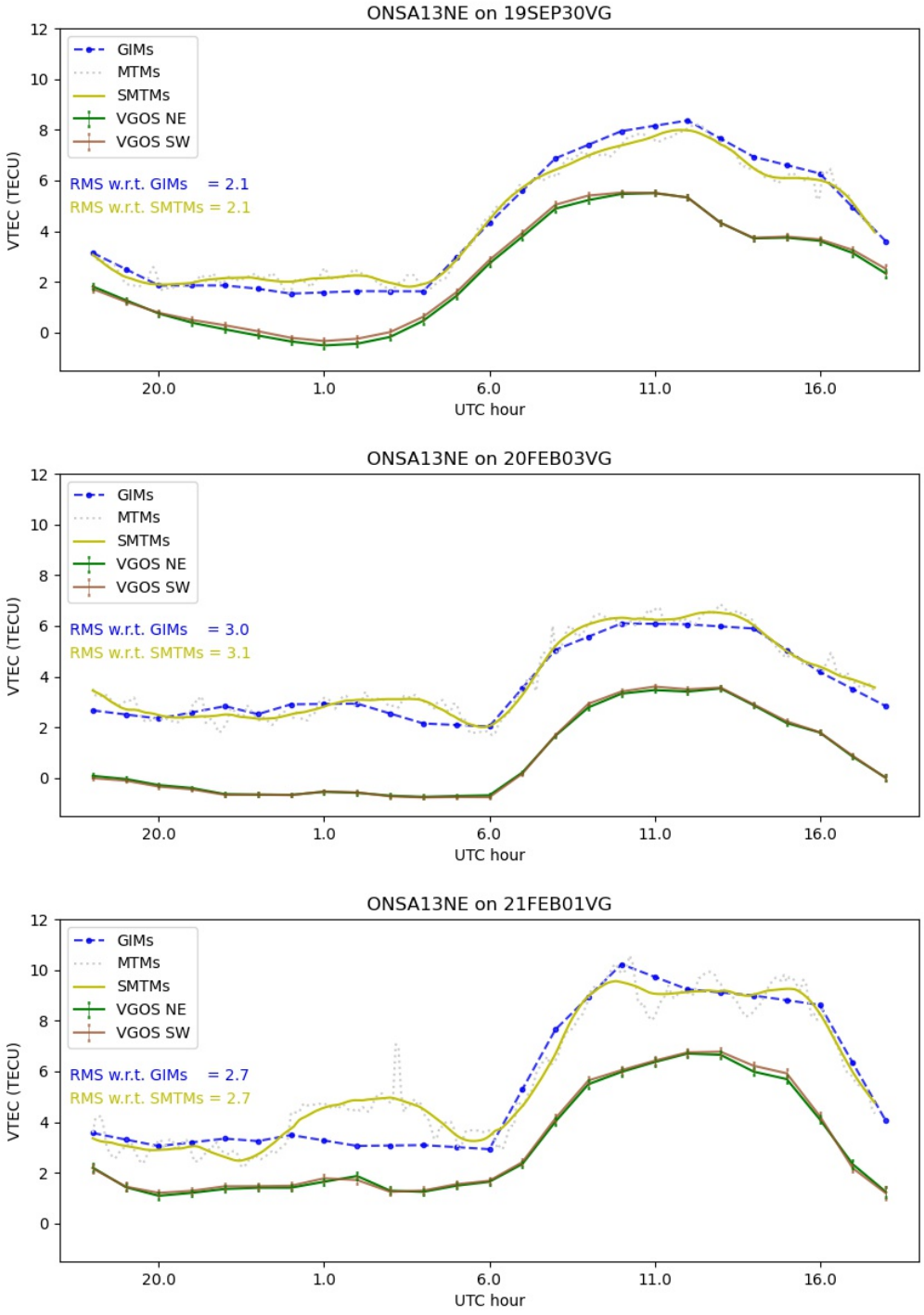

Figure 5.7: VTEC time series of ONSA13SW (in green) and ONSA13SW (in sienna) from session 19SEP30VG (top), 20FEB03VG (middle), and 21FEB01VG (bottom)

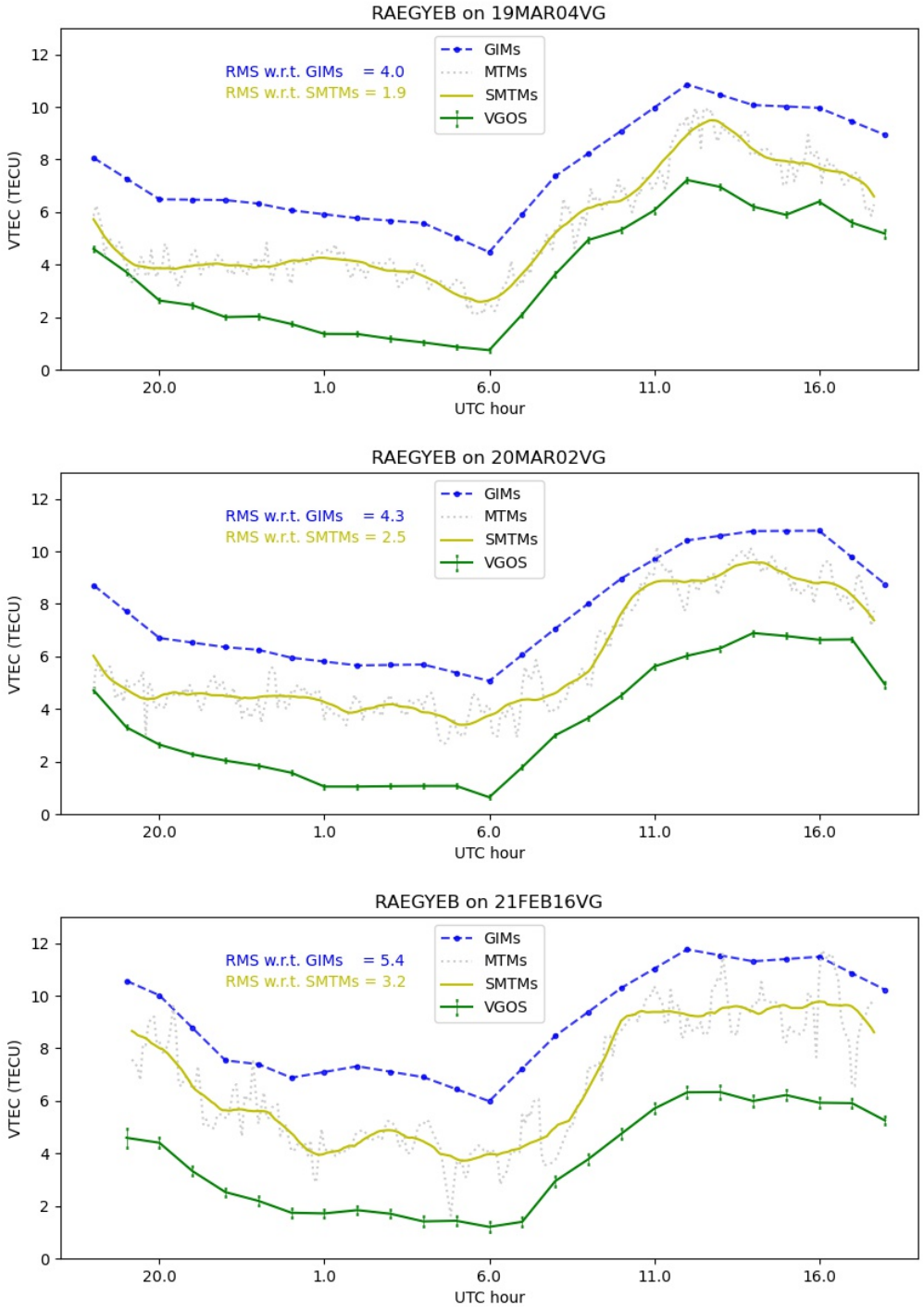

Figure 5.8: VTEC time series of RAEGYEB from session 19MAR04VG (top), 20MAR02VG (middle), and 21FEB16VG (bottom)

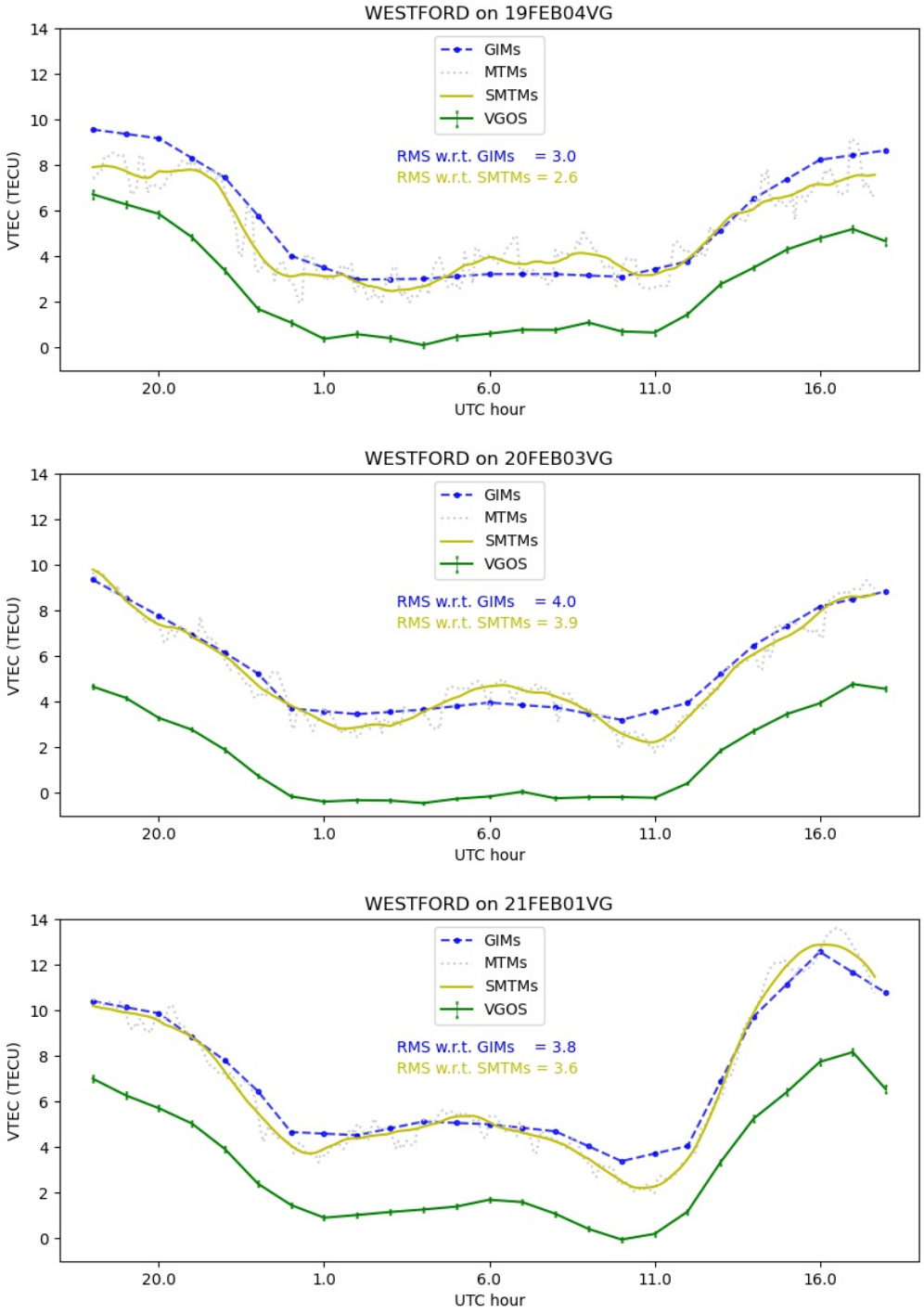

Figure 5.9: VTEC time series of WESTFORD from session 19FEB04VG (top), 20FEB03VG (middle), and 21FEB01VG (bottom)

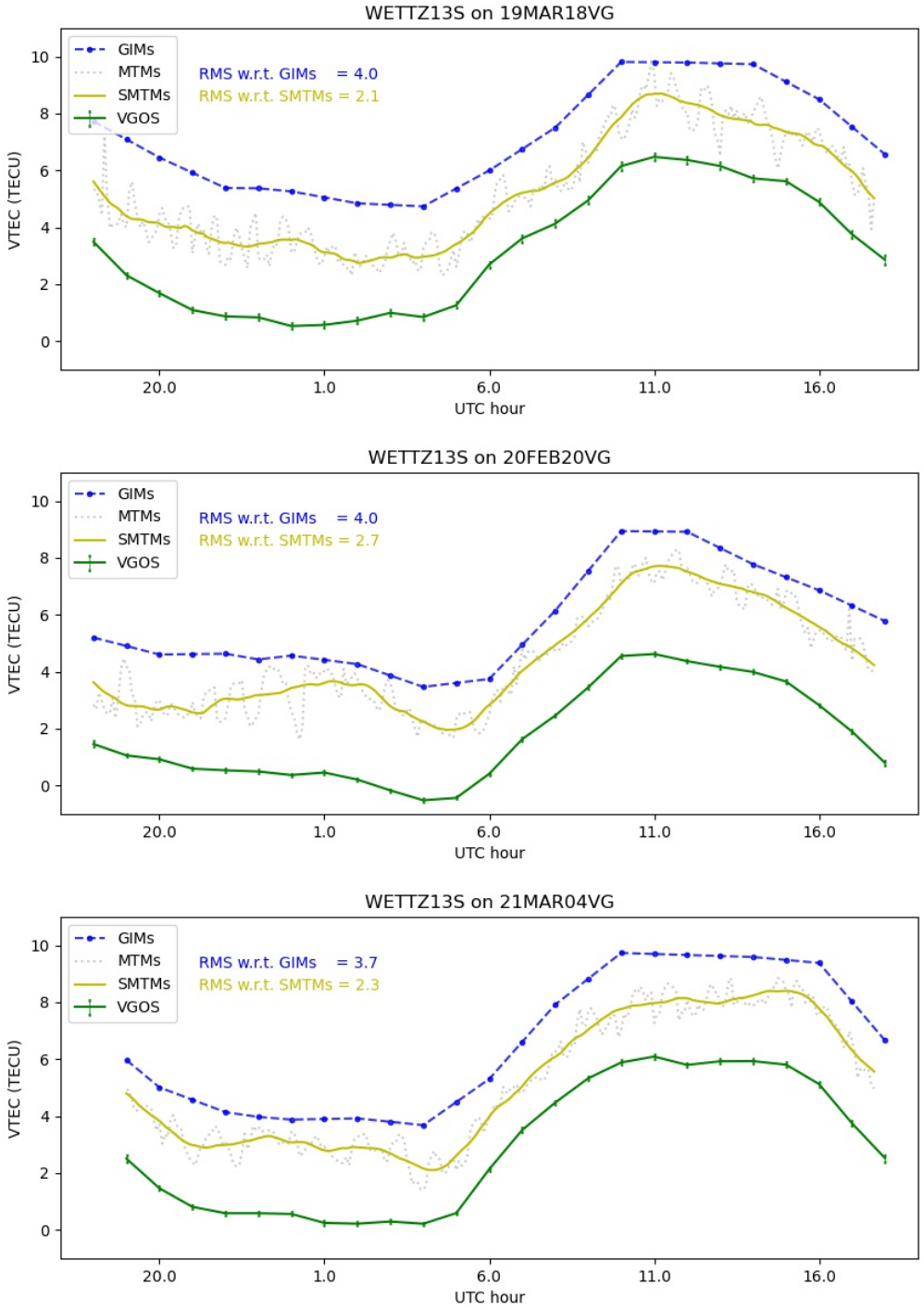

Figure 5.10: VTEC time series of WETTZ13S from session 19MAR18VG (top), 20FEB20VG (middle), and 21MAR04VG (bottom)

5.3 VGOS-GNSS Inter-Technique VTEC Biases

This section is dedicated to the biases in the VGOS-derived VTECs for all available 24-hour VGOS sessions w.r.t. to the station-based VTECs extracted from GIMs and MTMs. First, Fig. 5.11 shows the biases of GGAO12M, ISHIOKA, and KOKEE12M. Then, Fig. 5.12 shows the biases of MACGO12M, ONSA13NE, and ONSA13SW. Finally, Fig. 5.13 shows the biases of RAEGYEB, WESTFORD, and WETTZ13S.

For each station, the biases w.r.t. GIMs and MTMs are displayed as bars in purple and yellow, respectively. The x-axis shows the dates of the sessions while the y-axis shows the RMS in TECU. For some stations, the RMS differences for some sessions w.r.t. GIMs and/or SMTMs exceeds the limits of the y-axis, i.e., 10 TECU. Thus, the exact RMS values of these sessions w.r.t. GIMs and SMTMs are shown along the bar in purple and yellow, respectively. In each figure, the horizontal purple line represents the median RMS differences of VGOS-derived VTEC w.r.t. GIMs-based VTEC, and the yellow line represents the median RMS differences of VGOS-derived VTEC w.r.t. SMTMs-based VTEC. These median RMS differences as well as the number of sessions that VGOS stations participated in so far are summarized in Table 5.1 below.

VGOS Station	no. of sessions	Median RMS w.r.t. GIMs	Median RMS w.r.t. SMTMs
GGAO12M	42	5.08 ± 0.93	3.30 ± 1.01
ISHIOKA	16	4.62 ± 0.24	1.63 ± 0.24
KOKEE12M	42	5.44 ± 1.10	2.04 ± 0.50
MACGO12M	13	5.33 ± 0.39	2.68 ± 0.51
ONSA13NE	40	2.66 ± 0.51	2.24 ± 0.59
ONSA13SW	27	2.63 ± 0.54	2.39 ± 0.61
RAEGYEB	27	3.97 ± 0.79	2.27 ± 0.46
WESTFORD	39	3.16 ± 0.42	2.98 ± 0.60
WETTZ13S	44	4.03 ± 0.43	2.44 ± 0.46

Table 5.1: The median RMS differences of VGOS-derived VTEC w.r.t. to GIMs-based and SMTMs-based VTEC in TECU.

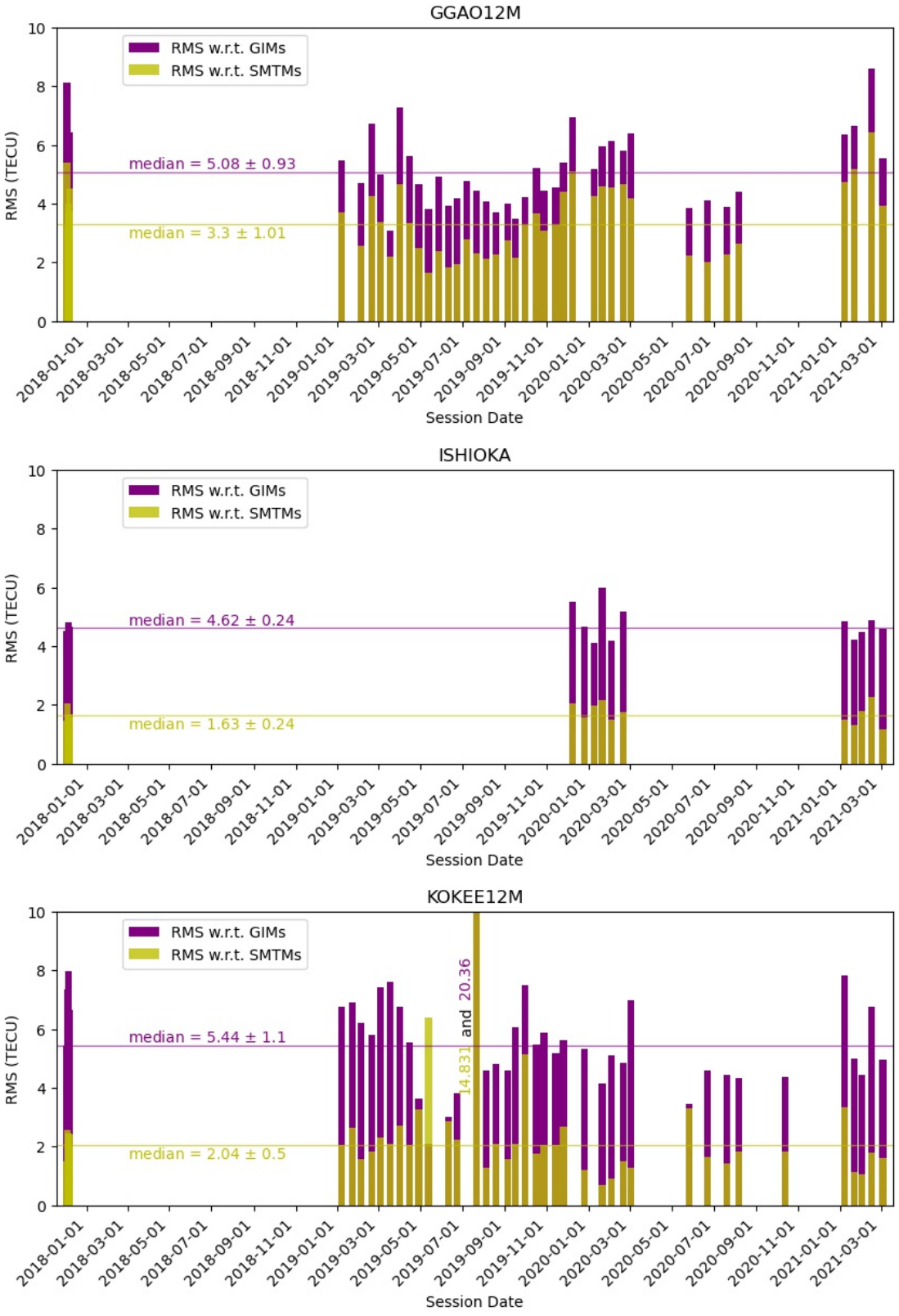

Figure 5.11: VGOS-GNSS inter-technique VTEC biases at GGAO12M (top), ISHIOKA (middle), and KOKEE12M (bottom) derived based on all avaialble 24-hour VGOS sessions.

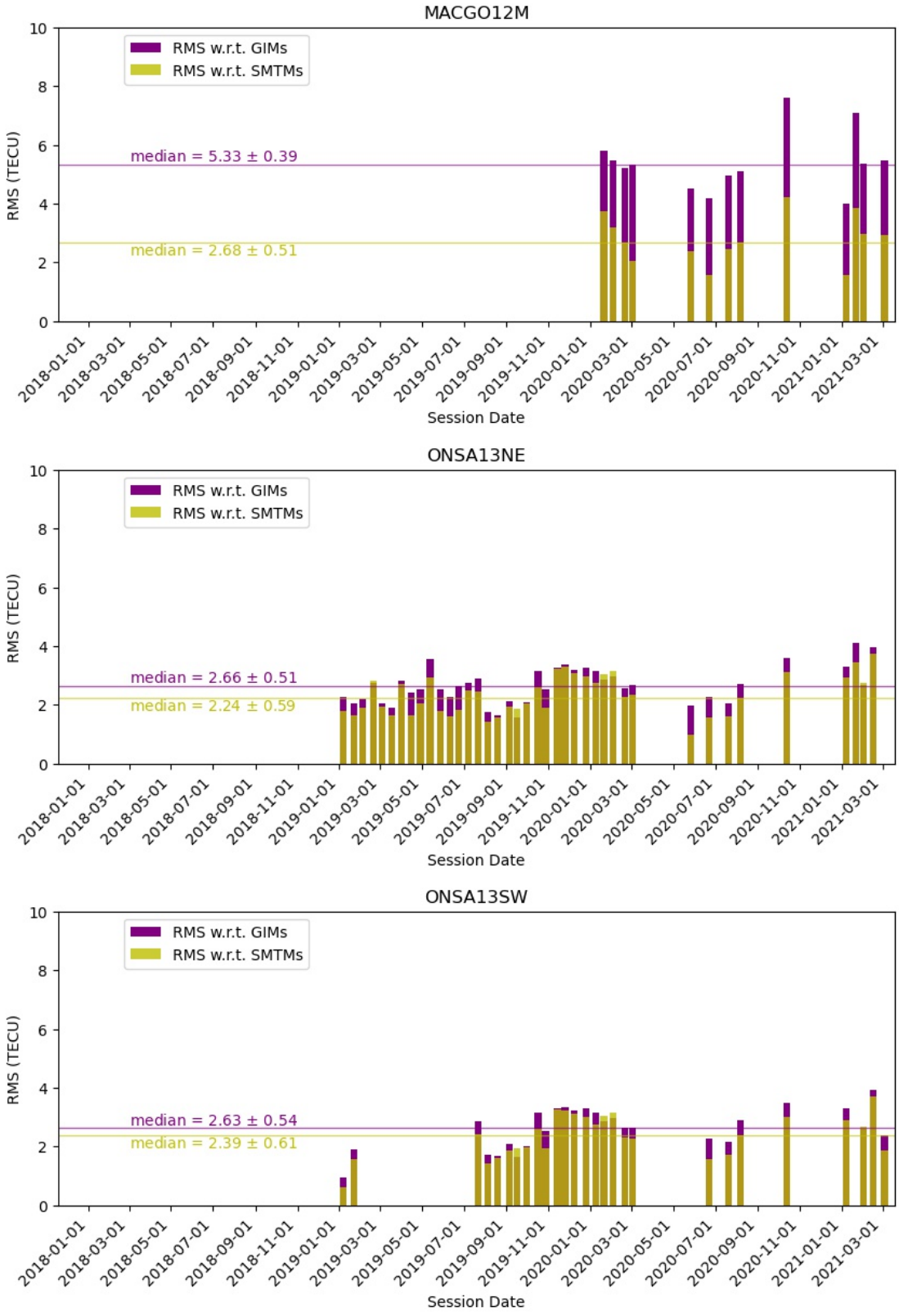

Figure 5.12: VGOS-GNSS inter-technique VTEC biases at MACGO12M (top), ONSA13NE (middle), and ONSA13SW (bottom) derived based on all avaialble 24-hour VGOS sessions.

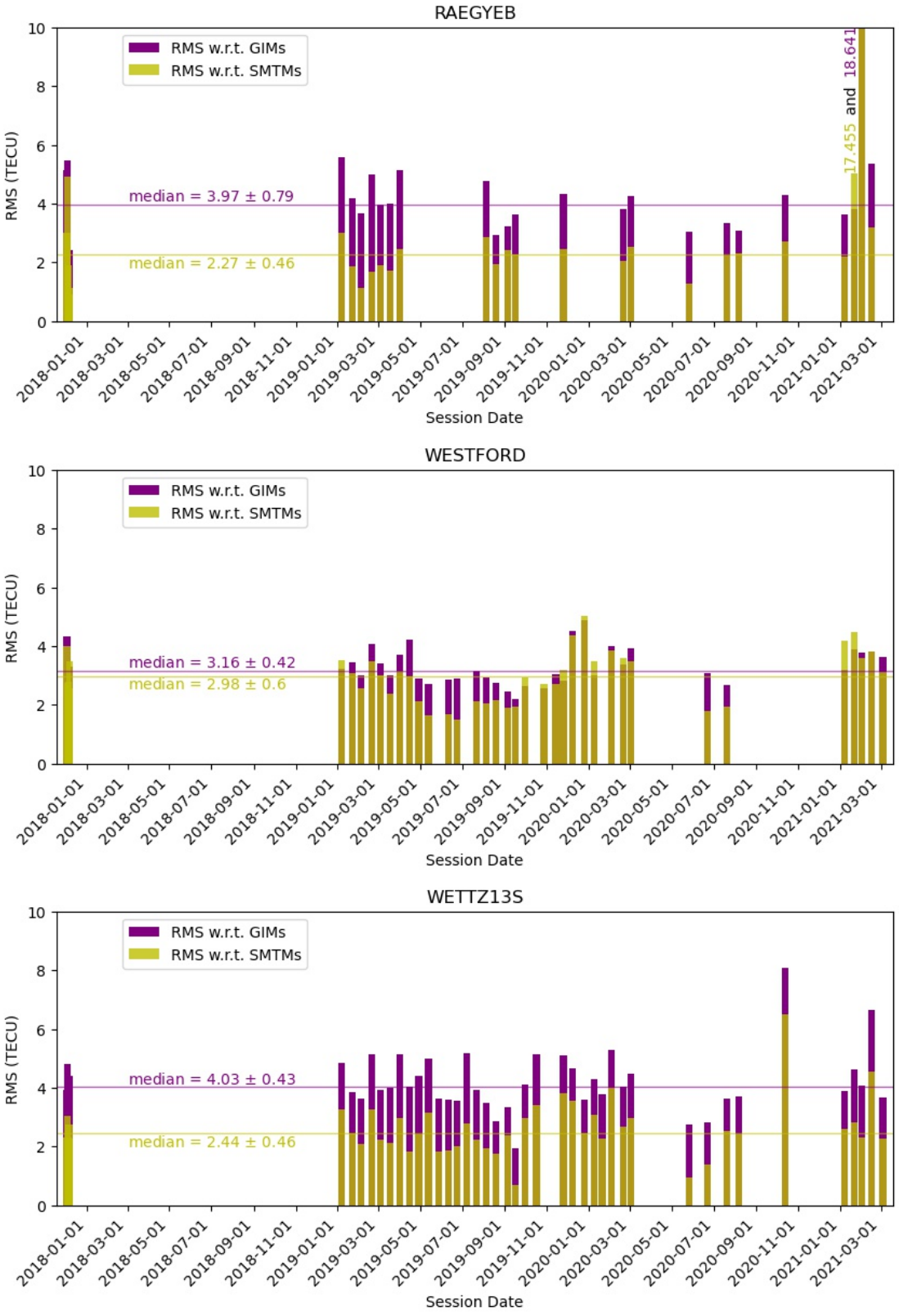

Figure 5.13: VGOS-GNSS inter-technique VTEC biases at RAEGYEB (top), WESTFORD (middle), and WETTZ13S (bottom) derived based on all avaialble 24-hour VGOS sessions.

5.4 VGOS-derived Ionospheric Gradients

This section focuses on the ionospheric gradients in the north and south directions estimated for all available 24-hour VGOS sessions. First, Fig. 5.14 shows the gradients for GGAO12M, ISHIOKA, and KOKEE12M. Then, Fig. 5.15 shows the gradients for MACGO12M, ONSA13NE, and ONSA13SW. Finally, Fig. 5.16 shows the gradients for RAEGYEB, WESTFORD, and WETTZ13S.

For each station, the estimated north and south gradients are visualized as bars in purple and yellow, respectively. The x-axis represents the dates of the sessions while the y-axis represents the gradient, which is in TECU/rad. For some stations, the gradient exceed the y-axis limits, and therefore its exact value is written in black on the corresponding bar.

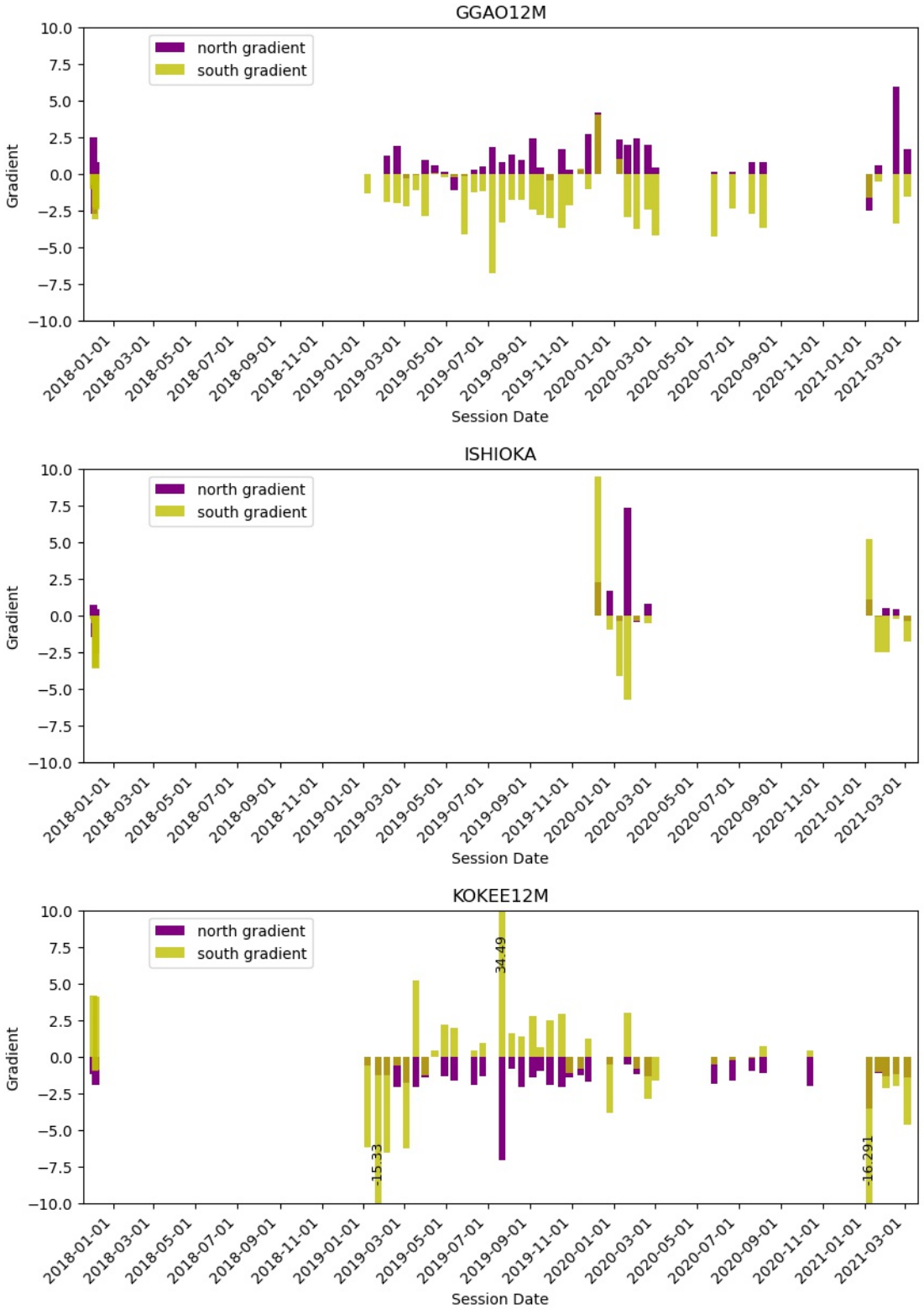

Figure 5.14: The north and south gradients for GGAO12M (top), ISHIOKA (middle), and KOKEE12M (bottom) derived based on all available 24-hour VGOS sessions.

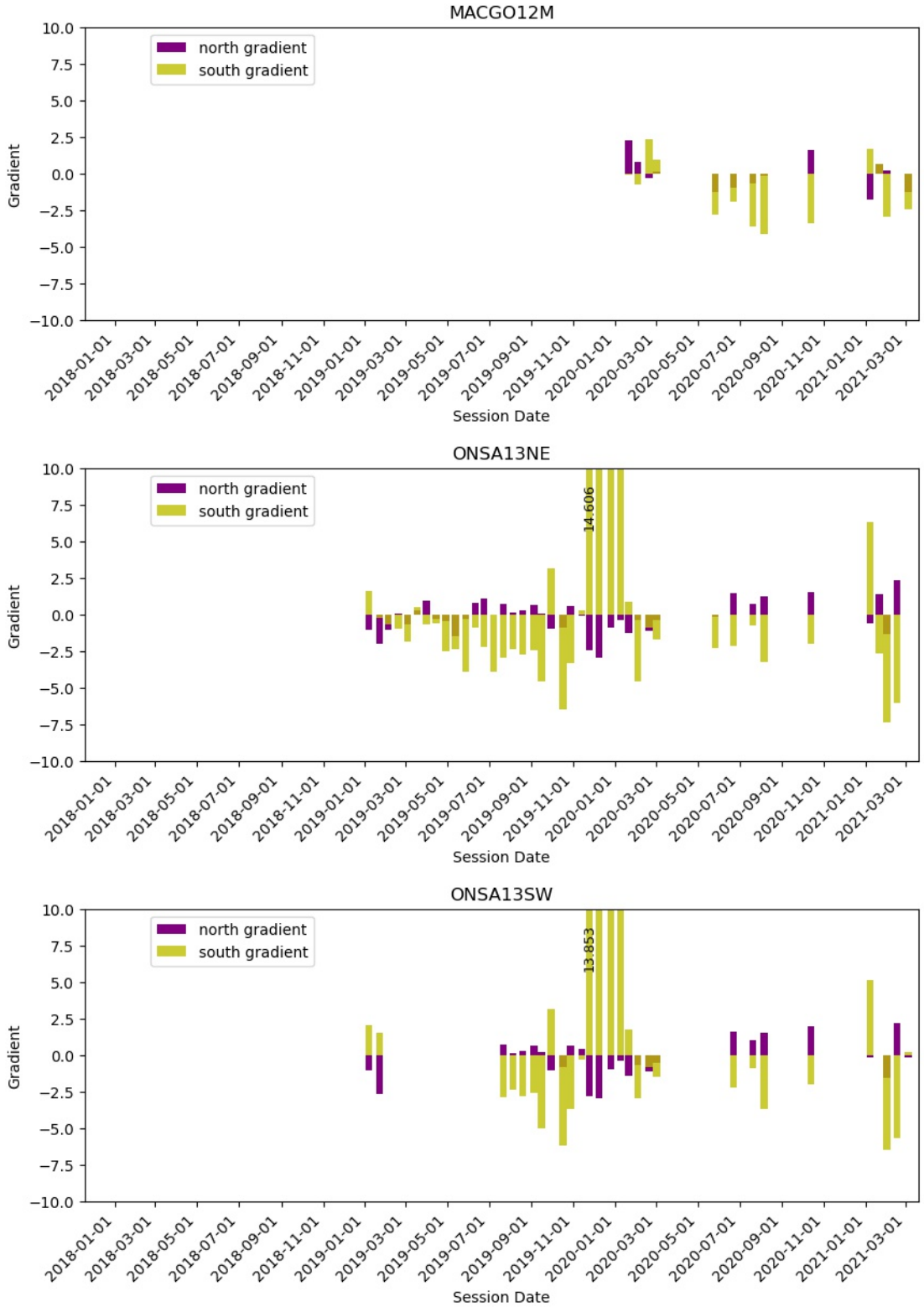

Figure 5.15: The north and south gradients for MACGO12M (top), ONSA13NE (middle), and ONSA13SW (bottom) derived based on all available 24-hour VGOS sessions.

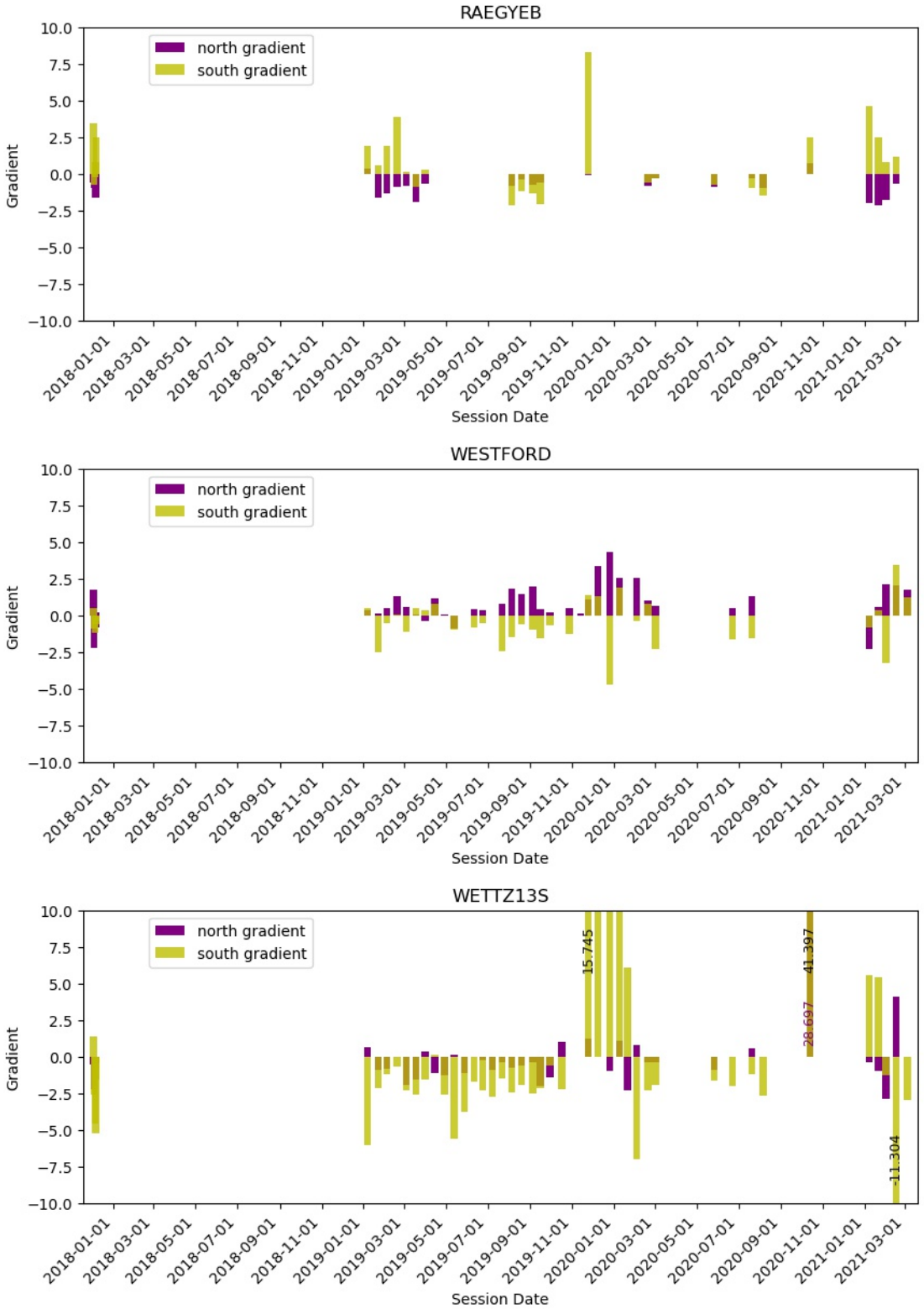

Figure 5.16: The north and south gradients for RAEGYEB (top), WESTFORD (middle), and WETTZ13S (bottom) derived based on all available 24-hour VGOS sessions.

5.5 VGOS Instrumental Offsets

In order to show the impact of the technical difficulties, experienced at some VGOS stations, on the estimated VTEC time series, this section shortly presents the VTEC time series of RAEGYEB, KOKEE12M, ONSA13NE, and ONSA13SW from sessions 17DEC04VG, 19JUL22VG, and 19JAN22VG, respectively. The VTEC time series of all these VGOS stations are shown in green, and this is illustrated on Fig. 5.17, 5.18, 5.19, and 5.20. Moreover, the VTEC time series extracted from GIMs and MTMs are displayed in blue and grey. Since the time series of MTMs are noisy, they were smoothed using the Savitzky–Golay filter, and the smoothed MTMs (SMTMs) are visualised in yellow. The x-axis shows the UTC time while the y-axis shows the VTECs in TECU. The small bars on the VTEC time series of the stations represent the uncertainty of the VTECs.

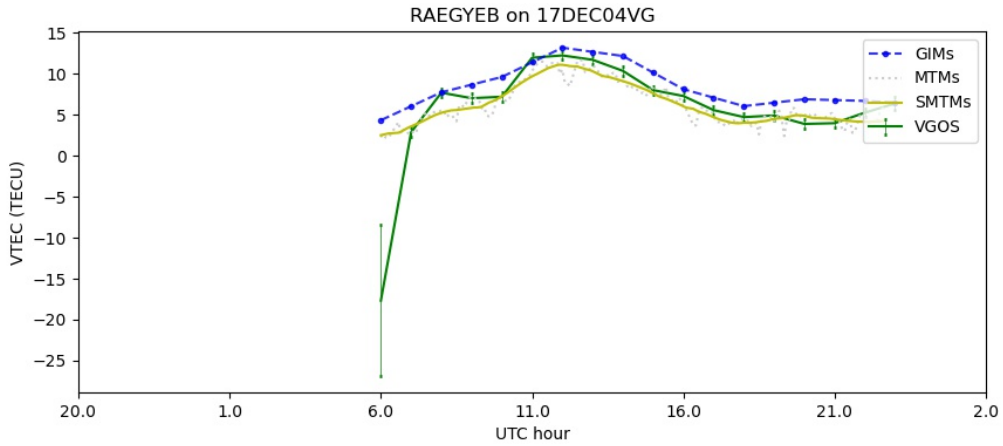

Figure 5.17: The VTEC time series of RAEGYEB from session 19DEC04VG

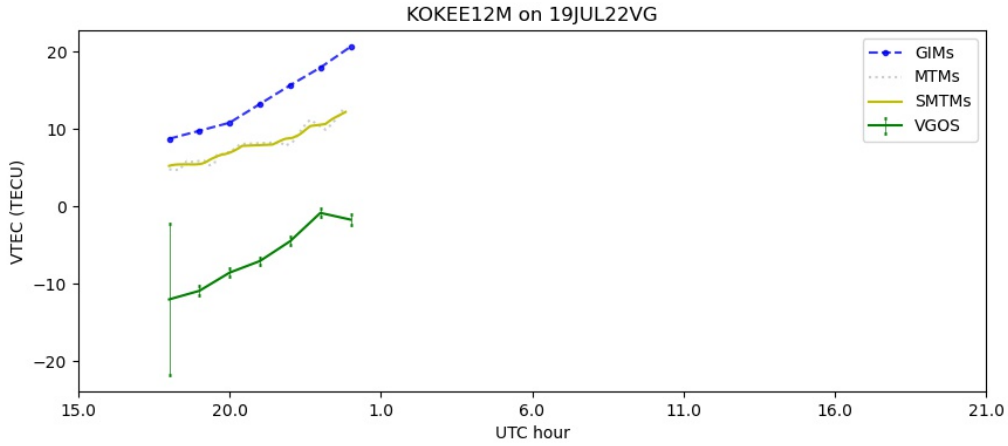

Figure 5.18: The VTEC time series of KOKEE12M from session 19Jul22VG

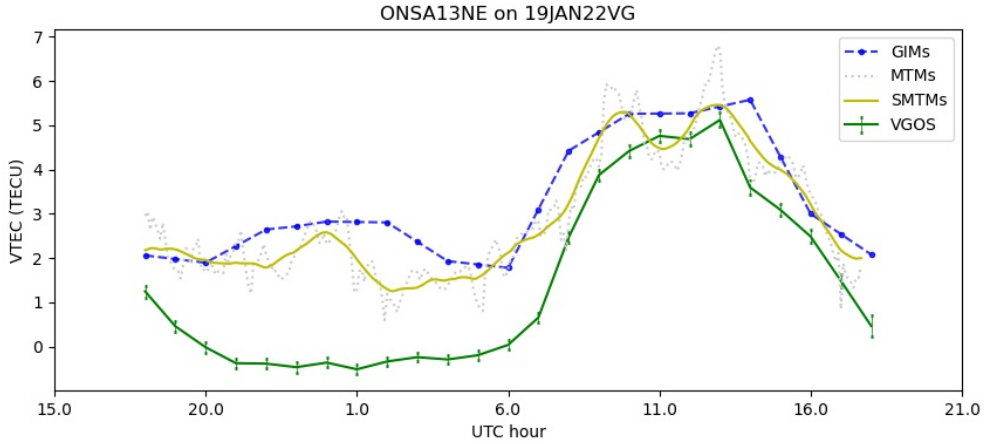

Figure 5.19: The VTEC time series of ONSA13NE from session 19JAN22VG

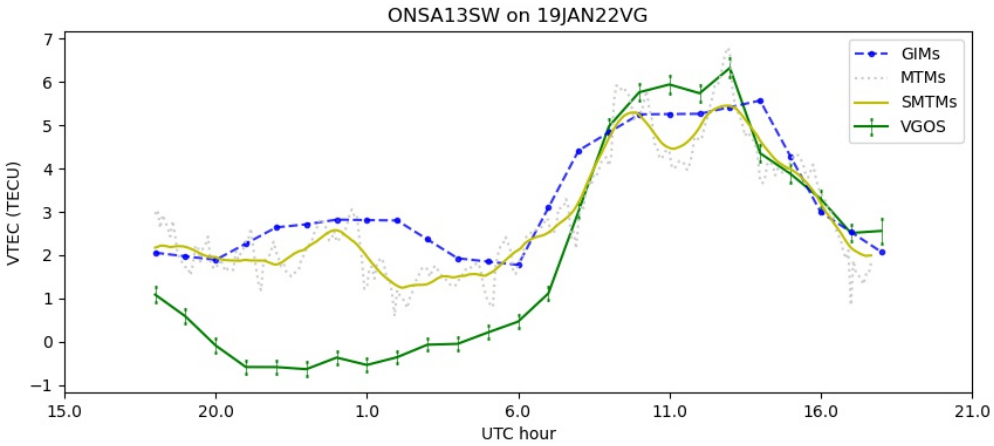

Figure 5.20: The VTEC time series of ONSA13SW from session 19JAN22VG

This section also summarizes the instrumental offsets derived for all nine VGOS stations and for all available 24-hour VGOS sessions. First, Fig. 5.21 shows the instrumental offsets for GGAO12M, ISHIOKA, and KOKEE12M. Then, Fig. 5.22 shows the instrumental offsets for MACGO12M, ONSA13NE, and ONSA13SW. Finally, Fig. 5.23 shows the instrumental offsets for RAEGYEB, WESTFORD, and WETTZ13S.

For each station, the estimated instrumental offsets are visualised as purple bars. In each figure, the small black line at the tip of each bar, i.e., the so-called error bar, represents the uncertainty of the instrumental offsets. Further, the x-axis show the dates of the sessions while the y-axis show the instrumental offsets in TECU. For some sessions, the instrumental offsets exceed the limits of y-axis. Therefore, the exact values of these instrumental offsets are given along the corresponding bars.

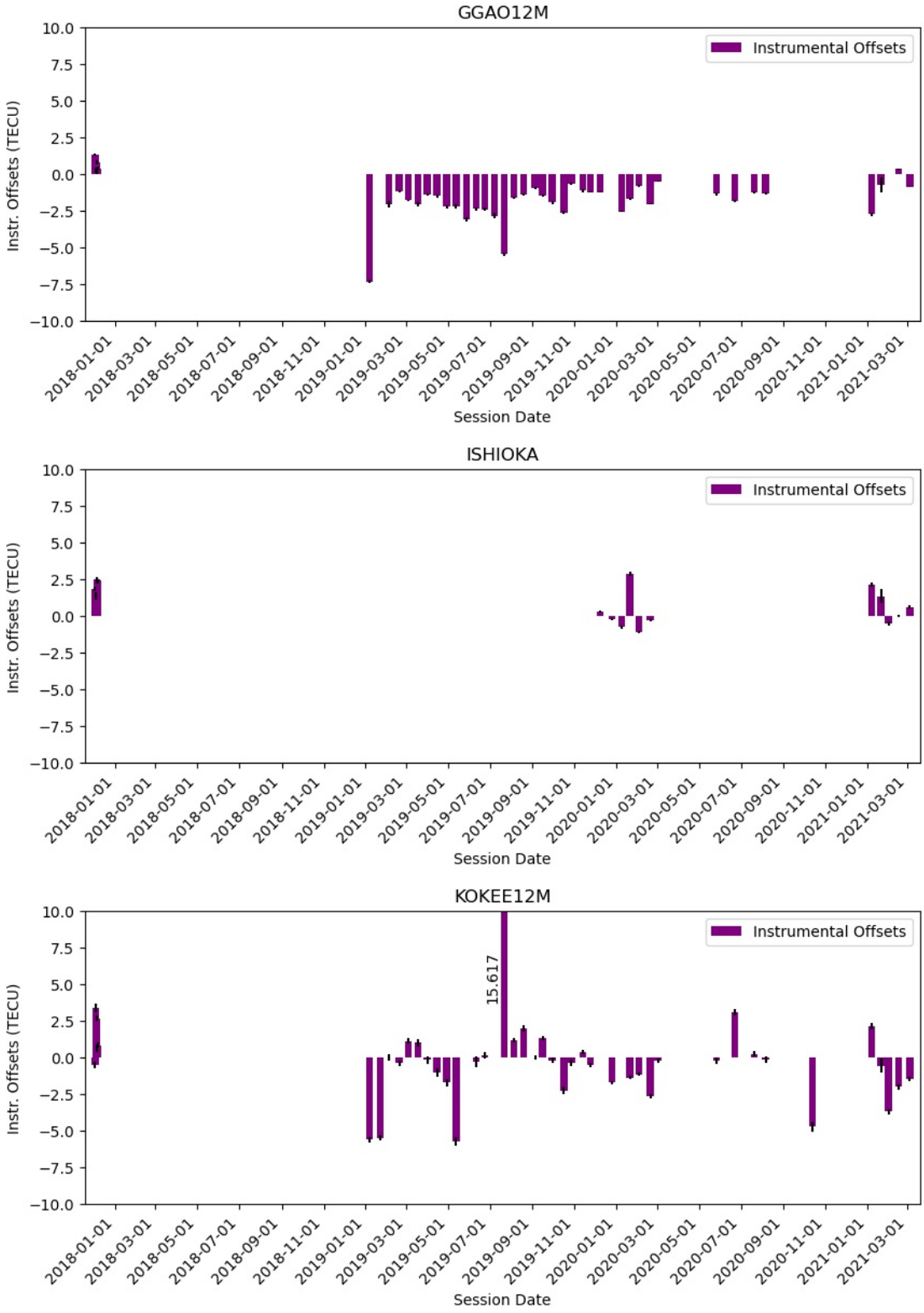

Figure 5.21: The estimated instrumental offsets for GGAO12M (top), ISHIOKA (middle), and KOKEE12M (bottom) displayed for all available 24-hour VGOS sessions.

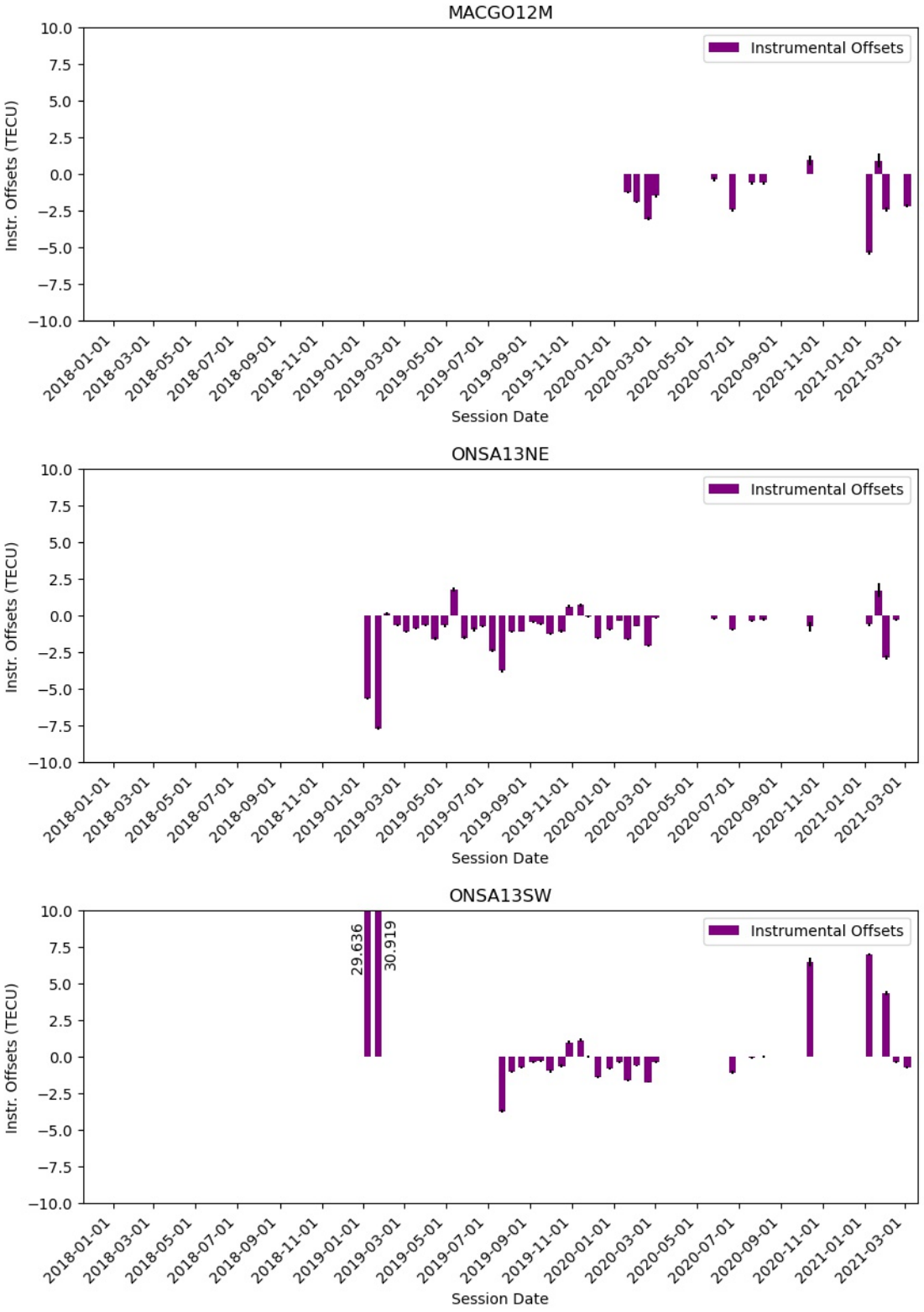

Figure 5.22: The estimated instrumental offsets for MACGO12M (top), ONSA13NE (middle), and ONSA13SW (bottom) displayed for all available 24-hour VGOS sessions.

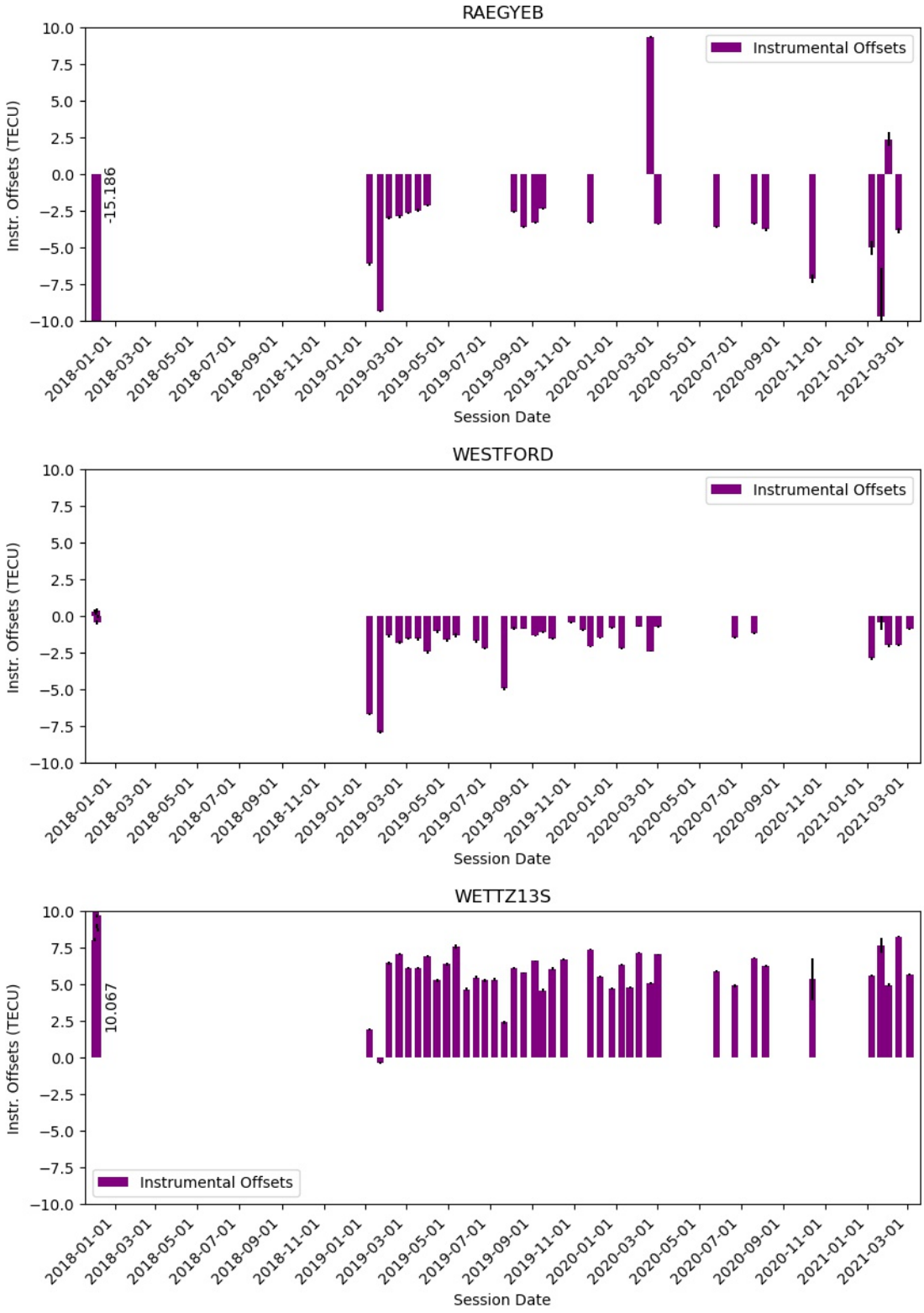

Figure 5.23: The estimated instrumental offsets for RAEGYEB (top), WESTFORD (middle), and WETTZ13S (bottom) displayed for all available 24-hour VGOS sessions.

5.6 Uncertainty of VGOS-derived VTEC

This section summarizes the uncertainties of the VTEC estimates for all the available sessions. VGOS stations that experienced technical difficulties were excluded from the solution. Furthermore, no relative constraints between the PWL offsets were applied. The reason behind is to reflect the true accuracy of VTEC estimates.

The RMS values of the station-based VTEC uncertainties are displayed as purple bars in Fig. 5.24, 5.25, and 5.26. The x-axis shows the dates of the sessions while the y-axis shows the uncertainty RMS of the sessions in TECU. The horizontal line on each plot represents the median uncertainty of the VTEC estimates for the corresponding station. These median uncertainty as well as the number of sessions considered when calculating these uncertainty are summarized in Table 5.2.

VGOS Station	no. of sessions	Median Uncertainty
GGAO12M	42	0.09 ± 0.02
ISHIOKA	15	0.12 ± 0.02
KOKEE12M	41	0.22 ± 0.05
MACGO12M	13	0.10 ± 0.01
ONSA13NE	40	0.09 ± 0.01
ONSA13SW	25	0.08 ± 0.01
RAEGYEB	21	0.10 ± 0.02
WESTFORD	39	0.08 ± 0.01
WETTZ13S	43	0.10 ± 0.02

Table 5.2: The median uncertainty of VGOS-derived VTEC in TECU for all nine VGOS stations.

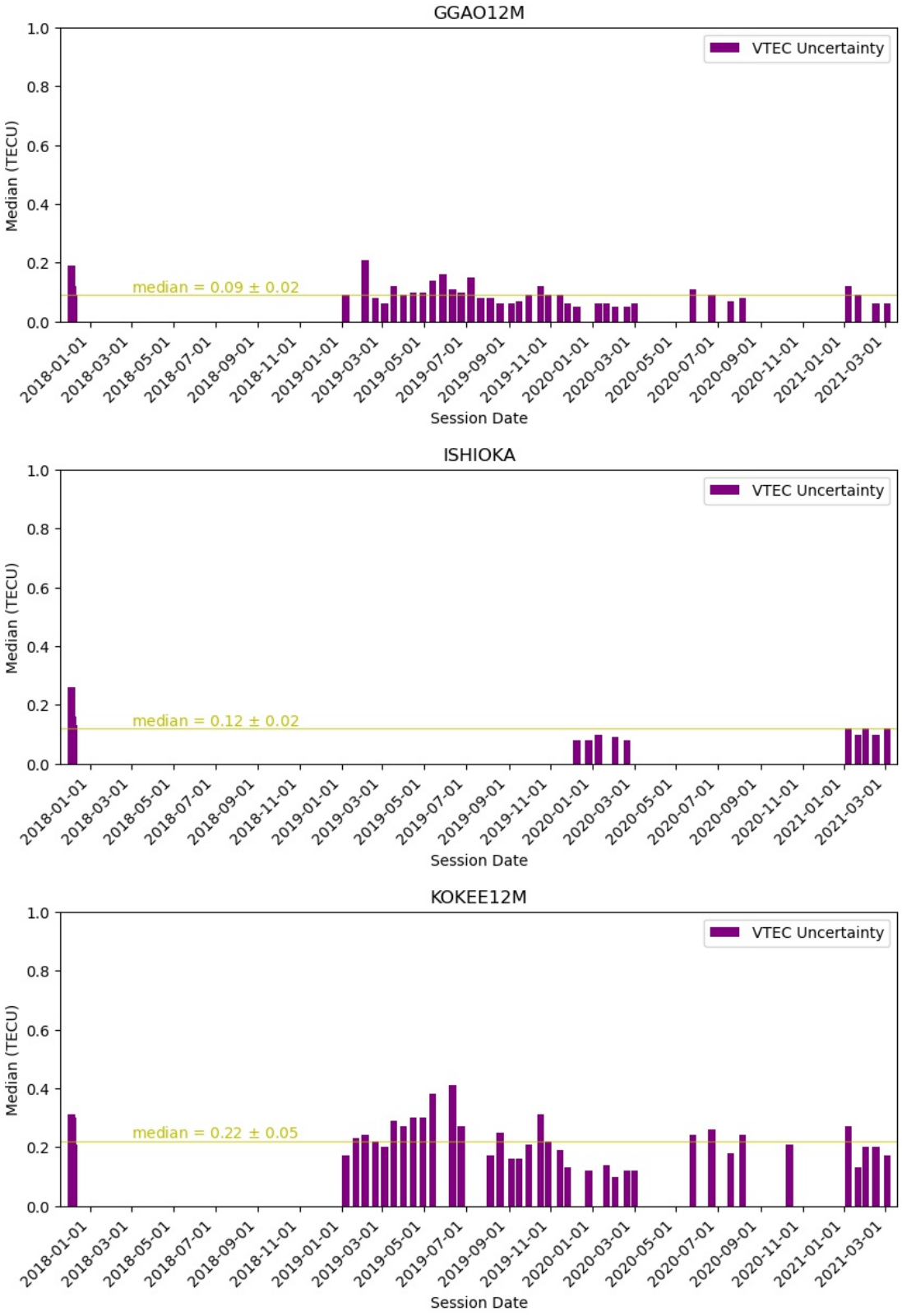

Figure 5.24: The estimated uncertainties of VTECs for GGAO12M (top), ISHIOKA (middle), and KOKEE12M (bottom)

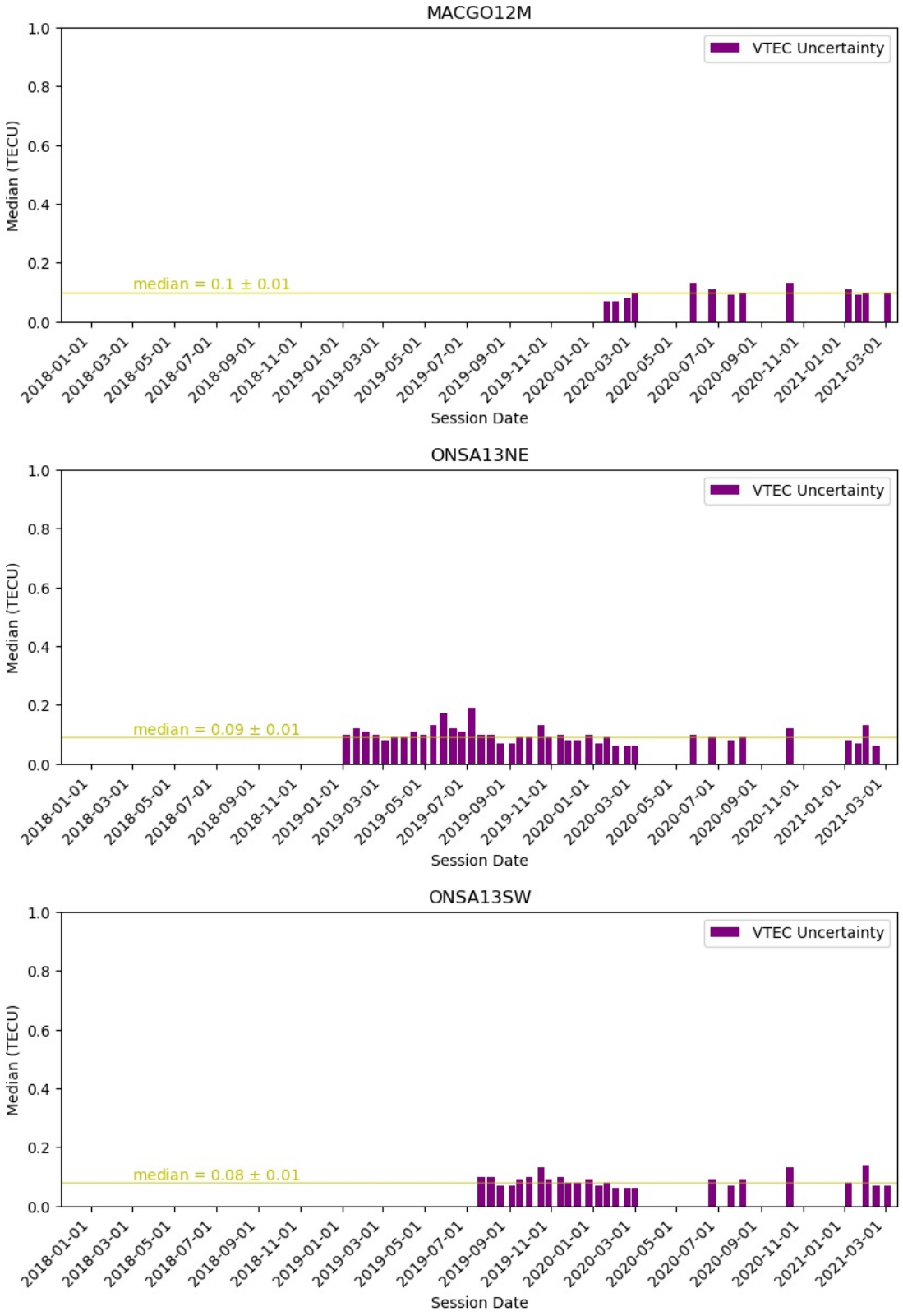

Figure 5.25: The estimated uncertainties of VTECs for MACGO12M (top), ONSA13NE (middle), and ONSA13SW (bottom)

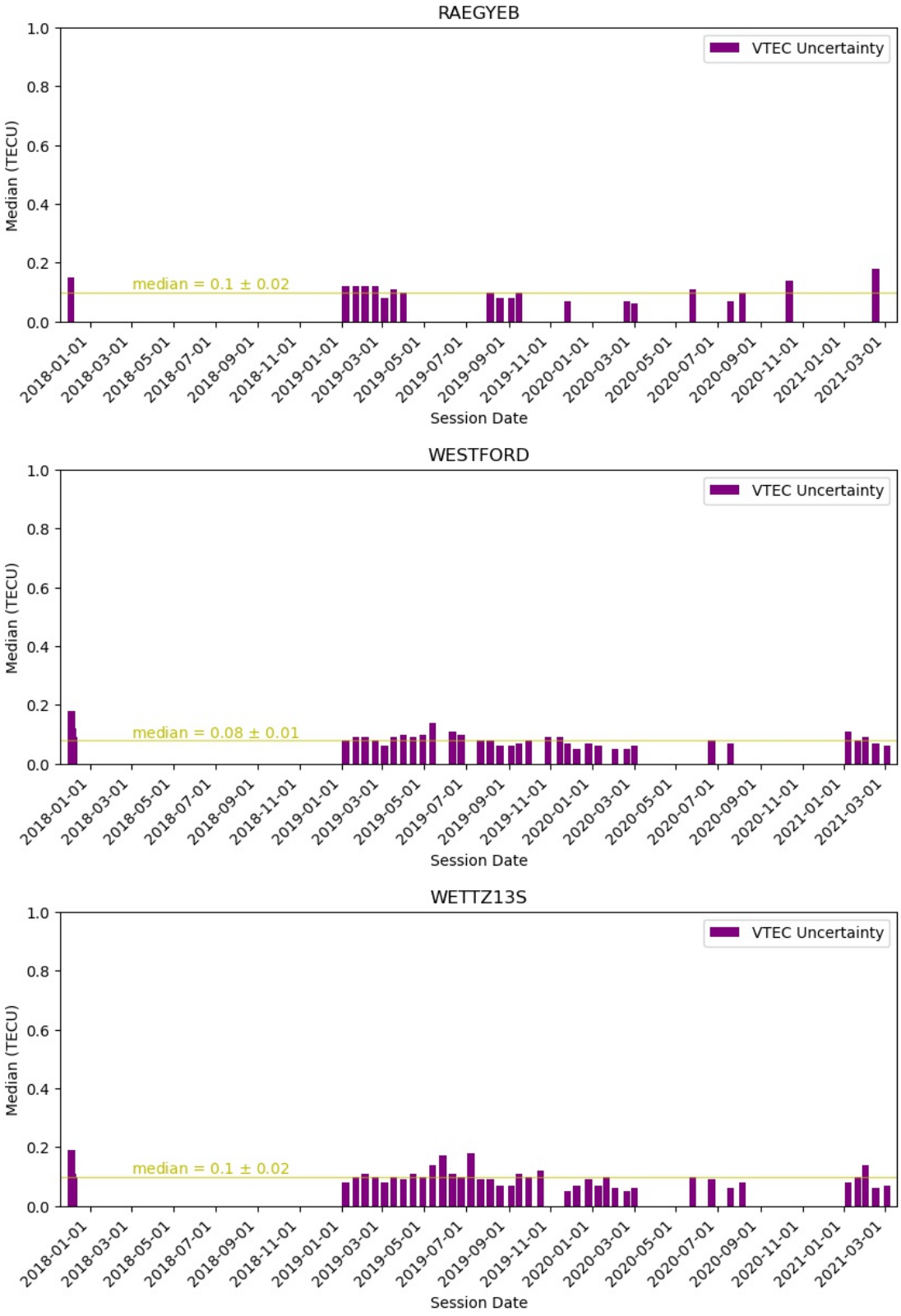

Figure 5.26: The estimated uncertainties of VTECs for RAEGYEB (top), WESTFORD (middle), and WETTZ13S (bottom)

6 Discussion

6.1 Validation of VGOS-derived VTEC Time series

Few VGOS sites such as those located at Kokee Observatory and Wettzell Observatory are already equipped with geodetic VBLI telescopes and GNSS antennae. The VTECs derived from observations carried out with these instruments could be used to validate the VTECs derived from observations made with VGOS. This requires an overlap in the time window of the observation between the different techniques. Fortunately, VGOS session 19APR29VG had an overlap of 22 hours with the geodetic VLBI session 19APR29XA and 19APR29XB. The subsequent paragraphs focus on the comparison between the VTECs derived from VGOS and GNSS observations at Kokee and Wettzell.

First, Fig. 5.1 shows the VTEC time series derived for VGOS station KOKEE12M, geodetic VLBI station KOKEE, and GNSS station KOKV, all of which are located in Hawaii, USA. The figure also shows the corresponding VTEC time series extracted from GIMs and SMTMs in blue and grey, respectively. As expected, the VTEC time series of KOKEE12M show similar temporal behavior of the ionosphere to that for KOKEE and KOKV for this time window. This is also the case for the VTEC time series from GIMs and SMTMs. There is however a bias between the VTEC time series of KOKEE12M and the remaining VTEC time series. The smallest VTEC bias was found to be in relation to KOKEE, i.e., 1.8 TECU, while the largest VTEC bias occurs w.r.t. GIMs, i.e., 3.6 TECU. The VTEC bias w.r.t. SMTMs and KOKV is 3.3 TECU for both.

Moreover, Fig. 5.2 shows the VTEC time series of VGOS station WETTZ13S, geodetic VLBI station WETTZ13N and WETTZELL, and GNSS station WTZZ, all of which are present at Geodetic Observatory Wettzell. As anticipated, the VTECs time series of WETTZ13S shows similar temporal behavior as in the case of WETTZ13S, WETTZ13N, WETTZELL, and WTZZ. Similarly to KOKEE12M, the VTEC time series of WETTZ13S exhibits a bias w.r.t. to the remaining time series. The smallest VTEC bias occurs w.r.t. WETTZELL, i.e., 1.5 TECU while the largest VTEC bias is w.r.t. GIMs, i.e., 4.4 TECU. Furthermore, the VTEC bias w.r.t. SMTMs, WTZZ, and WETTZ13N is 2.4, 3.9, and 4.0 TECU, respectively. In addition, the VTEC bias between WETTZ13N and WETTZELL, both of which belong to the legacy VLBI network, is 5.3 TECU.

6.2 VGOS Session-to-Session Comparison

GGAO12M is located at Goddard Geophysical and Astronomical Observatory in Maryland, USA. The VTEC time series of GGAO12M for session 19DEC09VG, 20JUL20VG, and 21MAR04VG,

are depicted in the top, middle and bottom of Fig. 5.3, respectively. The figure illustrates that the VTEC time series of GGAO12M vary in shape, which is expected, see Sec. 2.1, reflecting the ionosphere state above GGAO12M. For the the three highlighted sessions, the VTEC time series of GGAO12M is in general smooth and demonstrates similar temporal behavior comparable to VTEC time series from GIMs and SMTMs. The VTEC bias for GGAO12M w.r.t. GIMs and SMTMs varies from session to session. For example, the calculated RMS values of VTEC for GGAO12M w.r.t. GIMs are 6.9, 3.9 and 5.5 TECU for sessions 19DEC09VG, 20JUL20VG, and 21MAR04VG, respectively. The calculated RMS values of VTEC for GGAO12M w.r.t. SMTMs are 5.1, 2.3 and 3.9 TECU for session 19DEC09VG, 20JUL20VG, and 21MAR04VG, respectively. In addition, the VTEC time series of GGAO12M for session 19DEC09VG has some negative values, which seems to be contradictory to the physical nature of the ionosphere. This phenomena would probably vanish when the VTEC bias stemming from VGOS instrumentation is removed.

ISHIOKA is located at Ibaraki Prefectural Livestock Research Center in Ishioka, Japan. The VTEC time series of ISHIOKA for sessions 19DEC26VG, 20FEB20VG, and 21MAR04VG are shown in Fig. 5.4. As anticipated, these time series show similar temporal behavior compared to the VTEC from GIMs and SMTMs. Unlike GGAO12M, the calculated VTEC bias for ISHIOKA w.r.t. GIMs and SMTMs slightly varies from session to session. For the three sessions presented in Fig. 5.4, the RMS w.r.t. GIMs and SMTMs are approx. 5 and 1 TECU.

KOKEE12M is located at Kokee Park Geophysical Observatory in Hawaii, USA. The VTEC time series of KOKEE12M for session 19FEB04VG, 20FEB20VG, and 21MAR04VG are presented in 5.5. For all three sessions, the VTEC time series of KOKEE12M show similar temporal behavior compared to the VTEC time series from SMTMs, and the VTEC bias concerning KOKEE12M w.r.t. SMTMs is almost constant, i.e., 1.5 TECU. For session 19FEB04VG, the VTEC time series from GIMs for KOKEE12M shows a significant difference of 12 TECU around mid-night when compared to the time series of KOKEE12M and SMTMs. The main contributor to this difference could probably be the background model used in GIMs, which is used to smooth the ionospheric gradient and is known to introduce errors (Johnston et al., 2017). A second contributing factor could be in this case the magnetic field around the modip equator, the so-called equatorial plasma bubbles, see Sec. 2.1, which results in sharp ionospheric gradients (Johnston et al., 2017). In general, the mean RMS differences of VGOS-derived VTEC w.r.t. GIMs-based VTEC is between 5 and 6 TECU for these sessions.

MACGO12M is located at the University of Texas McDonald Observatory in Texas, USA. The VTEC time series of MACGO12M for session 20FEB03VG, 20JUL20VG, and 21FEB01VG are presented in 5.6. For all the three sessions, the VTEC time series of MACGO12M shows similar behavior of ionosphere when compared to the VTEC time series from GIMs and SMTMs. The VTEC bias w.r.t. GIMs and SMTMs is almost constant across these three sessions, and the

RMS differences of VGOS-derived VTEC values w.r.t GIMs-based and SMTMs-based VTEC are 5 and 3 TECU, respectively.
ONSA13NE and ONSA13SW are twin telescopes, located at Onsala Space Observatory in Sweden. The VTEC time series of ONSA13NE and ONSA13SW for session 19SEP30VG, 20FEB03VG, and 21FEB01VG are shown in Fig. 5.7 in green and brown, respectively. The VTEC time series for both stations not only show similar temporal behaviour when compared to the VTEC time series from GIMs and SMTMs, but also almost coincide with each other during the whole 24-hour session and across the different sessions. This good agreement between the VTEC time series from ONSA13NE and ONSA13SW can be utilized to reflect the current precision of VGOS-derived VTECs, see Sec. 5.6. In general, the mean VTEC bias for the two stations w.r.t. GIMs and SMTMs is 2.5 TECU.
RAEGYEB is located at Yebes Observatory in Portugal. The VTEC time series of RAEGYEB for session 19MAR04VG, 20MAR02VG, and 21FEB16VG are illustrated in Fig. 5.8. For the three highlighted sessions, the VTEC time series for RAEGYEB show similar temporal behaviour comparable to the VTEC time series from GIMs and SMTMs. The VTEC bias for RAEGYEB w.r.t. GIMs and SMTMs slightly varies from session to session. The RMS differences of VGOS-derived VTEC values w.r.t GIMs-based are between 4 and 5 TECU while the RMS differences of VGOS-derived VTEC values w.r.t SMTMs-based VTEC are between 2 and 3 TECU.
WESTFORD is located at MIT Haystack Observatory in Massachusetts, USA. The VTEC time series of WESTFORD for sessions 19FEB04VG, 20FEB03VG, and 21FEB01VG are presented in Fig. 5.9. The VTEC time series for WESTFORD shows similar temporal behavior of ionosphere to that for the VTEC time series from GIMs and SMTMs. The calculated VTEC biases w.r.t. GIMs and SMTMs is almost identical to each other, and they vary between 3 and 4 TECU.
WETTZ13S is located at Geodetic Observatory Wettzell in Germany. The VTEC time series for WETTZ13S for session 19MAR18VG, 20FEB20VG, and 21MAR04VG are depicted in Fig. 5.10. The VTEC time series of WETTZ13S show similar temporal behavior when compared to the VTEC time series from GIMs and SMTMs. The calculated VTEC bias for WETTZ13S w.r.t. GIMs and SMTMs is almost constant across the investigated sessions, i.e., 4 and 2.5 TECU, respectively.

6.3 VGOS-GNSS Inter-technique VTEC biases

The session-to-session comparison in Sec. 6.2 reveals the VTEC biases of VGOS-derived VTEC w.r.t. GIMs-based and SMTMs-based vary in size for all VGOS stations. The VTEC biases for all VGOS nine stations were calculated as RMS differences and presented in Fig. 5.11, 5.12,

and 5.13 for all available VGOS 24-hour sessions.

GGAO12M participated in 42 out of 44 sessions since Dec. 2017, see Fig. 5.11. The calculated VTEC bias w.r.t. GIMs and SMTMs vary largely across the investigated sessions. The smallest and largest RMS differences of VGOS-derived VTEC w.r.t. GIMs-based VTEC are 3.52 and 8.58 TECU for sessions 19MAY13VG and 21FEB16VG, respectively. The smallest and largest RMS differences of VGOS-derived VTECs w.r.t. SMTMs-based VTEC are 1.66 and 6.44 TECU for session 19MAY13VG and 21FEB16VG, respectively. The median RMS differences of VGOS-derived VTEC w.r.t. GIMs-based and SMTMs-based VTEC are 5.08 ± 0.93 and 3.3 ± 1.01 TECU, respectively.

ISHIOKA participated in 16 out of 44 sessions so far, see Fig. 5.11. The VTEC bias w.r.t. VTECs from GIMs and SMTMs remained constant across the investigated sessions. The median RMS differences of VGOS-derived VTEC w.r.t. GIMs-based and SMTMs-based VTEC are 4.62 ± 0.24 and 1.63 ± 0.24 TECU, respectively.

KOKEE12M participated in 42 out of 44 sessions so far, see Fig. 5.11. In general, the VTEC bias w.r.t. GIMs and SMTMs varies greatly from session to session. The VTEC bias w.r.t. GIMs and SMTMs however reached 14.83 and 20.36 TECU for session 19JUL22VG. On this session, KOKEE12M started late and experienced technical difficulties, see history file in Fig. C4. The median RMS differences of VGOS-derived VTEC w.r.t. GIMs-based and SMTMs-based VTEC are 5.44 ± 1.1 and 2.04 ± 0.5 TECU, respectively.

MACGO12M participated in 13 out of 44 sessions so far, see Fig. 5.12. Similar to KOKEE12M, the VTEC bias w.r.t. GIMs and SMTMs also varies significantly from session to session. The smallest and largest RMS differences of VGOS-derived VTEC w.r.t. GIMs-based VTEC are 4.0 and 7.6 TECU, respectively, while the smallest and largest RMS differences of VGOS-derived VTECs w.r.t. SMTMs-based VTEC are 1.57 and 4.23 TECU, respectively. The median RMS differences of VGOS-derived VTEC w.r.t. GIMs-based and SMTMs-based VTEC are 5.33 ± 0.39 and 2.68 ± 0.51 TECU, respectively.

ONSA13NE and ONSA13SW participated in 40 and 27 out of 44 sessions so far, respectively, see Fig. 5.12. For ONSA13NE and ONSA13SW, the VTEC bias w.r.t. GIMs was not only almost equal to the VTEC bias w.r.t. SMTMs for most sessions but also nearly stable across the sessions. For ONSA13NE, the median RMS differences of VGOS-derived VTECs w.r.t. GIMs-based and SMTMs-based VTEC are 2.66 ± 0.51 and 2.24 ± 0.59 TECU, respectively. For ONSA13SW, the median RMS differences of VGOS-derived VTECs w.r.t. GIMs-based and SMTMs-based VTEC are 2.63 ± 0.54 and 2.39 ± 0.61 TECU, respectively.

RAEGYEB participated in 27 out of 44 sessions, see Fig. 5.13. Like most other stations, the VTEC bias for RAEGYEB varies from session to session. However, for session 21FEB01VG, the RMS differences of VGOS-derived VTEC w.r.t. GIMs-based and SMTMs-based VTEC reached 18.64 and 17.45 TECU, respectively. During this session, RAEGYEB expierienced

multiple problems such as data lost, high phase-cal amplitude (that corrupts the estimation of broadband delays and dTECs), low fringe amplitude, and phase jumps, see the history file in Fig. C10. As a result, the quality of VTEC estimates for this session are of low quality. In general, the median RMS differences of VGOS-derived VTECs w.r.t. GIMs-based and SMTMs-based VTEC are 3.97 ± 0.79 and 2.27 ± 0.46 TECU, respectively.

WESTFORD participated in 39 out of 44 sessions so far, see Fig. 5.13. The VTEC bias for WESTFORD w.r.t. GIMs and SMTMs varies little across sessions. The median RMS differences of VGOS-derived VTECs w.r.t. GIMs-based and SMTMs-based VTEC are 3.16 ± 0.42 and 2.98 ± 0.6 TECU, respectively.

WETTZ13S participated in all the 44 sessions, see Fig. 5.13. The VTEC bias for WETTZ13S w.r.t. GIMs and SMTMs varies noticeably similar to the VTEC bias for most other stations. However, for session 20OCT13VG, WETTZ13S had numerous non-detections for unknown reasons in particular on long baselines, according to the history file, see Fig. C9. In general, the median RMS differences of VGOS-derived VTECs w.r.t. GIMs-based and SMTMs-based VTEC are 4.03 ± 0.43 and 2.44 ± 0.46 TECU, respectively.

There are many possible factors contributing to these discrepancies between VGOS-derived VTEC, GIMs-based VTEC, and SMTMs-based VTEC. These factors can be categorised into two groups. The first group is the calibration uncertainty of VGOS and GNSS instrumentation, which can manifest themselves not only in the form of noise but also as a VTEC bias. For GNSS, the uncertainty in the differential code biases (DCBs) of GNSS satellite and receivers is a main source of errors in estimating the absolute TEC from GNSS observation (Sekido et al., 2003; Rideout and Coster, 2006; Vierinen et al., 2016). For VGOS, radio source structure effects is a major source of errors in VGOS observations (Xu et al., 2017; Anderson and Xu, 2018; Niell et al., 2018). These structure effects cause jumps in the ionospheric delays, which impact the estimated VTECs (Xu et al., 2021). In this work, the different levels of accuracy for the radio sources is handled using VCE.

The second group is related to the modelling errors such as using a single ionospheric layer with a fixed height, a simple mapping function, and a geographic or geomagnetic reference frame. The ionosphere stretches during day and shrinks during night, and using a single layer model as an approximation for ionosphere might not be fully representative. Therefore, using two or more layers has the potential to decrease these discrepancies (Rovira-Garcia et al., 2016; Wielgosz et al., 2021). Furthermore, the height of the ionosphere layer also varies depending primarily on the solar activity (Brunini et al., 2011). Thus, using a fixed height for the ionosphere layer may result in errors manifesting themselves in the form of a VTEC bias. In addition, some IAACs such as CODE and ESA use solar-geomagnetic reference frame when estimating the VTECs, which is less accurate than the VTEC derivation with the use of the modip frame (Azpilicueta et al., 2006; Fu et al., 2021; Wielgosz et al., 2021). This also impacts the final IGS

solution used in this thesis for comparison purposes (Chen et al., 2020).

6.4 VGOS-derived Ionospheric Gradients

As expected, both north and south gradients vary across the sessions for all the stations mainly due the change in the ionosphere state. For some stations, there are however jumps in the gradients now and then, mostly resulting from the technical difficulties experienced by these stations. For example, for session 19JUL22VG, the south gradient of KOKEE12M reached 35 TECU/rad, see Fig. 5.14.

As anticipated, the gradients of ONSA13NE and ONSA13SW are almost identical as these twin telescopes are in close vicinity, see Fig. 5.15. The jumps in the south gradient for session 19NOV14VG, 19NOV25VG, 19DEC09VG, and 19DEC26VG are caused very often by the technical problems, such as low fringe amplitude, these two stations experienced, see the corresponding history files present on Fig. C5, C6, C7, and C8. A second contributor to these jumps is the radio source structure as pointed out in some of these files.

WETTZ13S had also its share of difficulties, see the history files present on Fig. C6 and C9. The impact of these difficulties partly manifested itself in the estimated gradients. For instance, for session 20OCT13VG, the north and south gradients jumped to 26.7 and 41.3 TECU/rad, respectively, see Fig. 5.16.

In general, the uncertainty of the south gradients is very often worse than that for the north gradients. The median uncertainty of north gradient is 0.12 ± 0.04 TECU/rad while the median uncertainty of south gradient is 0.36 ± 0.16 TECU/rad. The main reason behind this phenomenon is the geometric configuration and the number of the stations forming the VGOS network. The current VGOS network covers the east-west directions rather well, but the latitudinal coverage is poor as the utilized VGOS stations are located only in the northern hemisphere, see Fig. 2.3. The quality of the south gradient is expected to improve as VGOS stations, such as those in Hartebeesthoek in South Africa, Hobart in Australia, and Ny-Ålesund in Norway, come into service in the near future.

6.5 VGOS Instrumental Offsets

The instrumental offsets of VGOS stations are introduced into the adjustment process in order to absorb the unaccounted effects related to the VGOS receiver chains and the processing stages resulting in broadband delays and dTEC values (Hobiger et al., 2006; Niell et al., 2018). These instrumental offsets are assumed to be constant over the course of the 24-hour session. In the adjustment, the sum of instrumental offsets in the session network were set to zero, see Sec. 4.1.1, (Sekido et al., 2003).

Fig. 5.21, 5.22, and 5.23 show that the instrumental offset for each station varies in size and sign across the investigated sessions. Sometimes, one can notice that the derived instrumental offsets jump in size, which indicate that the corresponding station experienced some technical difficulties (or manipulation in the receiver chain) during the session. For example, on session 17DEC04VG, the instrumental offset of RAEGYEB jumped to -15.18 TECU, see Fig. 5.23. In the first eight hours of the session, RAEGYEB failed to point correctly to the radio source, and thus no pointing module was applied for the rest of the session, which reduced largely the sensitivity of the station, according to the history file of the session on Fig. C1. The impact can be seen in the VTEC time series of the station, where it started at -17 TECU, see Fig. 5.17. A second example can be the jump in the instrumental offset for KOKEE12M to 15.62 TECU on session 19JUL22VG, see Fig. 5.21. This jump is understandable since KOKEE12M experienced RDBEs synchronization and recording problems, see the history file of the session on Fig. C4. Similar to RAEGYEB, the impact of these technical problems can also be seen in the case of VTEC time series derived for KOKEE12M, which started at -12 TECU. A third noticeable example can be the instrumental offset for ONSA13SW on session 19JAN22VG, reaching 30 TECU, see Fig. 5.22. This rise is due to very weak phase cal amplitudes and low fringe amplitudes according to the history files of the sessions, shown on Fig. C2 and C3. When comparing the VTEC time series derived for ONSA13SW with those derived for ONSA13NE, the impact of these technical problems manifested itself as as nonlinear trend between the two time series, clearly visible in the second half of the session.
In general, VGOS stations sometimes experience wide range of technical problems, and the impact of these problems on the estimated VTECs vary in amount. Sometimes, these problems can be resolved and the data can be used. Other times, no remedy can be found and this valuable data is lost.

6.6 Uncertainty of VGOS-derived VTEC

The uncertainty of the VTEC estimates for all the investigated stations, except KOKEE12M, is almost constant across the sessions, see Fig. 5.24, 5.25, and 5.26. The median uncertainty of the stations is between 0.08 ± 0.01 and 0.12 ± 0.03 TECU. This is expected since VGOS delay uncertainty is around 8 ps compared to 31 ps for the geodetic VLBI, thanks to the broadband signal chain system, the stability of VGOS instrumentation, and the enhanced atmospheric sampling (Niell et al., 2018). For KOKEE12M, the uncertainty of the VTEC estimates varies noticeably from session to session, see Fig. 5.24. The smallest and largest uncertainties are 0.1 and 0.41 TECU for session 20FEB03VG and 19JUN11VG, respectively.The median uncertainty of the VTEC estimates is 0.22 ± 0.05 TECU. This is expected since KOKEE12M is the closest VGOS station to the equatorial plasma bubbles, which can cause sharp ionospheric gradient

(Johnston et al., 2017; Wielgosz et al., 2021). This situation introduces as a result, quite large variation of the uncertainty on very short time scales. On the contrary, the stations located in the middle and high latitudes, such as those in Europe, do not experience large variation in the VTEC uncertainty, and thus the derived VTEC estimates better reflect the temporal variation of ionosphere.

7 Conclusions and Outlook

In this master's thesis, a Python code was developed to automatically obtain VGOS sessions, derive VTEC time series from VGOS observations, and analyse these time series also in relation with external ionospheric products. Using this code, VTEC time series for all VGOS stations that are currently operational were derived from all 24-hour VGOS sessions that are publicly available. In comparison with internal ionospheric products, the results show that VGOS-derived VTE time series show similar temporal behavior of ionosphere as in the case of the VTEC time series derived from observations collected with geodetic VLBI stations and GNSS stations co-located with VGOS. In comparison with external ionospheric products, the results also show that VGOS-derived VTE time series show similar temporal behavior of ionosphere as in the case of GIM-based and SMTMs-based VTEC time series.

However, the results reveal that there is a bias between VGOS-derived VTEC time series and the remaining VTEC time series for all stations. This VTEC bias seems to vary in size from session to session. The bias for ONSA13NE appears to be not only almost constant but also of similar size as in the case of ONSA13SW. The smallest RMS differences w.r.t. GIMs were found to be for ONSA13NE and ONSA13SW, i.e., 2.6 ± 0.5 TECU, while the smallest RMS differences w.r.t. SMTMs were found to exist for ISHIOKA, i.e., 1.6 ± 0.2 TECU. The largest RMS differences w.r.t. GIMs were found to exist for KOKEE12M, i.e., 5.4 ± 1.1 TECU, while the largest RMS differences w.r.t. SMTMs occurred for GGAO12M, i.e., 3.3 ± 1.0 TECU. The source of these biases can be attributed to the calibration uncertainty of VGOS and GNSS instrumentation as well as the errors in the ionosphere modelling.

Moreover, for VGOS and VLBI stations, two ionospheric gradients, i.e., in north and south direction, were investigated. The results show that both gradients appear to vary in magnitude, and the uncertainty of the south gradient is often worse than that for the north gradient. This phenomenon possibly stems from the geometric configuration of the VGOS network as the current operational VGOS stations are only well-distributed in the north hemisphere. The quality of south gradient is expected to improve as new stations such as the twin telescopes in NyAlesund in Norway or the VGOS telescope at and Hartebeesthoek in South Africa come into service.

Furthermore, instrumental offsets for VGOS stations were estimated for all sessions. The results indicate that these instrumental offsets vary in size and sign across the investigated sessions. Sometimes, sporadic change in values and signs of the derived instrumental occur in relation to previous and subsequent sessions, which might indicate the existence of technical problems. These problems also manifest themselves in the gradients as shown in the presented results in this subject. Depending on the sources of these problems, the VTEC estimates are affected leading to the degradation of their quality.

Moreover, the results suggest that the uncertainty of VGOS-derived VTECs is in the order of 0.12 ± 0.03 TECU for all VGOS nine stations, except KOKEE12M. For this station, the uncertainty is 0.22 ± 0.05 TECU. This difference in uncertainty can be attributed to the severe ionospheric phenomena in the equatorial region. The uncertainty of all stations is expected to improve as technique-specific effects concerning VGOS are gradually resolved, and more VGOS stations are brought into service.

Recent studies such as from Xu et al. (2017) demonstrate the possibility of inferring the structure index of radio sources directly from geodetic VLBI observations. In the context of this thesis, the structure indices could be used to weight the radio sources or even exclude those that are problematic (extended source structure). This would complement VCE in mitigating the radio source effects and eventually improve VGOS-derived VTEC time series. In addition, there are different ionospheric models, each of which has its advantages and disadvantages. In order to better model the ionosphere with VGOS, one can consider implementing a two-layer voxel model or three-shell model considering the density of VGOS observation and the sparsity of VGOS stations.

In general, VGOS-derived VTEC time series has the potential to for complementing global and/or regional ionosphere maps in the vicinity of VGOS stations. For this purpose, one can use LSQ or Kalman filter to combine the different VTEC time series into one model, but one needs to take into account the VTEC inter-technique biases first. The VGOS-derived VTEC time series from all available sessions is rather short and irregular. Thus, it is not yet clear whether the dependency of the VTEC inter-technique biases on time and solar activity exist. This needs to be further investigated as more sessions are carried out and more VGOS station join the current operating network. In the meantime, one can use geodetic VLBI observations to learn more about the bias dependency.

Bibliography

Abdalati A, Gail W, Busalacchi A Jr (2018) Thriving on our changing planet: A decadal strategy for Earth observation from space, National Academies of Sciences, Engineering, and Medicine. The National Academies Press, Washington, DC, DOI 10.17226/24938, URL https://doi.org/10.17226/24938

Alken P, Thébault E, Beggan CD, Amit H, Aubert J, Baerenzung J, Bondar TN, Brown WJ, Califf S, Chambodut A, Chulliat A, Cox GA, Finlay CC, Fournier A, Gillet N, Grayver A, Hammer MD, Holschneider M, Huder L, Hulot G, Jager T, Kloss C, Korte M, Kuang W, Kuvshinov A, Langlais B, Léger JM, Lesur V, Livermore PW, Lowes FJ, Macmillan S, Magnes W, Mandea M, Marsal S, Matzka J, Metman MC, Minami T, Morschhauser A, Mound JE, Nair M, Nakano S, Olsen N, Pavón-Carrasco FJ, Petrov VG, Ropp G, Rother M, Sabaka TJ, Sanchez S, Saturnino D, Schnepf NR, Shen X, Stolle C, Tangborn A, Tøffner-Clausen L, Toh H, Torta JM, Varner J, Vervelidou F, Vigneron P, Wardinski I, Wicht J, Woods A, Yang Y, Zeren Z, Zhou B (2021) International Geomagnetic Reference Field: the thirteenth generation. Earth, Planets and Space 73(1):49, DOI 10.1186/s40623-020-01288-x, URL https://doi.org/10.1186/s40623-020-01288-x

Altamimi Z, Rebischung P, Métivier L, Collilieux X (2016) ITRF2014: A new release of the International Terrestrial Reference Frame modeling nonlinear station motions. Journal of Geophysical Research: Solid Earth 121(8):6109–6131, DOI https://doi.org/10.1002/2016JB013098, URL https://agupubs.onlinelibrary.wiley.com/doi/abs/10.1002/2016JB013098, https://agupubs.onlinelibrary.wiley.com/doi/pdf/10.1002/2016JB013098

Anderson JM, Xu MH (2018) Source structure and measurement noise are as important as all other residual sources in geodetic VLBI combined. Journal of Geophysical Research: Solid Earth 123(11):10,162–10,190, DOI https://doi.org/10.1029/2018JB015550, URL https://agupubs.onlinelibrary.wiley.com/doi/abs/10.1029/2018JB015550

Azpilicueta F, Brunini C, Radicella S (2006) Global ionospheric maps from GPS observations using modip latitude. Advances in Space Research 38(11):2324–2331, DOI https://doi.org/10.1016/j.asr.2005.07.069, URL https://www.sciencedirect.com/science/article/pii/S0273117705009555, middle and Upper Atmospheres, Active Experiments, and Dusty Plasmas

Bachmann S, Thaller D, Roggenbuck O, Losler M, Messerschmitt L (2016) IVS contribution to

ITRF2014. J Geod 90:631–654, DOI 10.1007/s00190-016-0899-4, URL https://doi.org/10.1007/s00190-016-0899-4

Barrett J, Cappallo R, Corey B, Crew G, Elosegui P, Niell A, Ruszczyk C, Titus M (2019) VGOS data processing manual. 1st edn, MIT Haystack Observatory, URL https://www.haystack.mit.edu/wp-content/uploads/2020/07/docs_hops_000_vgos-data-processing.pdf

Brunini C, Camilion E, Azpilicueta F (2011) Simulation study of the influence of the ionospheric layer height in the thin layer ionospheric model. J Geod 85:637–645, DOI 10.1007/s00190-011-0470-2, URL https://doi.org/10.1007/s00190-011-0470-2

Cai C, Gong Y, Gao Y, Kuang C (2017) An approach to speed up single-frequency PPP convergence with Quad-Constellation GNSS and GIM. Sensors 17(6), DOI 10.3390/s17061302, URL https://www.mdpi.com/1424-8220/17/6/1302

Charlot P, Jacobs CS, Gordon D, Lambert S, de Witt A, Böhm J, Fey AL, Heinkelmann R, Skurikhina E, Titov O, Arias EF, Bolotin S, Bourda G, Ma C, Malkin Z, Nothnagel A, Mayer D, MacMillan DS, Nilsson T, Gaume R (2020) The third realization of the International Celestial Reference Frame by very long baseline interferometry. A&A 644:A159, DOI 10.1051/0004-6361/202038368, URL https://doi.org/10.1051/0004-6361/202038368

Chen P, Liu H, Ma Y, Zheng N (2020) Accuracy and consistency of different global ionospheric maps released by IGS ionosphere associate analysis centers. Advances in Space Research 65(1):163–174, DOI https://doi.org/10.1016/j.asr.2019.09.042

Coster A, MIT/Haystack Observatory (2021) Data from the CEDAR Madrigal database: Madrigal TEC Maps. URL http://cedar.openmadrigal.org/

Davis J, Kellogg L, Arrowsmith J, Buffett B, Constable C, Donnellan A (2016) Challenges and opportunities for research in ESI (CORE). (tech. rep.)., Arlington, Virginia, URL https://smd-prod.s3.amazonaws.com/science-red/s3fs-public/atoms/files/CORE2016%20Updated%3DTAGGED.pdf, report from the NASA Earth Surface and Interior (ESI) Focus Area Workshop November 2–5, 2015.

Dettmering D, Heinkelmann R, Schmidt M (2011a) Systematic differences between VTEC obtained by different space-geodetic techniques during CONT08. J Geod 85:443, DOI 10.1007/s00190-011-0473-z, URL https://doi.org/10.1007/s00190-011-0473-z

Dettmering D, Schmidt M, Heinkelmann R (2011b) Combination of different space-geodetic observations for regional ionosphere modeling. J Geod 85:989–998, DOI 10.1007/s00190-010-0423-1, URL https://doi.org/10.1007/s00190-010-0423-1

Di Giovanni G, Radicella S (1990) An analytical model of the electron density profile in the ionosphere. Advances in Space Research 10(11):27–30, DOI https://doi.org/10.1016/0273-1177(90)90301-F, URL https://www.sciencedirect.com/science/article/pii/027311779090301F

Filip S (2021) magnetic-field-calculator Python library. URL https://pypi.org/project/magnetic-field-calculator/

Fu W, Ma G, Lu W, Maruyama T, Li J, Wan Q, Fan J, Wang X (2021) Improvement of Global Ionospheric TEC Derivation with Multi-Source Data in Modip Latitude. Atmosphere 12(4), DOI 10.3390/atmos12040434, URL https://www.mdpi.com/2073-4433/12/4/434

Ghilani D (2017) 6th edn, John Wiley & Sons, Ltd. DOI https://doi.org/10.1002/9781119390664.ch21, URL https://onlinelibrary.wiley.com/doi/abs/10.1002/9781119390664.ch21

Gipson J (2014) IVS working group IV and the new open format database. In: International VLBI Service for Geodesy and Astrometry 2014 General Meeting Proceedings: "VGOS: The New VLBI Network, pp 248–252

Guillaume S (2017) Geodetic networks and parameter estimation. Lecture Notes, Chair of Mathematical and Physical Geodesy, Institute of Geodesy and Photogrammetry, ETH Zurich

Hernández-Pajares M, Juan J, Sanz J (2009) The IGS VTEC maps: a reliable source of ionospheric information since 1998. J Geod 83:263–275, DOI 10.1007/s00190-008-0266-1, URL https://doi.org/10.1007/s00190-008-0266-1

Hobiger T (2006) VLBI as a tool to probe the ionosphere. A-1040 Wien, Gusshausstraße 27 - 29, URL https://repositum.tuwien.at/handle/20.500.12708/411

Hobiger T, Kondo T, Schuh H (2006) Very long baseline interferometry as a tool to probe the ionosphere. Radio Science 41(1), DOI https://doi.org/10.1029/2005RS003297, URL https://agupubs.onlinelibrary.wiley.com/doi/abs/10.1029/2005RS003297

Hugentobler U, Schaer S, Beutler G, Bock H, Dach R, Jäggi A, Meindl M, Urschl C, Mervart L, Rothacher M, Wild U, Wiget A, Brockmann E, Ineichen D, Weber G, Habrich H, Boucher C (2002) CODE IGS analysis center technical report 2002. Tech. rep.

Jin S, Jin R, Kutoglu H (2017) Positive and negative ionospheric responses to the march 2015 geomagnetic storm from bds observations. J Geod 91:613–626, DOI 10.1007/s00190-016-0988-4, URL https://doi.org/10.1007/s00190-016-0988-4

Johnston G, Riddell A, Hausler G (2017) The International GNSS Service. In: Teunissen PJ, Montenbruck O (eds) Springer Handbook of Global Navigation Satellite Systems, 1st edn, Springer International Publishing, Cham, Switzerland, p 967–982, DOI 10.1007/978-3-319-42928-1.

Julien O, Issler JL, Lestarquit L (2012) Ionospheric delay estimation using Galileo E5 signals only. In: Proceedings of the 25th International Technical Meeting of the Satellite Division of The Institute of Navigation (ION GNSS 2012, Nashville, TN, p 286–301

Klobuchar JA (1987) Ionospheric time-delay algorithm for single-frequency GPS users. IEEE Transactions on Aerospace and Electronic Systems AES-23(3):325–331, DOI 10.1109/TAES.1987.310829

Koch K, Kusche J (2002) Regularization of geopotential determination from satellite data by variance components. *Journal of Geodesy* 76:259–268, DOI 10.1007/s00190-002-0245-x, URL `https://doi.org/10.1007/s00190-002-0245-x`

Mathews PM, Herring TA, Buffett BA (2002) Modeling of nutation and precession: New nutation series for nonrigid Earth and insights into the Earth's interior. Journal of Geophysical Research: Solid Earth 107(B4):ETG 3–1–ETG 3–26, DOI https://doi.org/10.1029/2001JB000390

Niell A, Whitney A, Petrachenko B, Schluter W, Vandenberg N, Hase H (2006) VLBI2010: Current and future requirements for geodetic VLBI systems (WG3—final report). In: 2005 IVS Annual Report NASA/TP-2006-214136. International VLBI Service for Geodesy and Astrometry (IVS)

Niell A, Barrett J, Burns A, Cappallo R, Corey B, Derome M, Eckert C, Elosegui P, McWhirter R, Poirier M, Rajagopalan G, Rogers AEE, Ruszczyk C, SooHoo J, Titus M, Whitney AR, Behrend D, Bolotin S, Gipson JM, Gordon D, Himwich E, Petrachenko B (2018) Demonstration of a Broadband Very Long Baseline Interferometer System: A New Instrument for High-Precision Space Geodesy. Radio Science 53(10):1269–1291, DOI 10.1029/2018RS006617

Noll C (2010) The Crustal Dynamics Data Information System: A resource to support scientific analysis using space geodesy. Advances in Space Research,Volume 45(ue 12):1421–1440, DOI 10.1016/j.asr.2010.01.018, iSSN 0273-1177

Nothnagel A, Artz T, Behrend D, Malkin Z (2017) International VLBI Service for Geodesy and Astrometry - Delivering high-quality products and embarking on observations of the next generation. *Journal of Geodesy* 91(7):711–721, DOI 10.1007/s00190-016-0950-5

Petit G, Luzum B (eds) (2010) IERS Conventions (2010). IERS Technical Note 36, Verlag des Bundesamts fur Kartographie und Geodasie, Frankfurt am Main

Petrachenko B, Niell A, Behrend D, Corey B, Bohm J, Charlot P (2009) Design aspects of the VLBI2010 system. In: Progress report of the VLBI2010 committee (Tech. Rep.): NASA/TM-2009-214180, NASA Technical Memorandum, URL https://ivscc.gsfc.nasa.nasa.gov/publications/misc/TM-2009-214180.pdf

Plag HP, Pearlman M (eds) (2009) Global Geodetic Observing System: Meeting the Requirements of a Global Society on a Changing Planet in 2020, 1st edn. *Springer-Verlag Berlin Heidelberg*, DOI 10.1007/978-3-642-02687-4

Rideout W, Coster A (2006) Automated GPS processing for global total electron content data. GPS Solut 10:219–228, DOI 10.1007/s10291-006-0029-5, URL https://doi.org/10.1007/s10291-006-0029-5

Rovira-Garcia A, Juan J, Sanz J (2016) Accuracy of ionospheric models used in GNSS and SBAS: methodology and analysis. J Geod 90:229–240, DOI 10.1007/s00190-015-0868-3, URL https://doi.org/10.1007/s00190-015-0868-3

Rovira-Garcia A, Ibáñez-Segura D, Orús-Perez R (2020) Assessing the quality of ionospheric models through GNSS positioning error: methodology and results. GPS Solut 24, 4, DOI 10.1007/s10291-019-0918-z, URL https://doi.org/10.1007/s10291-019-0918-z

Schaer S (1999) Mapping and predicting the Earth's ionosphere using the Global Positioning System. Phd thesis, University of Berne

Schaer S, Gurtner W, Feltens J (1998) IONEX: The IONosphere Map Exchange format Version 1. In: By Dow J, Kouba J, Springer T (eds) Proc. of the IGS Analysis Center Workshop, Darmstadt, Germany, pp 233–247,

Sekido M, Kondo T, Kawai E, Imae M (2003) Evaluation of GPS-based ionospheric TEC map by comparing with VLBI data. *Radio Science* 38(4), DOI 10.1029/2000RS002620

Teke K, Boehm J, Krasna H, Pany A, Plank L, Schuh H (2009) Piecewise Linear Offsets for VLBI Parameter Estimation. In: 19th EVGA Working Meeting & 10th IVS Analysis Workshop, IVS 10th Anniversary Celebration, International VLBI Service for Geodesy and Astrometry, Bordeaux, France

Vierinen J, Coster AJ, Rideout WC, Erickson PJ, Norberg J (2016) Statistical framework for estimating GNSS bias. Atmospheric Measurement Techniques 9(3):1303–1312, DOI 10.5194/amt-9-1303-2016, URL https://amt.copernicus.org/articles/9/1303/2016/

Whitaker J (2021) Pyproj Python Library. URL https://pypi.org/project/pyproj/

Wielgosz P, Milanowska B, Krypiak-Gregorczyk A (2021) Validation of GNSS-derived global ionosphere maps for different solar activity levels: case studies for years 2014 and 2018. GPS Solut 25:103, DOI 10.1007/s10291-021-01142-x

Xu M, Heinkelmann R, Anderson J (2017) The impacts of source structure on geodetic parameters demonstrated by the radio source 3c371. J Geod 91:767–781, DOI 10.1007/s00190-016-0990-x, URL https://doi.org/10.1007/s00190-016-0990-x

Xu MH, Savolainen T, Zubko N, Poutanen M, Lunz S, Schuh H, Wang GL (2021) Imaging VGOS observations and investigating source structure effects. Journal of Geophysical Research: Solid Earth 126(4):e2020JB021,238, DOI https://doi.org/10.1029/2020JB021238, e2020JB021238 2020JB021238

List of Figures

List of Tables

Appendix

A PyIono

The python code developed for the purposes of this master's thesis is available under: `https://gitlab.ethz.ch/space-geodesy-open/pyiono` as v.0.0.3.

B GNSS Observation Files

```
#------------------------------------------------------------
#STA  SAT         epoch (UTC)          az(deg)  el(deg)   STEC
#------------------------------------------------------------
WTZZ  G_22  2019/04/30 00:00:12.000    94.324  44.236    5.494
WTZZ  G_06  2019/04/30 00:00:12.000   -49.339  28.268    8.320
WTZZ  G_03  2019/04/30 00:00:12.000    79.097  64.832    8.427
WTZZ  G_01  2019/04/30 00:00:12.000   153.284  32.382   13.079
WTZZ  G_17  2019/04/30 00:00:12.000  -105.661  30.715    6.619
NYA1  G_23  2019/04/30 00:00:12.000  -173.152  35.796    7.671
NYA1  G_06  2019/04/30 00:00:12.000   -80.368  44.366    5.495
NYA1  G_17  2019/04/30 00:00:12.000  -126.723  16.114    7.668
NYA1  G_14  2019/04/30 00:00:12.000    58.668  20.719   11.080
NYA1  G_03  2019/04/30 00:00:12.000   140.704  49.045    6.770
NYA1  G_02  2019/04/30 00:00:12.000   -48.285  18.594    9.819
NYA1  G_19  2019/04/30 00:00:12.000  -111.312  29.481    7.083
```

```
-----------------------------------------------
STA         X             Y             Z
-----------------------------------------------
BADG   -838281.513   3865777.334   4987624.632
GODE  1130773.7180 -4831253.5810  3994200.4220
HOB2  -3950071.274   2522415.218  -4311638.512
HRAO  5085352.5970  2668395.9920 -2768731.5510
KAT1  -4147413.524   4581462.781  -1573359.673
KOKB -5543838.3609 -2054586.6103  2387810.1225
KOKV -5543838.3609 -2054586.6103  2387810.1225
NYA1   1202434.000    252632.000   6237772.000
ONSA   3370658.832    711876.939   5349786.745
WES2   1492233.247  -4458089.489   4296046.035
WTZS   4075535.300    931822.185   4801608.915
WTZZ   4075579.269    931853.281   4801569.136
```

Figure B1: GNSS observation file (top) and the file of station coordinates (bottom) as an input to the GNSS module

C History Files

```
+CORRELATOR_NOTES

+STATION_NOTES

WESTFORD (Wf/E): OK.

GGAO12M (Gs/G):  OK.

KOKEE12M (K2/H): Station reports high winds caused multiple off-sources
                   starting at 339-0200 through 339-2000.

ISHIOKA (Is/I):  OK.

RAEGYEB  (Yj/Y):  Antenna not pointing until 339-0657.  No pointing model
                    applied from that time through  the remainder of CONT,
                    greatly reducing station sensitivity.
                  Nominal channel to channel phase scatter and fringe
                   amplitude variation.

WETTZ13S (Ws/V): Intermittent low fringe amplitude in band D.
                 Nominal channel to channel fringe amplitude variation.
```

Figure C1: Correlator and station notes from the history file of session 17DEC04VG

```
+CORRELATOR_NOTES

For the ONSA13NE-ONSA13SW baseline only 10 RFI-free channels included and
  notch filters applied to prevent phase cal tone cross-correlation. Due
  to the proximity of the stations and the lack of RFI-free channels, dTEC
  estimation was disabled for this baseline and fixed to zero.

+STATION_NOTES

WESTFORD (Wf/E): OK.

GGAO12M (Gs/G):  OK.

KOKEE12M (K2/H): Occasional G codes due to low fringe amplitude in band D.

RAEGYEB  (Yj/Y): Started late at 007-1844 due to communication failures
                   with the antenna control unit.
                 Presumed pointing problem caused G codes on upwards of 30%
                   of scans per baseline due to weak fringes in band D.

ONSA13NE (Oe/S): Missed from 008-0138 to 008-0608 due to recorder problems.
                 CDMS crashed at 008-0753 but was recovered.

ONSA13SW (Ow/T): Missed 133 scans interspersed throughout the schedule for
                   unknown reasons.
                 fourfit H code threshold lowered due to very weak phase cal
                   amplitudes.

WETTZ13S (Ws/V): OK.
```

Figure C2: Correlator and station notes from the history file of session 19JAN07VG

```
+CORRELATOR_NOTES

For the ONSA13NE-ONSA13SW baseline only 10 RFI-free channels included and
  notch filters applied to prevent phase cal tone cross-correlation. Due
  to the proximity of the stations and the lack of RFI-free channels, dTEC
  estimation was disabled for this baseline and fixed to zero.

+STATION_NOTES

WESTFORD (Wf/E): OK.

GGAO12M (Gs/G):  Did not correlate due to an RDBE configuration problem.

KOKEE12M (K2/H): Very occasional G codes due to low fringe amplitudes in
                   bands B and C, or D (exclusively).

RAEGYEB  (Yj/Y): Presumed pointing problem caused G codes on upwards of 14%
                   of scans per baseline due to low fringe amplitudes in
                    band D.

ONSA13NE (Oe/S): OK.

ONSA13SW (Ow/T): Intermittently low fringe amplitudes in upper channels of
                   band D after 023-0400 cause some G codes.
                 fourfit H code threshold lowered due to very weak phase cal
                   amplitudes.

WETTZ13S (Ws/V): Very occasional G codes due to low fringe amplitudes in
                   band A.
```

Figure C3: Correlator and station notes from the history file of session 19JAN22VG

```
+CORRELATOR_NOTES

There are 185 G codes in the experiment due to collectively low fringe
  amplitudes in one or more individual bands.  These are caused by
  source structure effects.  Four additional G codes are due to baselines
  passing through zero fringe rate.

+STATION_NOTES

WESTFORD (Wf/E): Recorded using R2DBE digital back ends.

GGAO12M (Gs/G):  OK.

KOKEE12M (K2/H): Started late at 203-1852 due to RDBEs not synced and Mark 6
                   not recording.
                 Ended at 204-0050 due to no commercial electric power.

RAEGYEB  (Yj/Y): Observed, but data not included in database due to unstable
                    phase cal. behavior.

ONSA13NE (Oe/S): OK.

ONSA13SW (Ow/T): OK.

WETTZ13S (Ws/V): Missed from 203-1815 to 203-2005 due to FILA10Gs and Mark
                   6 not recording.
```

Figure C4: Correlator and station notes from the history file of session 19JUL22VG

```
+CORRELATOR_NOTES

There are 79 G codes in the experiment. 66 are due to collectively low
  fringe amplitudes in one or more individual bands caused by source
  structure effects.  One is caused by a baseline passing through zero
  fringe rate.  The remainder of the fourfit letter codes are documented
  in the station notes.

+STATION_NOTES

WESTFORD (Wf/E): OK.

GGAO12M (Gs/G):  OK.

KOKEE12M (K2/H): OK.

MACGO12M (Mg/M): Station did not participate due to warranty repair work.

RAEGYEB  (Yj/Y): Data not included in database due to pointing errors and
                   unstable phase cal.

ONSA13NE (Oe/S): Missed from 318-2308 to 319-0740 due to a recorder problem.
                 Packet loss problems from 319-0948 to 319-1052 cause
                   numerous short scans.
                 One H code caused by no fringes or phase cal in channel
                   X14LX/Y of scan 319-0954.
                 Four G codes caused by no fringes or phase cal in channel
                   X14LX/Y of scans 319-1148 through 319-1154.

ONSA13SW (Ow/T): Missed from 318-2308 to 319-0740, and from 319-0948 to
                   319-1052 due to a recorder problem.
                 One H code caused by no fringes or phase cal in channel
                   X14LX/Y of scan 319-1149b and scan 319-1153.
                 Eight G codes caused by no fringes or phase cal in channel
                   X14LX/Y of scans 319-1148 through 319-1154.

WETTZ13S (Ws/V): Did not correlate due to unlocked LO Synthesizer.
```

Figure C5: Correlator and station notes from the history file of session 19NOV14VG

```
+CORRELATOR_NOTES

There are 83 G codes in the experiment not associated with Ow or Yj
  baselines.  These are almost all exclusively due to the collectively
  low fringe amplitudes in one or more individual bands caused by source
  structure effects.  Eight are due to baselines passing through zero
  fringe rate.  The Ow and Yj G codes are discussed in the station notes.

+STATION_NOTES

WESTFORD (Wf/E): OK.

GGAO12M (Gs/G):  OK.

KOKEE12M (K2/H): Missed six scans at 330-0826b through 330-0837a due to
                   field system computer reboot.

MACGO12M (Mg/M): Missed from 329-2258 to 330-1352 due to antenna high wind
                   stow.
                 Data not included in database.

RAEGYEB  (Yj/Y): Recorded with 10 MHz pcal tone intervals.
                 Low fringe amplitude and unstable phase in channel
                   X01LX/Y cause numerous G codes -- channel deleted in
                   fringing.
                 Station polarization swapped during correlation.
                 There are 46 G codes associated with Yj baselines.  Not
                   all of them are caused by Yj, some are due to the above
                   given reasons of source structure, but also a large
                   number are due to low fringe amplitudes in band A.

ONSA13NE (Oe/S): OK.

ONSA13SW (Ow/T): There are 66 codes associated with Ow baselines.  Not
                   all of them are caused by Ow, but most are, some due to
                   the usual reasons of source structure,  but also a large
                   number due to pronounced amplitude rolloff as frequency
                   decreases in band A.
```

Figure C6: Correlator and station notes from the history file of session 19NOV25VG

```
+CORRELATOR_NOTES

There are 258 G codes in the experiment.  Some are due to collectively low
  fringe amplitudes in one or more individual bands caused by source
  structure effects.  Some are caused by baselines passing through zero
  fringe rate.  Some are caused by station-specific problems, the root of
  which will be described in the station notes section.  Since these
  effects are sometimes compounded, specific counts attributed to cause
  will not be given for this experiment, only general descriptions.

+STATION_NOTES

WESTFORD (Wf/E): OK.
GGAO12M (Gs/G):  OK.

KOKEE12M (K2/H): Did not participate due to motor controller and network
                   upgrades.

MACGO12M (Mg/M): OK.
                 Data not included in data base.

ISHIOKA (Is/I):  Some G codes caused by collectively low fringe amplitude
                   in band A due to a recorder problem inserting fill
                   pattern into the data.

RAEGYEB  (Yj/Y): Recorded with 10 MHz pcal tone intervals.
                 Data not production correlated due to clean up oscillator
                   offsetting the pcal tone frequency, rendering it
                   unusable.

ONSA13NE (Oe/S): Some G codes caused by pronounced fringe amplitude
                   rolloff in the lower frequencies of band A.
                 Scans 344-0730 and 344-0810 had only a few seconds of
                   integration time.

ONSA13SW (Ow/T): OK.

WETTZ13S (Ws/V): Started late at 343-1831 due to module and datastream
                   problems on the Mark 6.
```

Figure C7: Correlator and station notes from the history file of session 19DEC09VG

```
+CORRELATOR_NOTES

There are 498 G codes in the experiment.  Some are due to collectively low
  fringe amplitudes in one or more individual bands caused by source
  structure effects.  Some are caused by baselines passing through zero
  fringe rate.  Some are caused by station-specific problems, the root of
  which will be described in the station notes section.  Since these
  effects are sometimes compounded, specific counts attributed to cause
  will not be given for this experiment, only general descriptions.

+STATION_NOTES

WESTFORD (Wf/E): OK.

GGAO12M (Gs/G):  Station did not participate.  Reason unknown.

KOKEE12M (K2/H): Missed from 361-0128 to 361-0433 due to a power outage.
                 Missed from 361-0704 to 361-0737 due to a power outage.

MACGO12M (Mg/M): Band B X pol fringe and pcal amplitudes greatly reduced
                   due to RDBE problem.
                 Data not included in database.

ISHIOKA (Is/I):  Upwards of 20% G codes in all baselines due to no
                   fringes in band A.

RAEGYEB  (Yj/Y): Recorded with 10 MHz pcal tone intervals.
                 Data not included in database due to problems setting
                   sampler delays.

ONSA13NE (Oe/S): OK.

ONSA13SW (Ow/T): A few G codes caused by pronounced fringe amplitude
                   rolloff in the lower frequencies of band A.

WETTZ13S (Ws/V): Started late at 343-1831 due to module and datastream
                   problems on the Mark 6.
```

Figure C8: Correlator and station notes from the history file of session 19DEC26VG

```
+CORRELATOR_NOTES

Test correlation done in DiFX 2.6.1 for comparison with
results of DiFX 2.5.3.
Please download the vgosDB at your earliest convenience:
ftp://ftp.mpifr-bonn.mpg.de/geoarchive/database/20OCT13VG_d261.tgz.
This database includes Yj and baseline Oe-Ow (applied notch filters
to flag pcal tones and RFI).

+STATION_NOTES

 WESTFORD (Wf/E): No pcal available; excluded from correlation.
 GGAO12M  (Gs/G): Station did not participate.
 KOKEE12M (K2/H): Nothing to report.

 RAEGYEB  (Yj/v): Low fringe amplitude in last 8 channels (band D)
                  causing numerous G codes.
                  Applied tone mask in control file because pcal
                  tones were injected every 10 MHz.

 WETTZ13S (Ws/t): Numerous non-detections particularly on long
                  baselines for unknown reason.
                  Since the correlation crashed a few times due to
                  problems with the Mark6 module, there might have
                  been recording problems at the station.
                  Recorrelation with d261 could save a handful of scans.

 ONSA13NE (Oe/A): Applied notch filters to flag pcal tones and RFI on
                  short baseline Oe-Ow to avoid most G codes.
                  RFI particularly affects band A channels X1LX/Y, X1LX/Y,
                  X1LX/Y, X1LX/Y and channel X27LX/Y; channels removed
                  from fringe fitting on baseline Oe-Ow.

 ONSA13SW (Ow/y): Applied notch filters to flag pcal tones and RFI on
                  short baseline Oe-Ow to avoid most G codes.
                  RFI particularly affects band A, channels X1LX/Y, X1LX/Y,
                  X1LX/Y, X1LX/Y and channel X27LX/Y; channels removed
                  from fringe fitting on baseline Oe-Ow.
```

Figure C9: Correlator and station notes from the history file of session 20OCT13VG

```
+CORRELATOR_NOTES

Correlated using DiFX-2.6.1; running difx2mark4 under DiFX-2.6.2.

Please download the vgosDB at your earliest convenience:
ftp://ftp.mpifr-bonn.mpg.de/geoarchive/database/21FEB01VG.tgz.
Applied notch filters on baseline Oe-Ow to avoid correlation of pcal
tones and remove RFI which, however, worked only partially.

+STATION_NOTES

 GGAO12M  (Gs/G): Station didn't observe due to a winter storm and
                  dangerous conditions at the site.

 ISHIOKA  (Is/Q): The V signal contains feed LNA noise in 2-10GHz band.

 KOKEE12M (K2/H): OK.

 MACGO12M (Mg/M): Observed with warm receiver.
                  Occasionally low pcal amplitude.

 ONSA13NE (Oe/A): Numerous G codes on Oe-Ow baseline.

 ONSA13SW (Ow/y): Numerous G codes on Oe-Ow baseline.

 WESTFORD (Wf/E): Ok.

 WETTZ13S (Ws/t): Stopped observing between 032/18:30 and 19:30 UT
                  for V21032.

 RAEGYEB  (Yj/v): Station had Mark6 recording problems because
                  one of the disks didn't get properly erased before
                  the session. All the scans between 032-1933a and
                  033-0224 are missing, no valid data/pcal until
                  033-0837.
                  Particularly high pcal amplitude in bands A and B.
                  Low fringe amplitude in the first band. Phase jumps
                  mostly in the first two bands interchanging between
                  channels.
```

Figure C10: Correlator and station notes from the history file of session 21FEB01VG

Eidgenössische Technische Hochschule Zürich
Swiss Federal Institute of Technology Zurich

Declaration of originality

The signed declaration of originality is a component of every semester paper, Bachelor's thesis, Master's thesis and any other degree paper undertaken during the course of studies, including the respective electronic versions.

Lecturers may also require a declaration of originality for other written papers compiled for their courses.

I hereby confirm that I am the sole author of the written work here enclosed and that I have compiled it in my own words. Parts excepted are corrections of form and content by the supervisor.

Title of work (in block letters):

Quality Assessment of VTEC Products Derived from Observations with the Next-Generation VLBI System

Authored by (in block letters):

For papers written by groups the names of all authors are required.

Name(s):	**First name(s):**
Awadaljeed	Mudathir

With my signature I confirm that

- I have committed none of the forms of plagiarism described in the 'Citation etiquette' information sheet.
- I have documented all methods, data and processes truthfully.
- I have not manipulated any data.
- I have mentioned all persons who were significant facilitators of the work.

I am aware that the work may be screened electronically for plagiarism.

Place, date	**Signature(s)**
Zurich, 12.07.2021	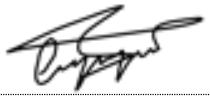

For papers written by groups the names of all authors are required. Their signatures collectively guarantee the entire content of the written paper.